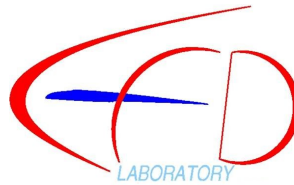


Wind Turbine Wake Encounter Study

Version 1.0



University of Liverpool

Authors: Dr Yaxing Wang
Dr Mark White
Prof George Barakos

Address: School of Engineering
University of Liverpool
Harrison Hughes Building
Liverpool
L69 3GH
United Kingdom

Date: March 27, 2015

Abstract

The wake vortices generated by a wind turbine or a wind farm could cause interference with passing light aircraft. A wind turbine wake study using engineering wake modelling, CFD, LIDAR field measurements and piloted flight simulations was carried out at University of Liverpool in collaboration with CAA, UK. A modified Kocurek wind turbine wake model has been developed to simulate wind turbine wakes. It has been validated using the MEXICO wind turbine and the PIV wind tunnel measurements, as well as CFD wake simulation results. This wake vortex model was applied to a WTN250 wind turbine that is installed near the East Midlands Airport, UK, where field measurements of wind turbine wake using LIDAR were carried out. The LIDAR data was compared with the wake velocity fields generated by different wake modelling methods. The WTN250 wind turbine wake velocities generated by the Kocurek wake vortex model were integrated into an aircraft flight dynamic model to simulate a wind turbine wake encounter scenario, designed for a light aircraft approaching an airport, where a wind turbine was installed. The severity of the wind turbine wake encounter was investigated using piloted flight simulations. The simulation results suggest that the wake generated minor upsets on the aircraft and resulted a severity rating of B if only the disturbances caused by wake velocity deficits were taken into account. Off-line simulations and analysis of wind turbine wake encounters were also carried out and the results indicated that for the small size WTN250 wind turbine, the approach based on the Beddoes circulation formula appeared to give predictions in line with the LIDAR measurements. The off-line analysis also showed the variability of the predictions based on the employed wake models.

Contents

1	Introduction and Motivation	1
2	Wind Turbine Wake Modelling	3
2.1	Kocurek wind turbine wake vortex model	3
2.2	Validation of Kocurek wind turbine wake model	6
2.3	Wind turbine wake velocity deficit models	9
2.4	Wind turbine wake study by full CFD	9
3	LIDAR Wind Turbine Wake Measurement Campaign	12
3.1	WTN250 wind turbines and historical wind data at East Midlands airport	12
3.2	Galion LIDAR and Set-up	16
3.3	LIDAR data processing	17
3.4	Results and discussion of the LIDAR campaign	19
3.4.1	Results of the LIDAR campaign	19
3.4.2	Comparisons of the LIDAR measurements	23
4	Flight Simulation of Aircraft Encounter with Wind Turbine Wakes	27
4.1	Wind turbine configurations and wind turbine wake encounter scenario	27
4.2	Description of the flight simulator	30
4.3	Pilot wake vortex severity rating scale	31
4.4	Wind turbine trial matrices	31
4.5	Simulation results	31
4.6	Discussion of simulation results	38
5	Off-line Flight Simulation of Wind Turbine Wake Encounter	39
5.1	Analysis of wind farm wake impacts on general aviation airport in the Kansas report	39
5.2	Off-line analysis of WTN250 wind turbine wake encounter	39
5.2.1	Wake induced crosswinds of a WTN250 wind turbine	41
5.2.2	Variations of forces and moments of the GA during wake encounters	46
5.2.3	Analysis of the roll upsets during wake encounters	55
5.3	Discussion of off-line simulation results	59
6	Conclusions and Future Work	60
7	Appendix: WTN250 Wake LIDAR Measurements	64
8	Appendix: Piloted Flight Simulation Results	79

List of Figures

2.1	The coordinate system of the Kocurek wind turbine wake model.	4
2.2	Rotor work state velocity relationships in axial flow [8].	5
2.3	MEXICO wind turbine model and wake vortices of full CFD simulation at wind speed 15m/s [4].	7
2.4	MEXICO wind turbine wake generated by Kocurek wind turbine wake model, wind speed 15 m/s.	8
2.5	MEXICO wind turbine flow field velocity comparisons between CFD and the Kocurek wake model at a wind speed 15 m/s.	9
2.6	MEXICO wind turbine flow field velocity comparisons between CFD and the Kocurek wake model at a wind speed 10 m/s.	10
2.7	MEXICO wind turbine flow field velocity comparisons between CFD and the Kocurek wake model at a wind speed 24 m/s.	10
2.8	MEXICO wind turbine wake generated by the full CFD, wind speed 15 m/s [5].	11
3.1	WTN250 wind turbines at East Midlands airport.	13
3.2	East Midlands aerodrome.	13
3.3	The final LIDAR site.	14
3.4	Diagram of the WTN250 wind turbine.	15
3.5	Wind direction over the entire year.	16
3.6	Fraction of time with the wind blowing from the various directions on a daily basis.	16
3.7	Average daily minimum(red), maximum (green) and average (black) wind speed with percentile bands.	16
3.8	Galion LIDAR of Sgurr Energy.	17
3.9	The on-site Galion LIDAR.	18
3.10	Schematic of the PPI or Arc scan for wind turbine wake measurements.	19
3.11	Locations of Galion LIDAR and the wind turbines.	20
3.12	The refined scan plane used in the LIDAR measurement.	21
3.13	Ten-minutes averaged line of sight velocity measured on 07-04-2014.	23
3.14	Ten-minutes averaged line of sight velocity measured on 07-04-2014.	23
3.15	Ten-minutes averaged line of sight velocity measured on 07-04-2014.	24
3.16	One-hour averaged Line of sight velocity measured on 07-04-2014.	25
3.17	Wake velocity deficits using the Park wake model for an approximate WTN250 wind turbine at a wind speed of 10 m/s.	25
3.18	Predicted line of sight velocity contours in the LIDAR scan plane.	26
4.1	NREL wind turbine wake crossing encounter.	28
4.2	NREL wind turbine wake oblique encounter at 45 deg.	29
4.3	External view of the simulator.	30
4.4	Internal view of the HELIFLIGHT simulator.	30
4.5	Wake Vortex Severity Rating Scale [12].	34
4.6	Comparison of the dimension of the induced velocity grid points and the size of a GA geometry.	35
4.7	Time history of the dynamics of GA aircraft and pilot's controls during wake encounter, wind turbine hub height 100 ft, wind speed 10 m/s, angle 90.0, offset 1.5D.	36

4.8	Dynamics of GA aircraft and pilot's controls during wake encounter, wind turbine hub height 100 ft, wind speed 10 m/s, angle 90.0, offset 1.5D, pilot's control holding. . . .	37
4.9	Comparison of the relative wake velocity deficits.	38
5.1	Circulation decay curves for the WTN250 wind turbine, wind speed 32.8 ft/s.	40
5.2	Contours of the induced velocities (ft/s) in a region from -0.5D to 15D. Beddoes circulation formula, normal core size (5%), exponential decay, wind speed 32.8 ft/s	41
5.3	Contours of the induced velocities (ft/s) in a region from -0.5D to 15D. Kansas circulation formula, enlarged core size, exponential decay, wind speed 32.8 ft/s	42
5.4	Wake induced crosswind speeds with distances, wind speed 32.8 ft/s, Model 1: Beddoes circulation formula with normal core size; Model 2: Kansas circulation formula with enlarged core size.	43
5.5	Contours of the induced velocities (ft/s) in a region from -0.5D to 15D. Beddoes circulation formula, normal core size, exponential decay, wind speed 20 m/s.	44
5.6	Contours of the induced velocities (ft/s) in a region from -0.5D to 15D. Kansas circulation formula, enlarged core size, exponential decay, wind speed 20 m/s.	44
5.7	Wake induced crosswind speeds with distances, wind speed 65.6 ft/s, Model 1: Beddoes circulation formula with normal core size; Model 2: Kansas circulation formula with enlarged core size..	45
5.8	Variations of coefficients of forces and moments in off-line crossing wake encounter, GA flew along the runway Central line, offset 3D, Beddoes circulation formula, normal core size, wind speed 32.8 ft/s.	46
5.9	Variations of coefficients of forces and moments in off-line crossing wake encounter, GA flew along the runway central line, offset 3D, Kansas circulation formula, enlarged core size, wind speed 32.8 ft/s.	47
5.10	Variations of coefficients of forces and moments in off-line crossing wake encounter, GA flew along the runway Central line, offset 5D, Beddoes circulation formula, normal core size, wind speed 32.8 ft/s.	48
5.11	Variations of coefficients of forces and moments in off-line crossing wake encounter, GA flew along the runway central line, offset 5D, Kansas circulation formula, enlarged core size, wind speed 32.8 ft/s.	48
5.12	Variations of coefficients of forces and moments in off-line crossing wake encounter, GA flew along the runway Central line, offset 10D, Beddoes circulation formula, normal core size, wind speed 32.8 ft/s.	49
5.13	Variations of coefficients of forces and moments in off-line crossing wake encounter, GA flew along the runway central line, offset 10D, Kansas circulation formula, enlarged core size, wind speed 32.8 ft/s.	49
5.14	Variations of coefficients of forces and moments in off-line crossing wake encounter, GA flew along the runway Central line, offset 3D, 45 deg oblique encounter, Beddoes circulation formula, normal core size, wind speed 32.8 ft/s.	50
5.15	Variations of coefficients of forces and moments in off-line crossing wake encounter, GA flew along the runway Central line, offset 3D, 45 deg oblique encounter, Kansas circulation formula, enlarged core size, wind speed 32.8 ft/s.	50
5.16	Variations of coefficients of forces and moments in off-line crossing wake encounter, GA flew along the runway Central line, offset 5D, 45 deg oblique encounter, Beddoes circulation formula, normal core size, wind speed 32.8 ft/s.	51
5.17	Variations of coefficients of forces and moments in off-line crossing wake encounter, GA flew along the runway Central line, offset 5D, 45 deg oblique encounter, Kansas circulation formula, enlarged core size, wind speed 32.8 ft/s.	51
5.18	Variations of coefficients of forces and moments in off-line crossing wake encounter, GA flew along the runway Central line, offset 10D, 45 deg oblique encounter, Beddoes circulation formula, normal core size, wind speed 32.8 ft/s.	52

5.19	Variations of coefficients of forces and moments in off-line crossing wake encounter, GA flew along the runway Central line, offset 10D, 45 deg oblique encounter, Kansas circulation formula, enlarged core size, wind speed 32.8 ft/s.	52
5.20	Wake induced crosswind speeds against distances, 90 m diameter large wind turbine, wind speed 32.8 ft/s and 65.6 ft/s.	53
5.21	Variations of coefficients of forces and moments in off-line crossing wake encounter, GA flew along the runway Central line, offset 3D, Beddoes circulation formula, normal core size, wind speed 32.8 ft/s, large wind turbine.	53
5.22	Variations of coefficients of forces and moments in off-line crossing wake encounter, GA flew along the runway central line, offset 3D, Kansas circulation formula, enlarged core size, wind speed 32.8 ft/s, large wind turbine.	54
5.23	Wake induced velocities in the regions close to the rotor blade tip, WTN250 wind turbine, wind speed 32.8 ft/s.	55
5.24	Wake induced rolling moment coefficients by V_y , WTN250 wind turbine, wind speed 32.8 ft/s.	56
5.25	Wake induced rolling moment coefficients by V_y , WTN250 wind turbine, wind speed 65.6 ft/s.	56
5.26	Wake induced rolling moment coefficients by V_x , WTN250 wind turbine, wind speed 32.8 ft/s.	57
5.27	Wake induced rolling moment coefficients by V_x , WTN250 wind turbine, wind speed 65.6 ft/s.	57
5.28	Wake induced rolling moment coefficients calculated from different numbers of spanwise computing points, WTN250 wind turbine, wind speed 65.6 ft/s.	58
5.29	Wake induced rolling moment coefficients, large wind turbine with a 90m diameter, wind speed 65.6 ft/s.	58
7.1	Ten-minutes averaged line of sight velocity measured on 07-04-2014.	65
7.2	Ten-minutes averaged line of sight velocity measured on 07-04-2014.	65
7.3	Ten-minutes averaged line of sight velocity measured on 07-04-2014.	66
7.4	One-hour (13-14) averaged Line of sight velocity measured on 07-04-2014.	66
7.5	Ten-minutes averaged line of sight velocity measured on 06-04-2014.	67
7.6	Ten-minutes averaged line of sight velocity measured on 06-04-2014.	67
7.7	Ten-minutes averaged line of sight velocity measured on 06-04-2014.	68
7.8	One-hour (05-06) averaged Line of sight velocity measured on 06-04-2014.	68
7.9	Ten-minutes averaged line of sight velocity measured on 06-04-2014.	69
7.10	Ten-minutes averaged line of sight velocity measured on 06-04-2014.	69
7.11	Ten-minutes averaged line of sight velocity measured on 06-04-2014.	70
7.12	One-hour (15-16) averaged Line of sight velocity measured on 06-04-2014.	70
7.13	Ten-minutes averaged line of sight velocity measured on 05-04-2014.	71
7.14	Ten-minutes averaged line of sight velocity measured on 05-04-2014.	71
7.15	Ten-minutes averaged line of sight velocity measured on 05-04-2014.	72
7.16	One-hour (16-17) averaged Line of sight velocity measured on 05-04-2014.	72
7.17	Ten-minutes averaged line of sight velocity measured on 24-03-2014.	73
7.18	Ten-minutes averaged line of sight velocity measured on 24-03-2014.	73
7.19	Ten-minutes averaged line of sight velocity measured on 24-03-2014.	74
7.20	One-hour (16-17) averaged Line of sight velocity measured on 24-03-2014.	74
7.21	Ten-minutes averaged line of sight velocity measured on 21-03-2014.	75
7.22	Ten-minutes averaged line of sight velocity measured on 21-03-2014.	75
7.23	Ten-minutes averaged line of sight velocity measured on 21-03-2014.	76
7.24	One-hour (21-22) averaged Line of sight velocity measured on 21-03-2014.	76
7.25	Ten-minutes averaged line of sight velocity measured on 20-03-2014.	77
7.26	Ten-minutes averaged line of sight velocity measured on 20-03-2014.	77
7.27	Ten-minutes averaged line of sight velocity measured on 20-03-2014.	78
7.28	One-hour (04-05) averaged Line of sight velocity measured on 20-03-2014.	78

8.28 Time history of the dynamics of GA aircraft and pilot's controls during wake encounter,
wind turbine hub height 150 ft, wind speed 10 m/s, angle 45.0, offset 1.0D. 107

List of Tables

3.1	WTN250 wind turbine technical data	14
3.2	Valid LIDAR datasets	22
4.1	NREL wind turbine wake encounter simulation matrix.	27
4.2	WTN250 wind turbine data used for the wake encounter simulation matrix.	28
4.3	Test matrix of simulation 2, test pilot 1; time: 25-06-2013	31
4.4	Test matrix of simulation 2, test pilot 2; time: 28-06-2013	32
4.5	Test matrix of simulation 3, test pilot: Student pilot 1; time: 29-09-2013	32
4.6	Test matrix of simulation 4, test pilot: Student pilot 2; time: 15-10-2013	33
5.1	Parameters used in the off-line analysis	41

Nomenclature

\bar{v}	Non-dimensional induced velocity by v_h
\bar{v}_a	Non-dimensional axial impressed velocity by v_h
δ	Effective turbulent viscosity coefficient
Γ	Circulation
λ	Contraction rate parameter
ν	Kinematic viscosity coefficient
Ω	Rotation speed of the rotor
σ	Solidity of rotor blades
A	Developed wake radius
c	Chord of blade
c_T	Thrust coefficient
k_z	Axial settling rate
r_0	Initial core radius
v_a	Axial impressed velocity
v_h	Mean induced velocity in hover
V_{line}	line of sight velocity
Az	Azimuthal angle
D	Diameter of wind turbine rotor
El	Elevation angle
R	Wind turbine rotor radius
vec	Measurement point vector

Chapter 1

Introduction and Motivation

The wakes generated by a wind turbine or a wind farm have similar, but not identical, characteristics as aircraft wakes. They may also pose a potential hazard to nearby aircraft in terms of a wake encounter. Wind turbine wakes have their own structure, duration and decay [17, 14]. With the increasing size of modern wind turbine rotors, the strength and influencing region of the wind turbine wakes has increased, which might potentially generate hazards to nearby flying aircraft. In the UK, wind turbines are being proposed and built close to aerodromes, producing an urgent need to assess the potential impact of wake turbulence on aircraft and in particular, to light aircraft and helicopters [3]. Therefore, understanding and prediction of wind turbine wake characteristics are vital to prevent upsets and potential accidents during wind turbine wake encounters.

Wind turbine wakes can be divided into near and far wake regions [17, 14]. The near wake is the area just downstream of the rotor up to one rotor diameter, where the effect of the rotor properties, including the blade aerodynamics and geometry determine the flow field. Near wake research is focused on the wind turbine's performance and the physics of power extraction. The far wake is the region beyond the near wake, where the details of the rotor are less important. The main interest in this area is the wake interference with other wind turbines (e.g. in a wind farm) or passing-by aircraft (wind turbine wake encounter). Here, flow convection and turbulent diffusion are the two main mechanisms that determine the flow field [17].

There are similarities between helicopter rotor wakes and wind turbine wakes. The vortex methods used for the analysis of helicopter wake problems can also be adopted for wind turbine wakes to represent the strengths and the spatial locations of the vortical wake elements that are trailed by each blade and convected downstream. Prescribed vortex wake models [8] have also been developed for wind turbine applications. Like the helicopter rotor wake cases, the models are usually based on the assumption of incompressible, potential flow, and experimental observations.

The CFD simulation of wind turbine wakes is an active area of research, and with increasing computer power, CFD simulations of wind turbine wakes obtained from Navier–Stokes (NS) equations are practical for near wake, however, far wake simulations need fine grid resolutions. Actuator disk [17, 14] and actuator line [16] methods have also been used to simulate the rotor and the rest of flow was simulated by solving the NS equations, which enabled the CFD domain to cover the region extending from rotor plane to several diameters downstream to study both the near and far wake development. Recently, CFD methods [4, 5] were used to study wake development and breakdown. These methods are very computationally expensive and require very fine grids to cover the far wake region. In most CFD wake studies, the flow conditions were treated as ideal. The effects of wind shear, terrain, ambient turbulence and temperature variation were ignored. This resulted in predictions that show much stronger and coherent vortices than would be expected, and the results represented a worst-case-scenario in terms of the wake properties.

Most of the wind turbine wake measurements in wind tunnels, reported in the published literature were focused on the near-wake due to technical challenges of the experimental setup. With the advance of LIDAR technology, field measurements are now possible, in which the near and far wakes could be measured. LIDAR measurements are, however, still rare and typically are not in the

public domain. LIDAR data is also highly dependent on the local atmospheric and environmental conditions. Since CFD simulations and wake models need to be verified with experimental data, the aerodynamic research on wind energy shifted towards a more fundamental approach based on experiments in controlled conditions. In the USA, the NASA/NREL unsteady aerodynamic experiments [17] of a full-scale rotor were conducted in the NASA-Ames 24.4m by 36.6m wind tunnel. The wind turbine was a two-bladed rotor with a diameter of 10m. In the NREL project, emphasis was put on measuring pressure distribution on the blades and hardly any wake measurements were conducted. In Europe, a similar project called MEXICO (Model rotor EXperiments In COntrolled conditions) was also conducted [15]. A three-bladed rotor model of 4.5 m diameter was tested in the DNW (German-Dutch wind tunnel). In addition to pressure measurements on the blade surface, wake velocity measurements with PIV (particle image velocimetry) were also carried out.

Flight simulation can play an important role in the prediction and severity evaluation of wake encounters by offering a safe, low cost and controllable environment to assess aircraft upsets following an encounter. However, wake encounter simulation has its own challenges. An accurate wake model is essential for the generation of wake velocity data. A validated aircraft flight dynamic model is necessary and the wake velocity data has to be carefully integrated into the simulation system to account for the interference of the wake on the aircraft flight dynamics when a wake encounter occurs. Piloted simulation trials are needed to subjectively assess the severity of wake encounters. In addition, high fidelity visual cues are also very important to reflect the real wake encounter scene.

The objectives of this project are:

- (1) To study and validate different numerical models for the generation of wind turbine wakes, from relatively simple prescribed wake models to free wake models and finally more complex CFD wake modelling.

- (2) To use the selected wake model to calculate the wake induced velocity field and integrate it into an aircraft flight dynamic model to carry out piloted wake encounter simulation trials in flight simulator.

- (3) To make recommendations regarding safe encounter distances for general aviation (GA) aircraft.

A wind turbine wake encounter study using engineering wake modelling, CFD, LIDAR field measurements and piloted flight simulations was carried out at University of Liverpool in cooperation with CAA, UK. The first results of this study are presented in this report.

Chapter 2

Wind Turbine Wake Modelling

Modelling wind turbine wakes requires accurate predictions and simulations of wake vortex geometry, wake breakdown, mean velocity deficits and wake induced velocity flow-fields. There are several wake models available in the literature [17, 14] with different levels of complexity and fidelity. Three wake models were used in this study. These were the Kocurek wind turbine wake vortex model [8], the velocity deficit wake model [7] and the CFD method [4, 5].

Wind turbine wakes can be divided into near and far wake regions [17]. Because there are similarities between helicopter rotor wakes and wind turbine wakes, the vortex method that is used for analysis of helicopter wake problems can be adopted to represent the strengths and the spatial locations of the vortical wake elements that are trailed by each blade and convected into the downstream wake. For example, the Kocurek prescribed vortex wake model [8] has been developed for wind turbine applications.

In this section, the Kocurek wind turbine wake model [8] is introduced and applied to the MEXICO wind turbine geometry. Then the validation of the Kocurek model with the PIV and the full CFD simulation was carried out.

The Kocurek wake model [8] was then applied to an approximation of the WTN250 wind turbine, which has been installed at the East Midlands airport in the UK. A LIDAR measurement of the WTN250 wind turbine wake is a parallel project that has been conducted at East Midland airport by the CAA, Sgurr Energy and University of Liverpool using Galion a LIDAR. The LIDAR data has been used for comparison with the CFD and the wake model results.

The wake velocity field data were generated by the Kocurek wake model at different wind speeds, thrusts and orientations with flight path. These velocity field data are implemented in the wind turbine wake encounter flight simulations.

2.1 Kocurek wind turbine wake vortex model

The wind turbine wake was first modelled using the modified Kocurek wind turbine wake vortex model [8] to capture the location and strength of the tip vortices. The Kocurek wind turbine wake vortex model was derived from the Kocurek-Tangler helicopter rotor hover wake model [9].

In the Kocurek-Tangler helicopter wake model, the wake vortex elements are positioned using analytical functions that give the axial settling and radial contraction rates in terms of basic inflow parameters. The tip vortex initially settles at a near constant rate until passing beneath the following blade, at which time the additional induced velocity from the second blade's bound vorticity and wake increase the settling rate. The radial contraction changes exponentially with increasing wake azimuth, reaching a minimum wake radius. The observed behaviour is represented by parametric equations in the wake azimuth increment, ψ_w , aft of the generating blade in the following form:

$$z/R = k_z \psi_w \quad (2.1)$$

$$r/R = A + (1 - A)e^{-\lambda \psi_w} \quad (2.2)$$

where k_z is the axial settling rate, λ is the construction rate parameter, and A is the developed wake radius.

However, for the wind turbine case, due to the wind, the trajectory rates will be changed significantly by the axial transport. The wake transport is attributed to both induced velocities and wind. In the extreme case of very high wind speeds, there will not be much induced flow effect because of the high pitch or settling rate of the wake spiral. In normal working conditions, it is assumed that the wind speeds are sufficiently high to require only mean induced effects to be included in describing wake trajectories. In addition, wind turbine wakes expand rather than contract as in the case of hovering helicopter wake.

For a wind turbine wake model, the task is to develop expressions for the axial and radial translation rates of the turbine wake. The above equations have to be modified to include the effect of wind speed, which will determine the rotor work states. The coordinate system for modelling wind turbine wake is shown in Figure 2.1.

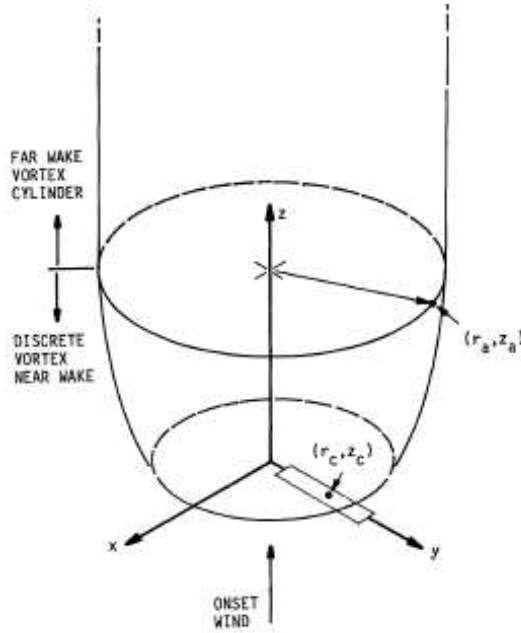


Figure 2.1: The coordinate system of the Kocurek wind turbine wake model.

There are three flow states defined by the axial impressed velocity v_a (corresponds to climb or descent rate for helicopter rotor) through the rotor. It is convenient to normalise velocity by the mean induced velocity value v_h in hover. Then the axial, induced and net velocity are given by:

$$\bar{v}_a = v_a/v_h \quad (2.3)$$

$$\bar{v} = v/v_h \quad (2.4)$$

$$\bar{v}_{net} = \bar{v}_a + \bar{v} \quad (2.5)$$

The normal state extends from hover through climb, $\bar{v}_a < 0$. The impressed and induced velocities are both downward. From hover to decent the rotor enters the vortex ring state in which the induced velocity is opposed to the descent speed. The streamline flow through the rotor no longer exists and a highly unstable recirculating flow developed about the rotor. The limits of the vortex ring state are $0 < \bar{v}_a < 2$. At further higher decent speeds, the rotor enters into the windmill brake state in which the streamline flow reorganises. This is the primary work state that wind turbines operate at.

In the normal and windmill brake states, the disk momentum theory is applicable because of the existence of a continuous stream-tube. This gives the mean induced velocity for the two states respectively as:

$$\bar{v} = -\bar{v}_a - [(\bar{v}_a/2)^2 + 1]^{\frac{1}{2}} \quad (2.6)$$

$$\bar{v} = -\bar{v}_a + [(\bar{v}_a/2)^2 - 1]^{\frac{1}{2}} \quad (2.7)$$

In the vortex ring state, because of the breakdown of the streamline structure of the flow, the induced velocity could only be generated from empirical relationships. An empirical model of apparent induced velocity is based on Castle and Gray [6] measurements of rotors in descent. The induced velocities in the vortex ring state are represented by the following two linear functions:

$$\bar{v} = -\bar{v}_a - 1, 0 < \bar{v}_a < 1.5 \quad (2.8)$$

$$\bar{v} = 3\bar{v}_a - 7, \bar{v}_a > 1.5 \quad (2.9)$$

$$(2.10)$$

The velocity relationships at three rotor work states are shown in Figure 2.2.

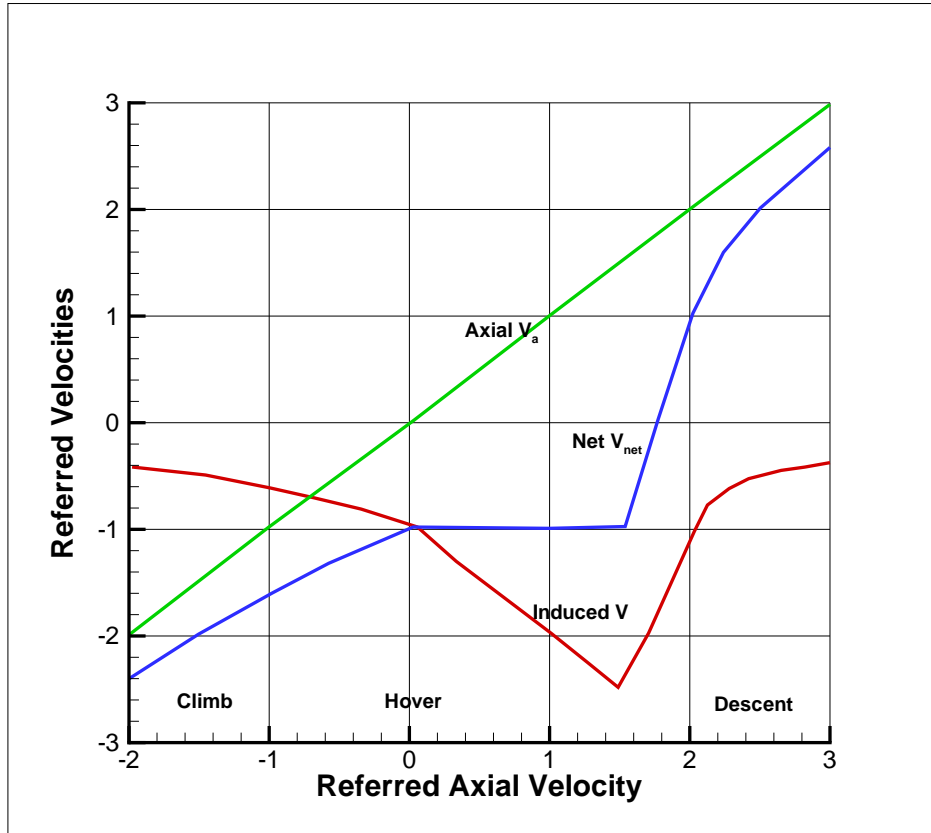


Figure 2.2: Rotor work state velocity relationships in axial flow [8].

The net settling rates are composed of an induced component and one due to the impressed axial velocity transport. $k_z = k_a + k_i$ where $k_a = v_a/(\Omega R)$ and k_i is proportional to the induced velocity and is determined by recognising that the pitch of the wake vortex helix is given by the settling rate and that the induced velocity varies inversely with the pitch.

For the normal and windmill brake work states, the normalised (by the hover settling rate) settling rate are expressed as:

$$\bar{k}_z = \bar{k}_a/2 - [(\bar{k}_a/2)^2 + 1]^{\frac{1}{2}} \quad (2.11)$$

$$\bar{k}_z = \bar{k}_a/2 - [(\bar{k}_a/2)^2 + (1 - \sqrt{2})]^{\frac{1}{2}} \quad (2.12)$$

In the vortex ring work state, the wake spiral is disorganised. It is assumed that the integrity of the wake spiral remains and its position nominally represents the overall circulation of the flow. The settling rate is also assumed to be proportional to the net flow. The settling rates in vortex ring work state are:

$$\bar{k}_z = -1, 0 < \bar{v}_a < 1.5 \quad (2.13)$$

$$\bar{k}_z = 4\bar{v}_a - 7, 1.5 < \bar{v}_a < 2 \quad (2.14)$$

The radial coordinate equation of the helicopter rotor wake is still used for the Kocurek wind turbine wake.

$$r/R = A + (1 - A)e^{-k_r(z/R)} \quad (2.15)$$

For a wind turbine, as the wake convects from upwind to downwind of the rotor, the radial character of the wake changes from contraction to expansion. To determine the wake radius A and rate K_r , the reference value of hover helicopter rotor $A=0.78$ is taken from the experimental measurements [8]. The rate parameter is assumed to be inversely proportional to the wake pitch which sets the radial induced velocities. These results the following equations:

$$A = 1 + 0.22[\text{sign}(k_z)] \quad (2.16)$$

$$k_r = k_{rh}/\bar{k}_z[\text{sign}(k_z)] \quad (2.17)$$

Now the cylindrical coordinates of the wake tip vortex can be determined by the equations

$$z/R = k_z(\psi_w - \psi_{te}) + (z_{te}/R) \quad (2.18)$$

$$r/R = (A + (1 - A)e^{-[k_{rh}(z - z_{te})/R]})/R \quad (2.19)$$

2.2 Validation of Kocurek wind turbine wake model

The Kocurek wind turbine model was applied to the MEXICO wind turbine, for which PIV wind tunnel measurements [15] and CFD simulations [4] were conducted.

The MEXICO wind turbine has a three-bladed rotor of 4.5m diameter. The model was designed for an optimum tip speed ratio of 6.7, reached at a tunnel velocity of 15 m/s. Three aerofoils: the DU91-W2-250, RISOE-A1-21 and NACA 64-418 were used for the rotor blades. In addition to the surface pressure measurements on the blades, PIV measurements were carried out to map the flow field in the DNW wind tunnel (see Figure 2.3). A traversing mechanism for the PIV was able to cover a region from approximately one diameter upstream to a little over one diameter downstream. Three wind tunnel speeds were set at 10, 15 and 24 m/s.

A CFD simulation of the MEXICO wind turbine was performed at UoL [4]. The CFD results (see Figure 2.3) showed good agreements of blade surface pressure distributions and flow field velocities to the wind tunnel measurements. However, there were discrepancies in the calculated thrust and the measured thrust. These were also reported by other authors [1].

In this section, the CFD and the measured thrusts are used in the Kocurek wind turbine wake model. The vortex circulation strength is dependent on the spanwise loading of the blade, the degree of the rolled-up of the tip vortex and changes induced by interference effects. The Beddoes circulation equation [2] was used to obtain the rolled-up tip vortex circulation Γ .

$$\Gamma/(cR\Omega) = 2.4c_T/\sigma \quad (2.20)$$

where $c_T = Thrust/(\rho\pi R^4\Omega^2)$, σ is the solidity of rotor blades, Ω is the rotation speed of the rotor and c is the chord of blades.

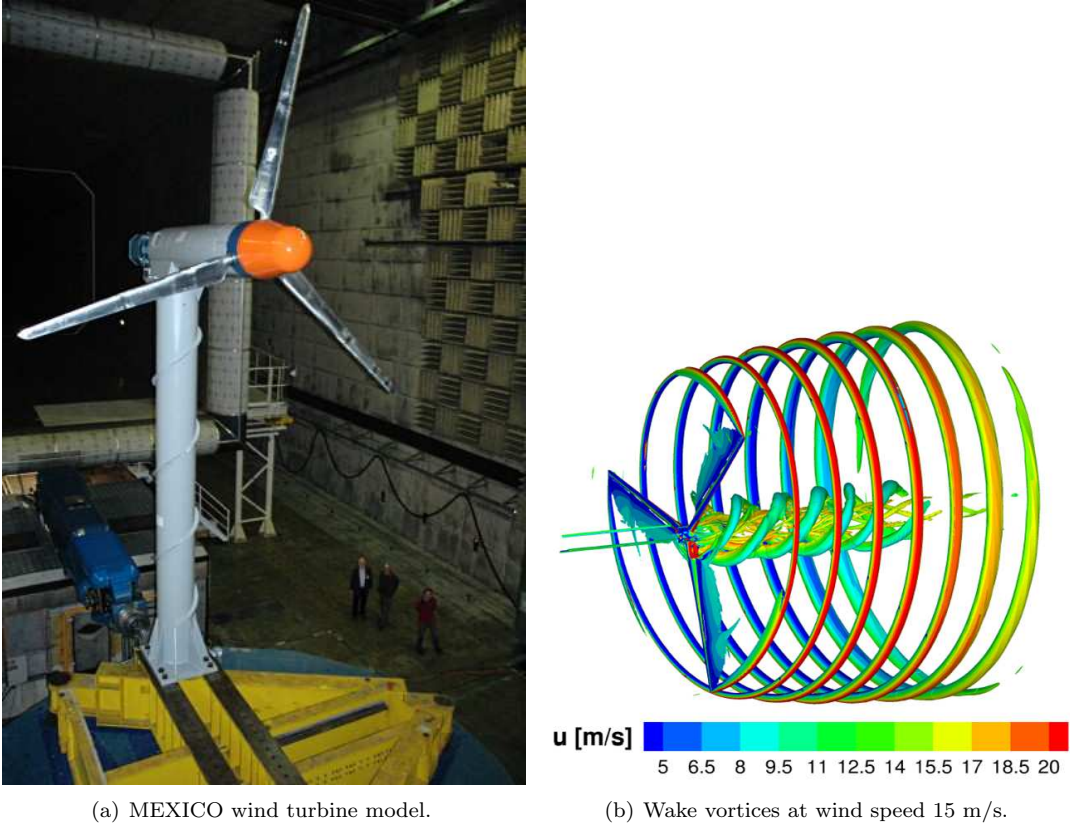


Figure 2.3: MEXICO wind turbine model and wake vortices of full CFD simulation at wind speed 15m/s [4].

The initial tip vortex core radius was set to be 5 percent of the blade chord ([2]). The core growth was determined by the following formula suggested in [10].

$$r_c(\psi_w) = \sqrt{r_0^2 + \frac{4\alpha\delta\nu\psi_w}{\Omega}} \quad (2.21)$$

where r_0 is the initial core radius; δ is the effective turbulent viscosity coefficient and α is a constant number of 1.25643.

The tip vortex structures generated by the Kocurek wind turbine wake model are shown in Figure 2.4. The top figure shows an iso-surface of vorticity which defines the tip vortex core structures and the contour plot at $y=0$ plane. The velocity contour plots at individual vortex elements are shown in the middle figure. Compared with the PIV measurements (the bottom figure), the individual vortex positions in the axial direction are accurately captured. The Kocurek model, however, over-predicts the radial position. So the use of helicopter rotor experimental data of the contraction and expansion parameters may require further testing.

The flow field velocity comparisons of the Kocurek model and the full CFD simulation are presented in figure 2.5. Two values of thrust, one is CFD calculated and the other is experimentally measured, were used to obtain the induced velocities. Both the w (axial) and u velocity components show good agreements when the measured thrust was used. The fluctuations in the CFD velocity components are absent in the results of Kocurek wake model due to its steady nature.

The flow velocity comparison at the other two wind speeds of 10 m/s and 24 m/s are shown in figures 2.6 and 2.7.

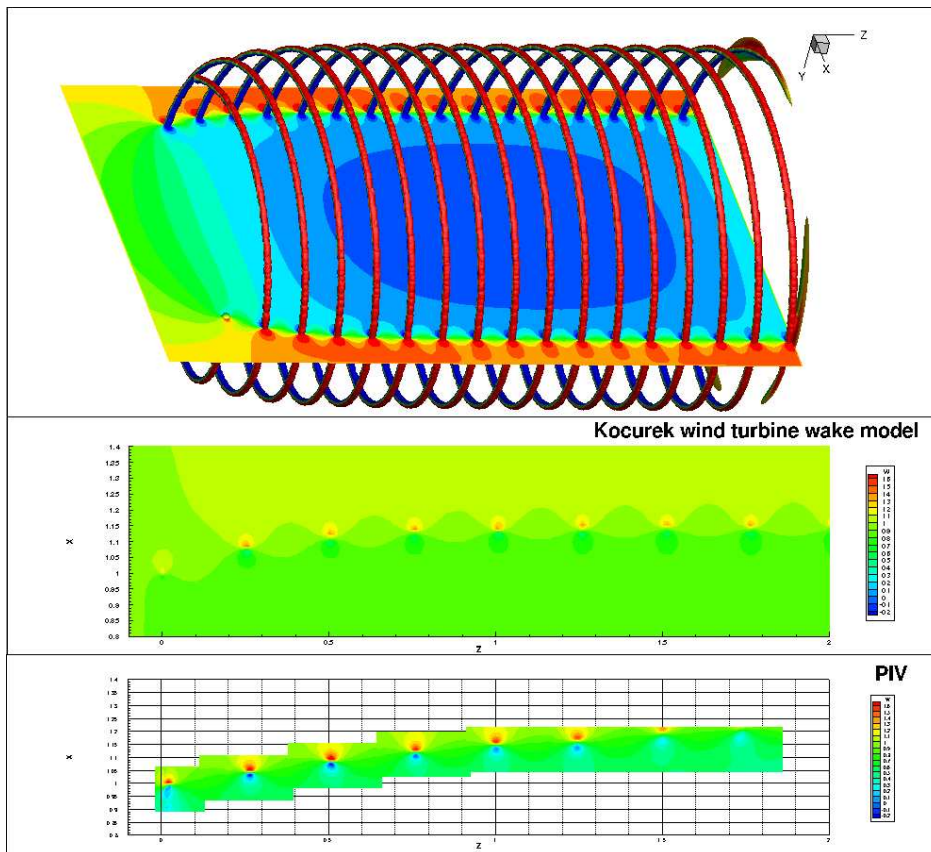


Figure 2.4: MEXICO wind turbine wake generated by Kocurek wind turbine wake model, wind speed 15 m/s.

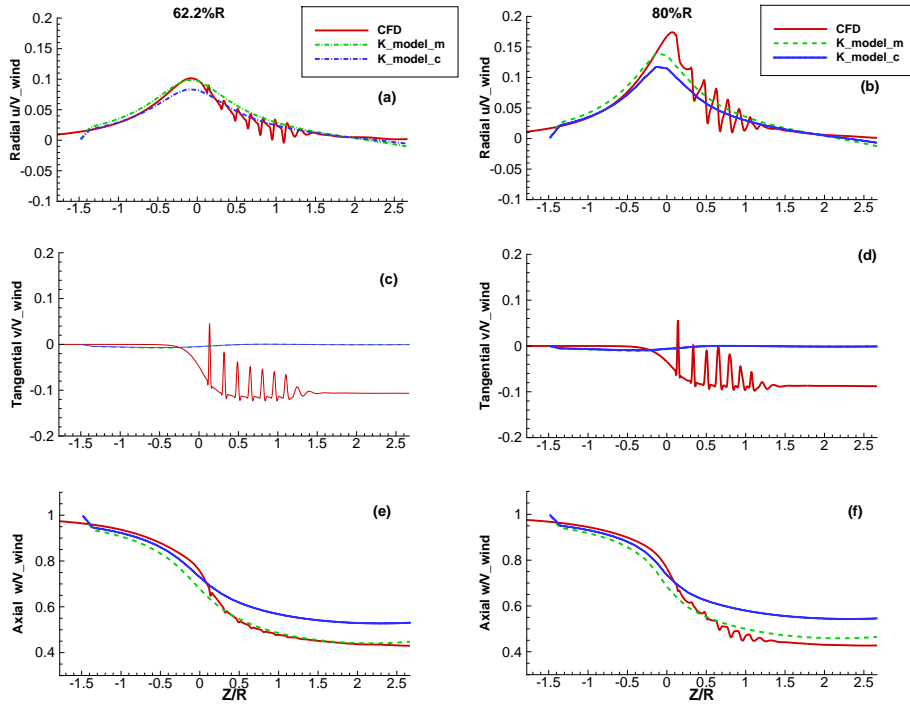


Figure 2.5: MEXICO wind turbine flow field velocity comparisons between CFD and the Kocurek wake model at a wind speed 15 m/s.

2.3 Wind turbine wake velocity deficit models

Wind turbine wake velocity deficit models are used in the wind energy industry to study wake interactions within a wind farm. These models are categorised into three families [17, 14]. The kinematic models are based on self-similar velocity deficit profiles and global momentum conservation. The wind turbine rotor thrust coefficient is the input. Wake growth is caused by ambient turbulence and the turbulence created by the shear in the wake. The field models use analytical forms of eddy viscosity to simulate turbulence and assume that the wake flow has axial symmetry. The boundary layer wake models consider the nonuniform atmospheric boundary layer and model turbulence transport via the $k - \epsilon$ model. The Park or Katic [7] model, which belongs to the kinematic model family, was used in this study to compare wind turbine wake velocity deficits with the LIDAR field measurements in the next section.

2.4 Wind turbine wake study by full CFD

At University of Liverpool, a full CFD method [4] was used with the HMB solver to study wind turbine wakes. The CFD results showed good agreement for the blade surface pressure distributions and flow field velocities with the wind tunnel measurements. The wake was then solved on a very fine mesh able to capture the wake vortices up to 8 radii downstream of the blades on the MEXICO wind turbine rotor. The location of the onset of instabilities and wake breakdown were predicted at wind speeds of 15 m/s and 10 m/s [5]. The CFD simulated wake vortices of the MEXICO wind turbine are shown in Fig. 2.8.

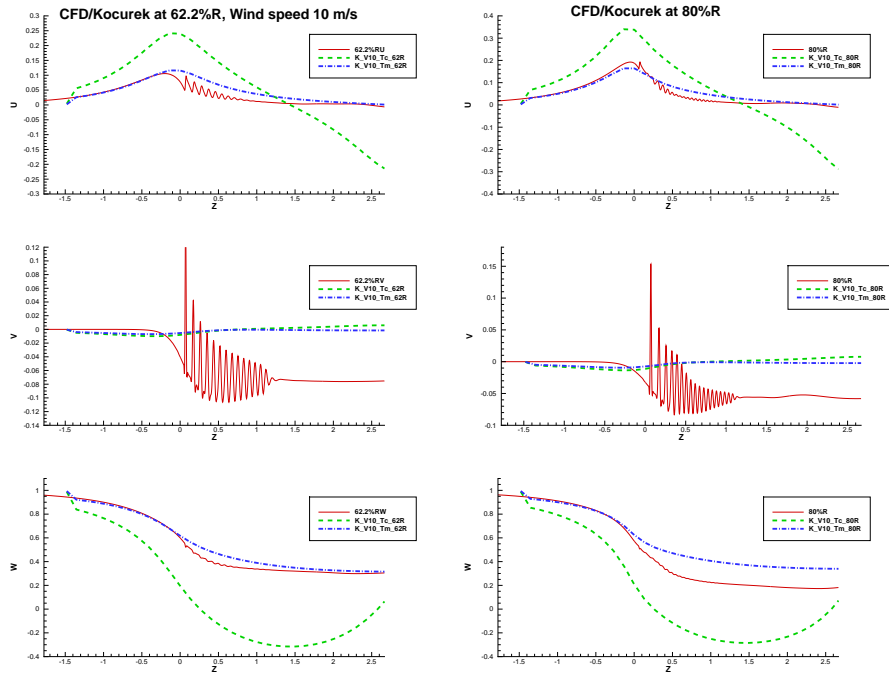


Figure 2.6: MEXICO wind turbine flow field velocity comparisons between CFD and the Kocurek wake model at a wind speed 10 m/s.

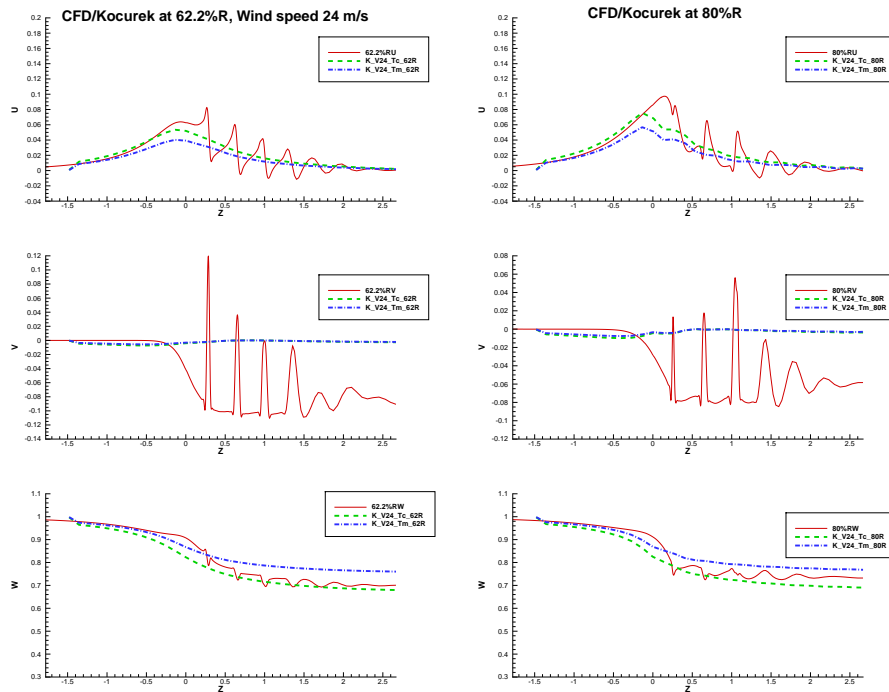


Figure 2.7: MEXICO wind turbine flow field velocity comparisons between CFD and the Kocurek wake model at a wind speed 24 m/s.

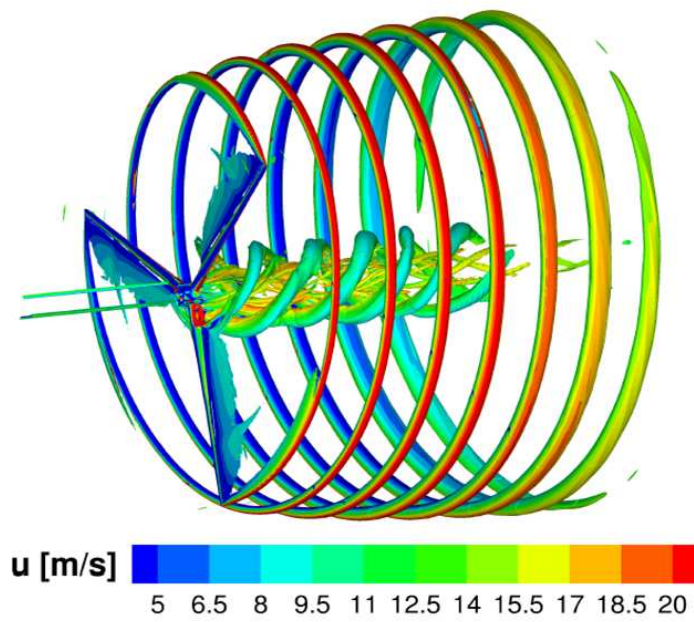


Figure 2.8: MEXICO wind turbine wake generated by the full CFD, wind speed 15 m/s [5].

Chapter 3

LIDAR Wind Turbine Wake Measurement Campaign

A wind turbine wake LIDAR measurement campaign, coordinated by the CAA was conducted in addition to the wind turbine wake modelling and wake encounter simulations at the University of Liverpool. Sgurr energy was selected as the LIDAR system provider and technical supporter for this project.

Two WTN250 wind turbines installed at East Midland airport (Figure 3.1) were used for LIDAR measurements. An on-site visit and meeting was held on 08/08/2013. The relevant people from CAA, Surge energy, UoL and EMA attended the meeting and visited the wind turbine site. Figure 3.2 of the East Midland aerodrome shows that the wind turbines were installed on the south side of the runway at a distance about 22.5 rotor diameters (675 m) from the runway. This distance is longer than that indicated in the current guideline on wind turbine separation distance.

Several locations for installation of the LIDAR were proposed and the final site was decided after several rounds of discussion. The ideal LIDAR position should be on the nacelle of the wind turbine, where the wake can always be captured regardless of the incoming wind direction. However, it was not possible to obtain the planning permit from the wind turbine operator and manufacturer to install the LIDAR device on the nacelle in a short period of time. The selected site (Figure 3.3) was located on the northern slope of the runway, about 868m from the wind turbines, where there was a nearby power station available for supplying power to the LIDAR sensor system. The LIDAR set-up was carried out by Surge energy engineers on 06/02/2014. A finer re-adjustment of the scan set-up was conducted on 24/02/2014 to maximise the resolution of the scan plane. A second scan plane re-adjustment was carried out on 13/03/2014 to extend the scan plane to cover the wind turbine's near wake region after the initial scan data analysis showed that the wake field was not well captured by the first scan set-up.

3.1 WTN250 wind turbines and historical wind data at East Midlands airport

The wind turbines installed at East Midlands airport are WTN250 wind turbines and were the first wind turbines installed in the vicinity of an airport in the UK. The WTN250 wind turbine has a 3-bladed up-wind stall regulated rotor. The rotor diameter is 30 m and the rotor speed is 40 rpm. A diagram of the WTN250 wind turbine is shown in Figure 3.4. The technical data of the WTN250 wind turbine are summarised in Table 3.1 (see www.windtechniknord.de).

An on-line survey of the weather historical data in the East Midlands region indicated that over the entire year, the proportions of the wind blowing from the south, south-east and south-west are 16%, 5% and 20%, respectively (Figure 3.5). The fraction of time spent with the wind blowing from different directions on a daily basis is shown in Figure 3.5. Over the course of the year typical wind speeds vary from 1 m/s to 9 m/s, rarely exceeding 14 m/s (high wind) (Figure 3.7).



Figure 3.3: The final LIDAR site.

Table 3.1: WTN250 wind turbine technical data

General	
Nominal Output	250 KW
Number of blades	3
Rotor Shaft	Horizontal
Rotor Arrangement	Upwind
Hub Height	30 m or 40 m
Power	
Cut in wind speed	4 m/s
Rated wind speed	14 m/s
Power at 10 m/s	175.5 KW
Rotor Arrangement	Upwind
Cut off wind speed	25 m/s
Max shaft power	300 KW
Rotor and Blade	
Diameter	30 m
Swept area	707 m ²
Rotor speed	40 rpm
Blade material	Glass fibre
Blade length	13.39 m

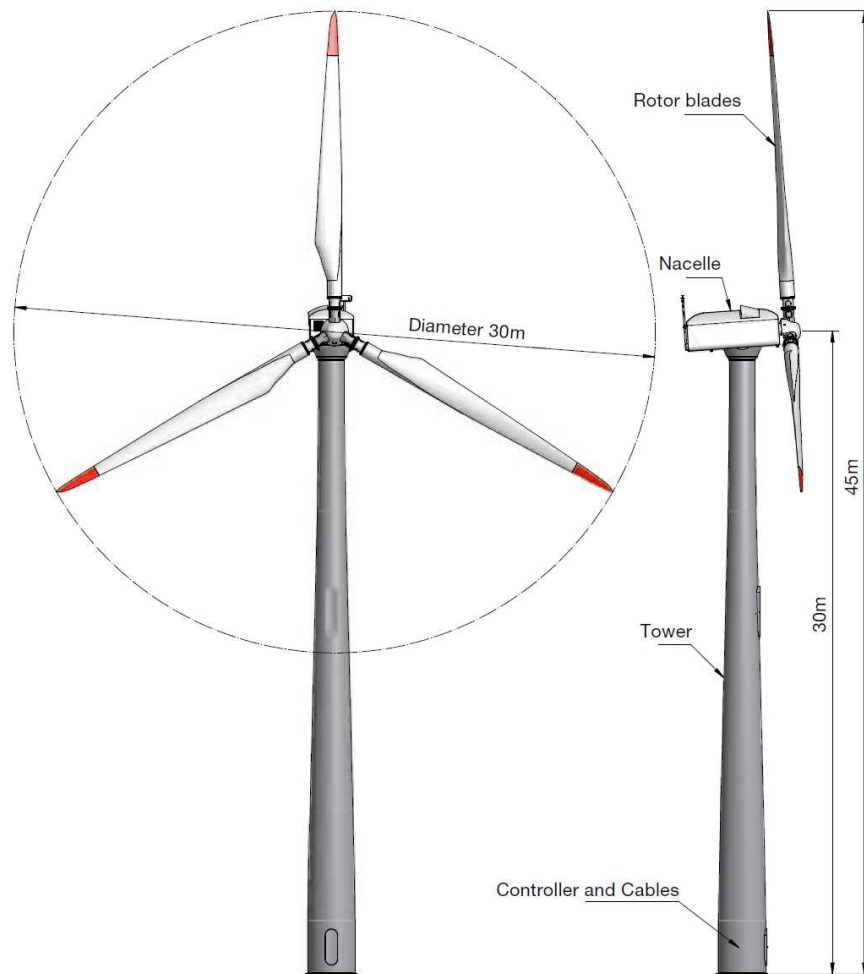


Figure 3.4: Diagram of the WTN250 wind turbine.



Figure 3.5: Wind direction over the entire year.

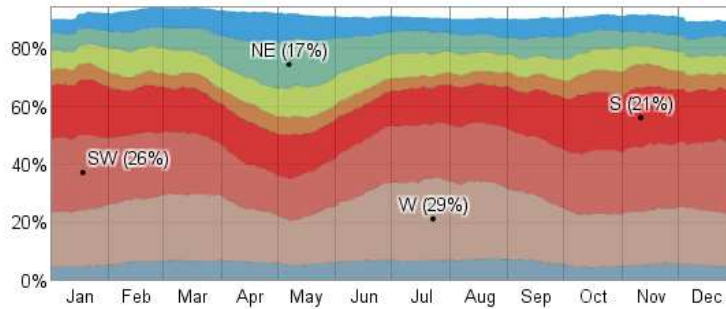


Figure 3.6: Fraction of time with the wind blowing from the various directions on a daily basis.

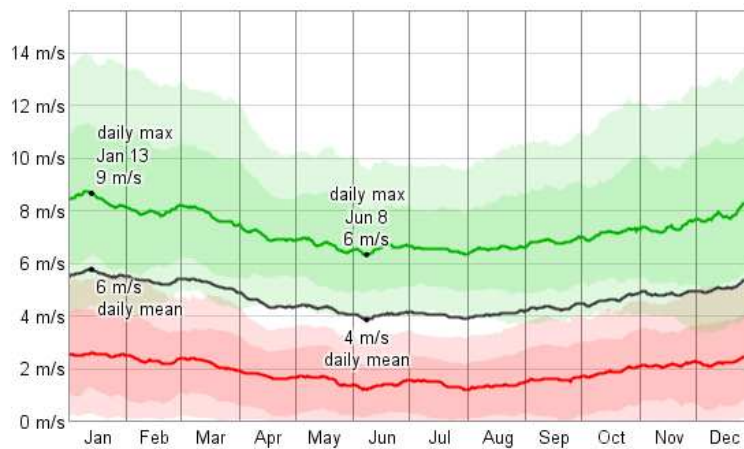


Figure 3.7: Average daily minimum (red), maximum (green) and average (black) wind speed with percentile bands.

3.2 Galion LIDAR and Set-up

The Galion G4000 (Figure 3.8) operated by Sgurr Energy was selected as the tool to measure the wind turbine wake. The Galion is characterised as a second generation LIDAR device capable of varying the measurement beam in azimuth and/or elevation. It can provide an all sky scanning capability and up to 4km range. The emitted laser beam is in the form of a pulsed laser with a frequency of 20kHz. The distance is calculated from the time of flight of each range gate which in turn controls

measurement points. An overlapping technique is used to refine the measurement resolution. The Galion LIDAR is shown in Figure 3.9 as located on-site.



Figure 3.8: Galion LIDAR of Sgurr Energy.

Position Plane Indicator (PPI) scan or Arc scan was used in this campaign to measure the wind turbine wake flow. A PPI scan is indicated in Figure 3.10, where multiple beams are used to build a detailed picture of the flow field over the designed region.

The locations of Galion LIDAR and the wind turbines are indicated on the map as shown in Figure 3.11.

The final refined scan region is shown in the Figure 3.12. In the first scan set-up, the radial length is 300m, which covered an area from 478m to 778m. This gave 100 measurement points per-ray. In the second refined scan set-up, the radial length was extended to 400m, which covered an area from 478m to 878m, giving 133 measurement points per-ray. A 3m overlapping of range-gate in the radial direction was used for all the scans to increase the measurement resolution.

For both set-ups, the scan plane included 25 rays in azimuth covering a narrow band of azimuth angles from 180.694° to 186.454° at an interval of 0.24° .

The WTN250 wind turbines at EMA are an example of a relatively small wind turbine. The above scan set-ups produced wake measurement with a spatial resolution of 3m by 3m, which is at Gallion LIDAR's extreme measurement limits.

3.3 LIDAR data processing

The daily Galion scan data was stored in 24 sub-directories. Each sub directory corresponded to hourly scanned data sets. A single scan took 30 sec (300m range) or 35 sec (400m range). So a one-hour scan produced 105 or 95 scan data files.

Each scan data file contains the following columns of data:

Range-gate Doppler Intensity Time Az El Pitch Roll

where the range-gate is the radial range of each measurement point represents. The coordinates (x,y,z) of each measurement point can be constructed from the range-gate, azimuth(Az) and elevation (El) parameters using the following equations. The line (ray)vector is first calculated based on the LIDAR set-up. Here, the *FFSET* is the overlapping distance which is 3.0m; the *RANGE_GATE_SIZE* is 30m for the Galion LIDAR and the *STANDOFF_DISTANCE* is 463.0m, which is the radial distance from the starting measurement point to the LIDAR location in each ray.



Figure 3.9: The on-site Galion LIDAR.

The flow velocity V_{line} is calculated from the Doppler signal which gives the line of sight velocity (the velocity along the ray). The horizontal velocity V_h at each measured point can also be calculated from the Doppler, azimuth and elevation.

$$vec = range_gate * OFFSET + RANGE_GATE_SIZE/2.0 + STANDOFF_DISTANCE \quad (3.1)$$

$$x = vec * \cos(El) * \sin(Az) \quad (3.2)$$

$$y = vec * \cos(El) * \cos(Az) \quad (3.3)$$

$$z = vec * \sin(El) \quad (3.4)$$

$$V_{line} = Doppler \quad (3.5)$$

$$V_x = V_{line} * \cos(El) * \sin(Az) \quad (3.6)$$

$$V_y = V_{line} * \cos(El) * \cos(Az) \quad (3.7)$$

$$V_z = V_{line} * \sin(El) \quad (3.8)$$

$$V_h = \sqrt{V_x^2 + V_y^2} \quad (3.9)$$

The *Intensity* signal is used to determine the backscatter light quality. If the intensity is lower than 1.01, the measured velocity at the point is not regarded as reliable and should be screened out. The *pitch* and *roll* data are used only for the Galion beam set-up and are not used in the velocity calculations.

The current LIDAR set-up makes the scan plane fixed in the downwind region of the wind turbine and can only capture the wind turbine wake flow fully when the wind is blowing from the south. It

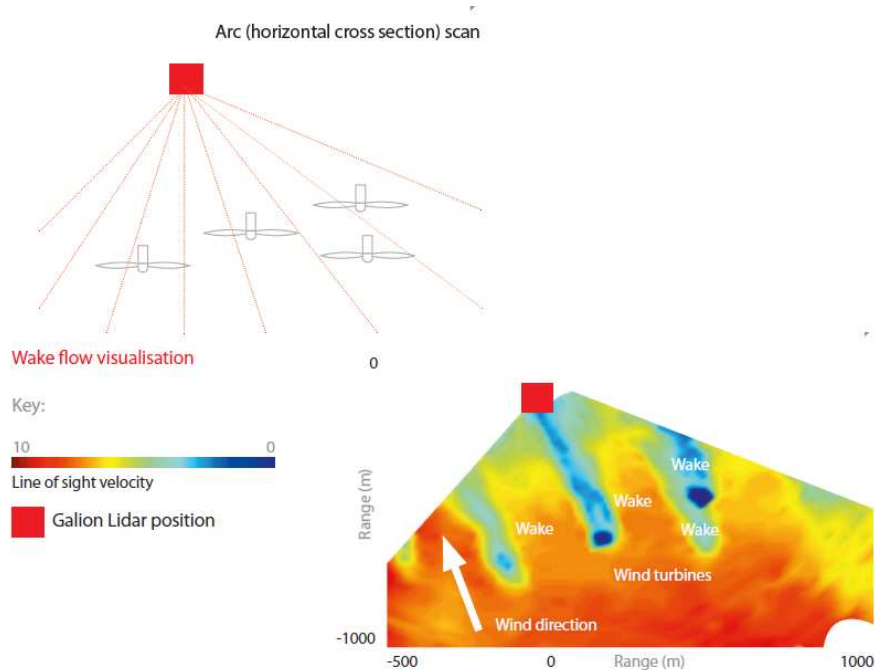


Figure 3.10: Schematic of the PPI or Arc scan for wind turbine wake measurements.

can also capture partially the wake if wind is blowing from south-east or south-west. Hence the scan data is only useful for these ideal wind directions. The wind turbine cut-off wind speed is 4m/s which means that only when the speed is above 4m/s the scan data is meaningful.

A wind screening processing is therefore required to pick up the meaningful scan data. This screening process needs the local weather data of the wind speed and direction. The Meteorological Aerodrome Report (METAR) reports of EMA, which records the weather condition of the airport, are accessible on-line. The report can provide the half-an-hour averaged wind data in EMA. However, it was later found not to be very accurate. The wind turbine anemometer wind data, the so-called Supervisory Control And Data Acquisition (SCADA) systems on modern wind turbines is required for the wind screening. Unfortunately, the SCADA was not used or was not available at EMA. The wind data measured by two on-site anemometers was available. The location of one of the anemometers (on site B) is close to the Galion LIDAR unit. It provided the ten-minute statistic wind data to determine the wind conditions.

3.4 Results and discussion of the LIDAR campaign

3.4.1 Results of the LIDAR campaign

Because the scan region was set at the north of the wind turbine, the wind direction was restricted to a narrow band of 170° to 220° to capture a meaningful wake flow field. The wind speed range was also limited by the wind turbine's cut-off wind speed of 4 m/s (7.8 kt). Therefore, the valid scan datasets are for those wind directions between 170° to 220° and speed is larger than 7.8 kt. These datasets are listed in Table 3.2.

Wind turbine wakes are characterised by reduced mean wind speeds (velocity deficit) and wake turbulence. The current LIDAR scan can only capture the mean velocity deficits. Because the wind direction and speed constantly change with time; statistics of the measured data is more appropriate to represent the velocity deficits. In the wind industry and weather forecast, ten-minute, half-hour and one-hour data is widely used.



Figure 3.11: Locations of Galion LIDAR and the wind turbines.

Some typical LIDAR scans of the WTN250 wind turbine wake is presented in Figures 3.13, 3.14 and 3.15, where the LIDAR measured Line of sight (Los) velocities during 14:00 to 15:00 on 07-04-2014 are plotted. The METAR wind data recorded that the overall wind direction was 190° and speed was 17 kt at 14:20 in EMA, and at 14:50, the overall wind direction was 200° and the speed was 18 kt. The one-hour averaged LIDAR wake measurement is shown in Figure 3.16. The estimated location of wind turbine (the location was changed with wind direction as the rotor was turned into the incoming wind direction) as well as the arcs of one-diameter to five-diameter from the rotor hub were indicated in the figure. The one-hour statistic data reveal that the wake velocity deficit was recovered to approximately 10% of the free-stream wind speed at a downstream distance of 5D. Note that on the right side of the wind turbine, there is a long low-speed contour bar that extends to about to 2.5D in downwind. This is caused by the LIDAR laser reflections on a solid or solids (most likely the blades, nacelle or supporting tower) in the gate-range (30 m for current set-up). The velocity measurements in this region were distorted without any physical meanings. This phenomenon is quite common in LIDAR near wake measurements. The location of this distorted contour bar is random. In some cases, there were more than one distorted contour bars in the near wake velocity contour plots. Considerations must be taken to these near wake distortion areas to avoid any distraction from the measured data. This also proves that in any future LIDAR campaign, a "better" LIDAR system is needed with a capacity of measuring the near wake flow velocity accurately without any distortions

Although these ten-minute averaged mean velocity contours revealed different shapes of the wake velocity, the measurements indicated that statistically the mean velocity deficit was recovered to the free-stream wind speed in the downwind area about 5D from the rotor.

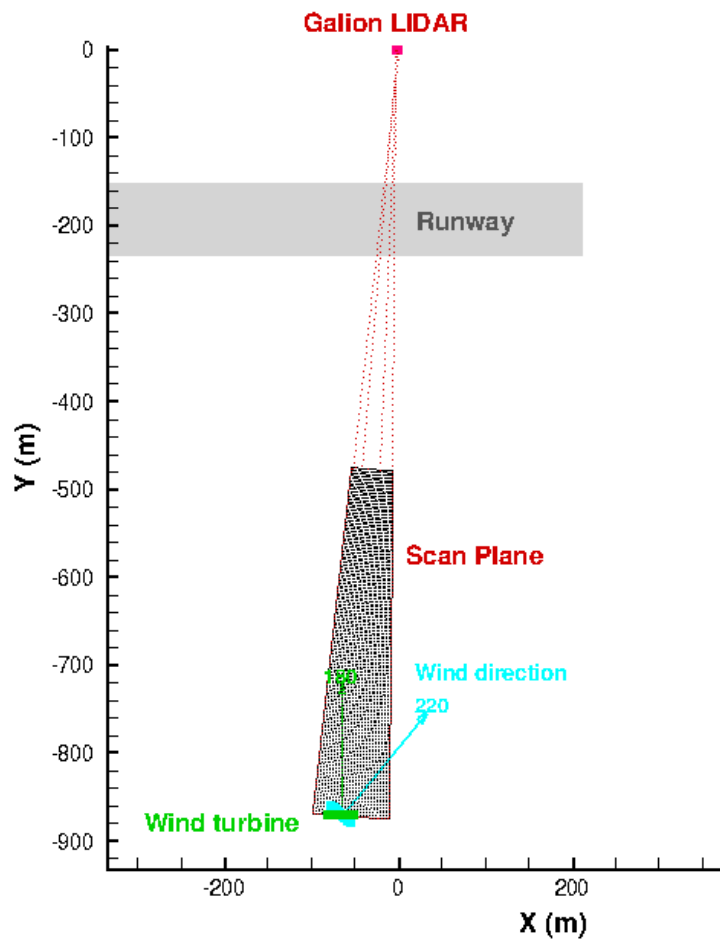


Figure 3.12: The refined scan plane used in the LIDAR measurement.

Table 3.2: Valid LIDAR datasets

Date	Time	Wind direction	Wind speed
07/04	00 - 14	170 - 210	8 - 18
06/04	00 - 23	190 - 220	10 - 20
05/04	04 - 23	190 - 210	8 - 17
24/03	10 - 18	170 - 190	11 - 17
21/03	17 - 23	190 - 220	13 - 19
20/03	02 - 16	210 - 220	11 - 25
19/03	21 - 22	220 - 220	19 - 22
09/03	20 - 23	210 - 220	8 - 11
09/03	00 - 17	180 - 220	8 - 13
08/03	07 - 23	170 - 200	9 - 17
07/03	00 - 07	210 - 220	17 - 21
06/03	00 - 23	200 - 210	9 - 18
02/03	00 - 23	170 - 220	8 - 20
27/02	00 - 06	180 - 190	14 - 22
26/02	00 - 10	210 - 220	12 - 15
26/02	18 - 23	180 - 220	9 - 16
25/02	00 - 20	180 - 220	8 - 20

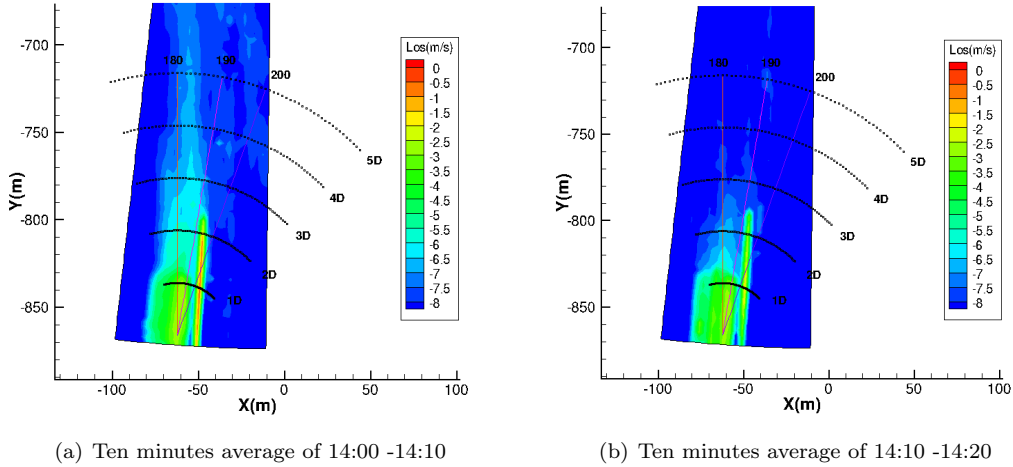


Figure 3.13: Ten-minutes averaged line of sight velocity measured on 07-04-2014.

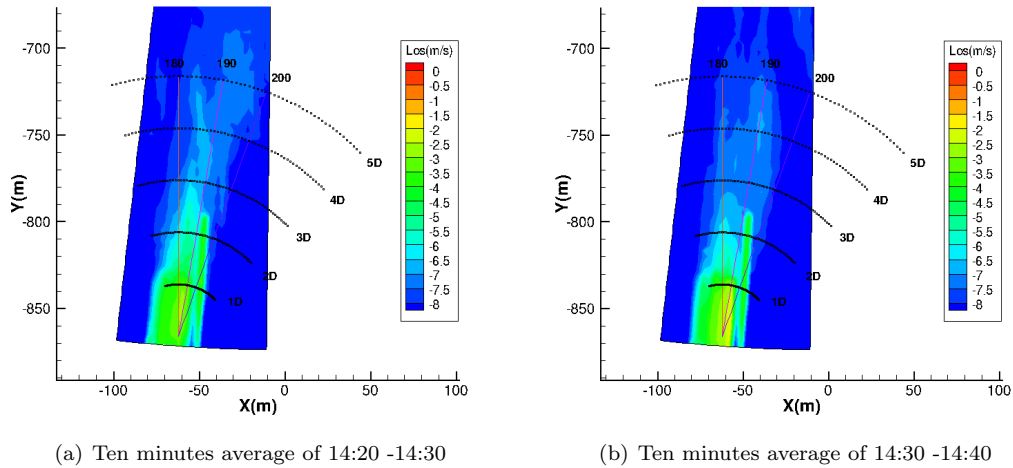


Figure 3.14: Ten-minutes averaged line of sight velocity measured on 07-04-2014.

3.4.2 Comparisons of the LIDAR measurements

The LIDAR measurement was first compared with the full CFD results [5], indirectly, as the full CFD method was applied to the MEXICO rotor in an uniform inflow. At wind speed of 15 m/s, the MEXICO rotor tip speed ratio is 6.67. The full CFD results [5] revealed that wake vortices instability started at a position of about 2.5D downstream of the rotor and the breakdown occurred in the downstream region from 3D to 4D. The mean velocity in the wake was about 9.5 m/s at the hub height (63% of the free stream wind speed) at 5D downstream. As a reference, at a wind speed of 10 m/s, the WTN250 wind turbine tip speed ratio is 6.3, close to that of the full CFD case.

The Park [7] wake velocity deficit model was applied to the WTN250 wind turbine at the wind speed of 10 m/s and the results are shown in Figure 3.17. The Park model predicted the mean velocity deficit recovered to 10% of the free stream wind speed at about 4D. As in the full CFD case, in these models the effect of wind shear, terrain and ambient turbulence were not taken into account.

The Kocurek wind turbine wake model was also applied to the WTN250 wind turbine geometry to

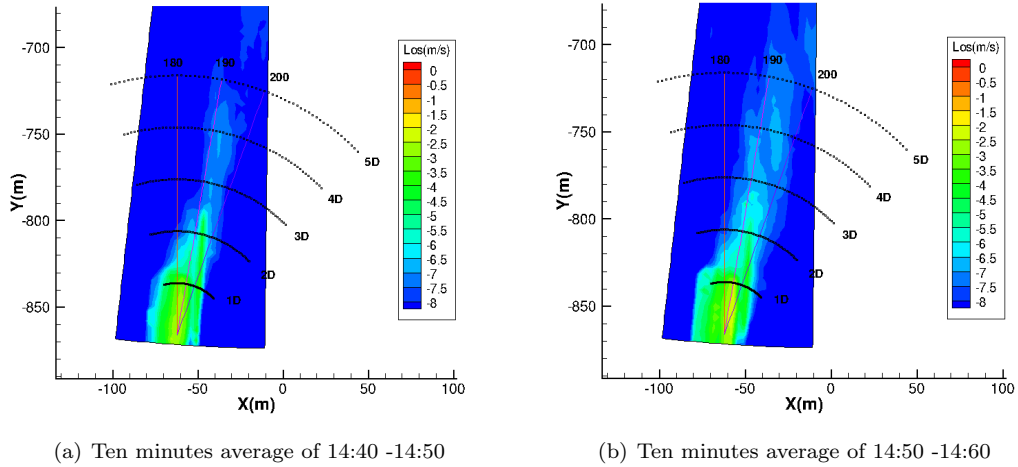


Figure 3.15: Ten-minutes averaged line of sight velocity measured on 07-04-2014.

generate the induced velocity fields. The induced velocities generated by the Kocurek and the Park models were projected to the scan plane along the ray directions. The velocity contours are shown in Figure 3.18. The mean velocity results of the Park model are close to the LIDAR measurements, while the Kocurek wake model over-predicted the velocity deficits in far wake region. If the induced velocities predicted by Kocurek wake model were used in flight simulations, it can be considered as the worst case scenario.

In general, the LIDAR measurements captured the regular wake mean velocity patterns. Statistic LIDAR data indicate that the effects of wind turbine rotor wake, in term of velocity deficit, are limited within a downwind distance of 5D. This is generally in agreement with the results of the full CFD method and the velocity deficit models.

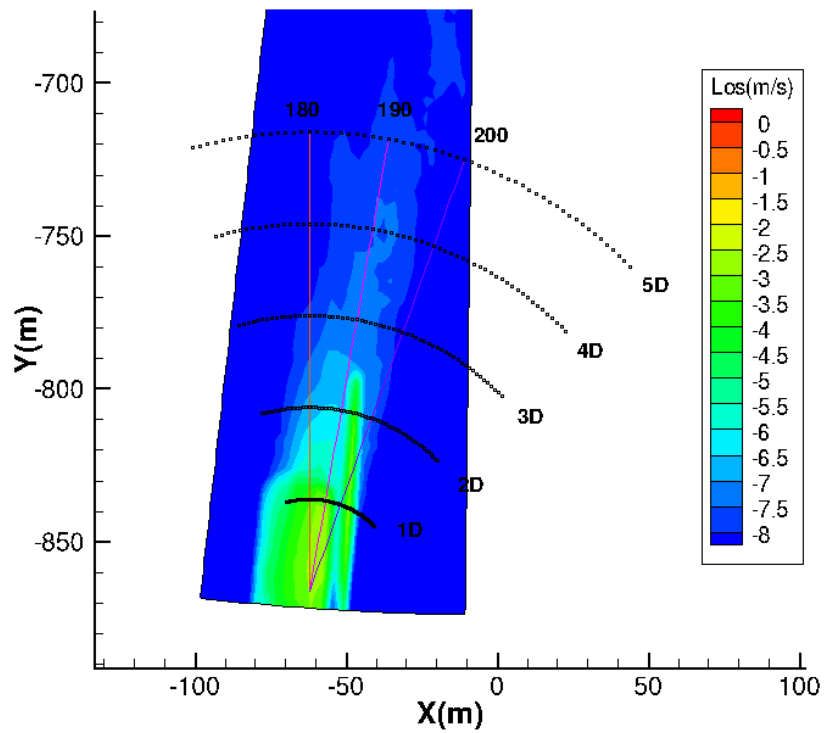


Figure 3.16: One-hour averaged Line of sight velocity measured on 07-04-2014.

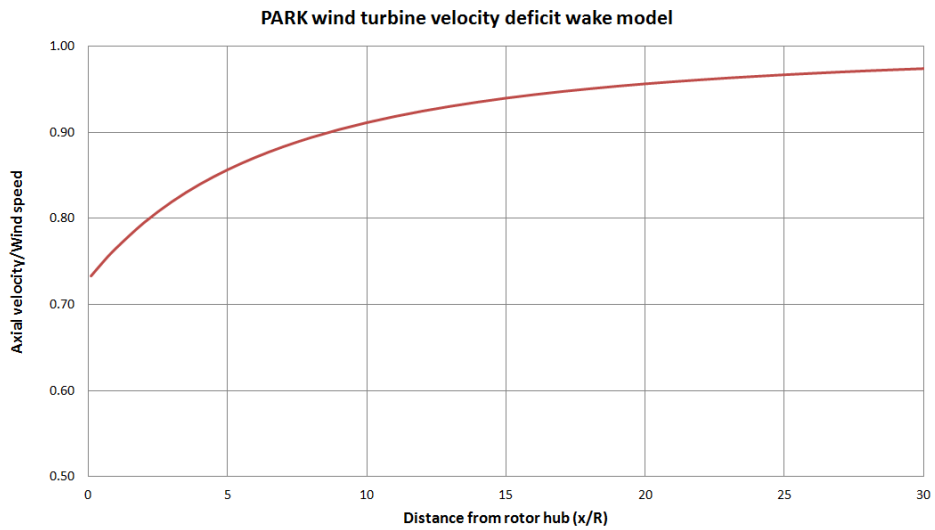
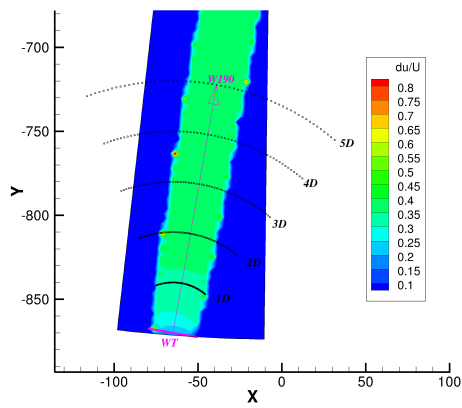
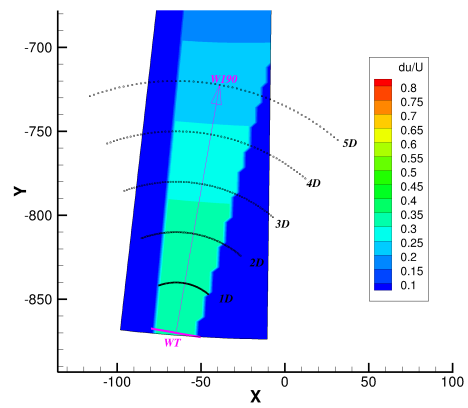


Figure 3.17: Wake velocity deficits using the Park wake model for an approximate WTN250 wind turbine at a wind speed of 10 m/s.



(a) Kocurek wake model



(b) Park wake velocity deficit model

Figure 3.18: Predicted line of sight velocity contours in the LIDAR scan plane.

Chapter 4

Flight Simulation of Aircraft Encounter with Wind Turbine Wakes

4.1 Wind turbine configurations and wind turbine wake encounter scenario

The 4.5 m diameter MEXICO wind turbine might be considered too small to be used as a wind turbine model for wake encounter flight simulation assessments. Hence the NREL wind turbine, which is a two-bladed rotor with a diameter of 10m, was therefore initially selected. The Kocurek wind turbine wake model was applied to the NREL wind turbine geometry to generate the induced velocity fields. The parameters of the NREL wind turbine used in the wake generation are listed in Table 4.1.

Table 4.1: NREL wind turbine wake encounter simulation matrix.

Parameters	Used in simulations
Wind turbine	NREL
Number of blades	2
Radius of rotor (m)	5
Thrust (N)	709.6, 2065.6, 2870.8, 3481.43
Wind speed (m/s)	5.0, 10, 13.07, 21.13
Height (m)	10, 20
Orientation angles	45°, 90°
Offset	1.5D, 3D, 6D, 10D
Rotation speed (rpm)	72

The perceived wind turbine wake encounter scenario is for a light General Aviation (GA) aircraft approaching an airport, where a wind turbine is located nearby. On the approach to landing on the runway, the aircraft passes through the wind turbine wake field and is upset by the wake encounter. The severity of this encounter was investigated using piloted flight simulations. Two wake encounter scenarios are shown in figures 4.1 and 4.2, where the crossing (90°) and oblique (45°) wake encounters are illustrated.

The second candidate wind turbine used in the piloted simulations was the WTN250 wind turbine. The parameters of the WTN250 wind turbine were presented in the previous section.

LIDAR measurements of the WTN250 wind turbine wake were obtained at East Midland airport by the CAA, Sgurr Energy and University of Liverpool. So it is considered more appropriate to

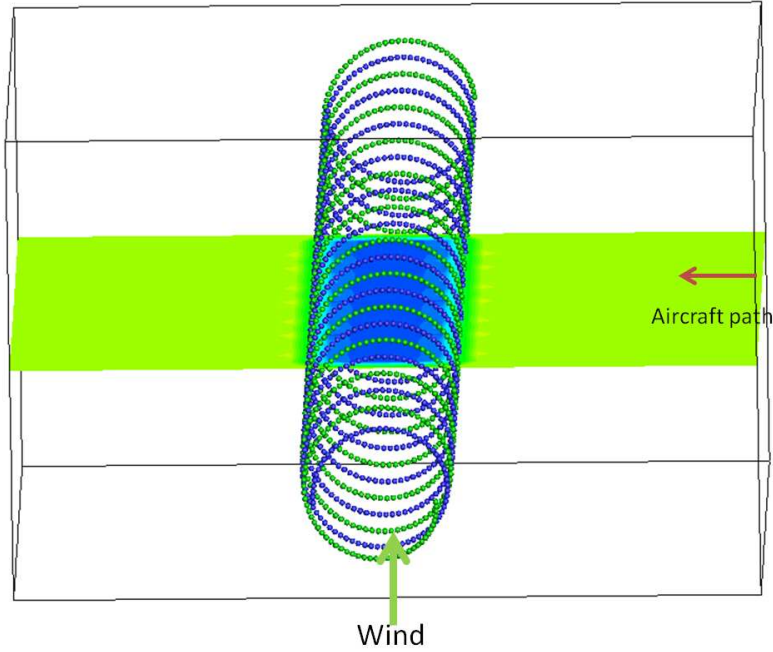


Figure 4.1: NREL wind turbine wake crossing encounter.

use the WTN250 wind turbine configuration for the wake generation and encounter simulation. The Kocurek wind turbine wake model was applied to the WTN250 wind turbine geometry to generate the induced velocity fields. Based on the wind historical data, the WTN250 wind turbine simulation matrix was planned and is listed in Table 4.2. The thrust was estimated from the rated power output of 175.5 kw at wind speed of 10 m/s. For other wind speeds the thrusts should be calculated from momentum theory. Here, the objective is not to match the WTN250 wind turbine itself, but to use it as a representative of the small wind turbines with power output less than 250 KW that could be installed near an airport in future.

Table 4.2: WTN250 wind turbine data used for the wake encounter simulation matrix.

Parameters	Used in simulations
Wind turbine	WTN250
Number of blades	3
Radius of rotor (m)	15
Thrust (N) (at 10m/s)	20288
Wind speed (m/s)	10
Height (m)	31.5
Orientation angles	45°, 90°
Offset	1.5D, 3D, 6D, 10D
Rotation speed (rpm)	40

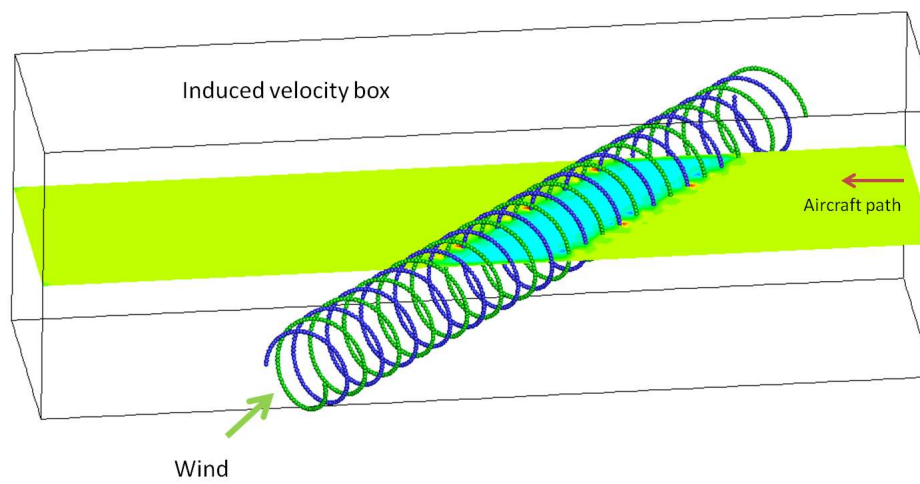


Figure 4.2: NREL wind turbine wake oblique encounter at 45 deg.

4.2 Description of the flight simulator

The simulator used in the trials was the HELIFLIGHT simulator [13] shown in Figures 4.3 and 4.4. It is a full motion simulator with a single seat cockpit. It uses a 3 channel collimated visual display for the Out-the-Window view and two chin-window displays. Pilot controls are provided by a four-axis dynamic control loading system. It has a six DOF full motion platform and the pilot is able to communicate with the control room at all times via a headset.



Figure 4.3: External view of the simulator.



Figure 4.4: Internal view of the HELIFLIGHT simulator.

4.3 Pilot wake vortex severity rating scale

During the trials, the pilot was asked to give feedback on the wake encounters. This feedback took the form of a short questionnaire and used a pilot rating scale, that was developed in a previous study by Padfield [12]. The ratings scale is shown in Figure 4.3. It provides a decision tree that enables the pilot to provide a subjective assessment of the wake encounter in terms of effect of the encounter on the aircraft states and the pilot’s ability to recover.

4.4 Wind turbine trial matrices

The wind turbine wake encounter simulation trials were carried out using two test pilots and two student pilots. The wake velocity data of a generic small wind turbine with 250 KW power output, which is approximately based on the parameters of the WTN250 wind turbine, were integrated into the flight simulation environment. The crossing (90°) and oblique 45° to the centreline of the runway wake encounter scenarios were simulated. The wind turbine rotor hub was positioned at a height of 100 ft above the ground and at several offset distances from the centreline of the runway. The pilots were asked to fly a simulation of a GA aircraft at two altitudes of 100 ft and 150 ft along the runway to penetrate the wind turbine wake, simulating the crossing and oblique wake encounters.

The wake induced velocity field should have a finer grid to make sure that for each aerodynamic computing point on the GA, there are enough data points for interpolation. The comparison of the dimension of the induced velocity grid and the geometry size of the aircraft is shown in Figure 4.6, where a sketch was used to represent the size of the encountering aircraft.

A constant wind speed of 10 m/s was used in the simulation for the wake generation. In some simulation sorties, the pilots were asked to hold the controls during the encounter to measure the maximum attitude and altitude deviations without interventions of pilot.

4.5 Simulation results

The wind turbine wake encounter simulation trials were carried out at different stages with different test pilots. The first trial was conducted by a CAA test pilot. In later trials, another test pilot and two student pilots were invited to carry out some test items. All the wind turbine wake simulation items and results are listed in Tables 4.3, 4.4, 4.5 and 4.6.

For each condition, the time histories of the aircraft attitude angles, rates and accelerations of roll, pitch and yaw, the pilot’s control activities of the lateral, longitudinal sticks and the pedal, the vertical height of aircraft and the body accelerations in x, y and z body axes were plotted in the figures.

Table 4.3: Test matrix of simulation 2, test pilot 1; time: 25-06-2013

Sortie	Height	Angle	Offset	Pilot Ratings
14 - 15	150	90	3D	A
16 - 17	150	90	1.5D	A
18	150	45	1D	B
19 - 20	150	45	1D	Hands-off
21 - 22	150	90	1D	B
68 - 69	150	45	3D	A
70	150	45	3D	Hands-off
71	150	45	1.5D	B
72	150	45	1.5D	Hands-off

Table 4.4: Test matrix of simulation 2, test pilot 2; time: 28-06-2013

Sortie	Height	Angle	Offset	Pilot Ratings
73 - 74	150	45	1.5D	B
75	150	45	1.5D	Hands-off
76 - 77	100	45	1.5D	B
78	100	45	1.5D	Hands-off
79 - 80	100	90	1.5D	B
81	100	90	1.5D	Hands-off
82 - 83	150	90	1.5D	B
84	150	90	1.5D	Hands-off
85 - 86	100	90	3D	B
87	100	90	3D	Hands-off

Table 4.5: Test matrix of simulation 3, test pilot: Student pilot 1; time: 29-09-2013

Sortie	Height	Angle	Offset	Pilot Ratings
23 - 25	150	90	1.0D	B/C
26 - 27	150	45	1.0D	A

Typical time history plots of the aircraft responses and pilot control activities during the wind turbine wake encounter are shown in Figure 8. The same parameters of simulation with the pilot controls fixed are shown in Figure 8. In this case, the pilot flew the GA aircraft through the WTN250 wind turbine wake at the height of the wind turbine rotor center (100 ft) in the crossing encounter. The wake generated minor upsets on the GA aircraft and a severity rating B was awarded for this encounter, indicating that the excursion of aircraft states is minor.

Table 4.6: Test matrix of simulation 4, test pilot: Student pilot 2; time: 15-10-2013

Sortie	Height	Angle	Offset	Pilot Ratings
18 - 19	100	90	1.0D	B
20 - 21	150	90	1.0D	B
22 - 23	100	45	1.0D	A
24	150	45	1.0D	A

Wake Vortex Severity Rating Scale

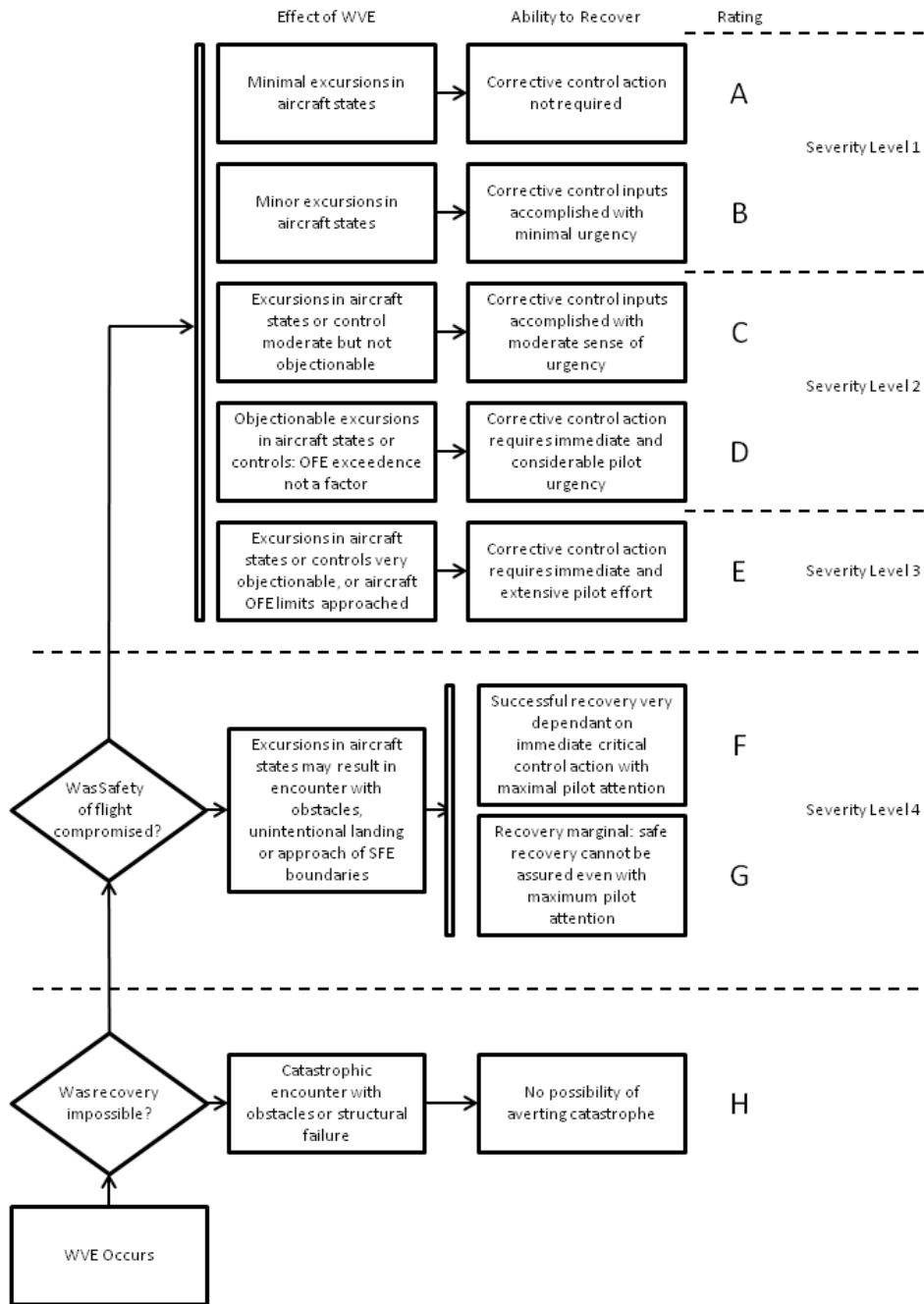


Figure 4.5: Wake Vortex Severity Rating Scale [12].

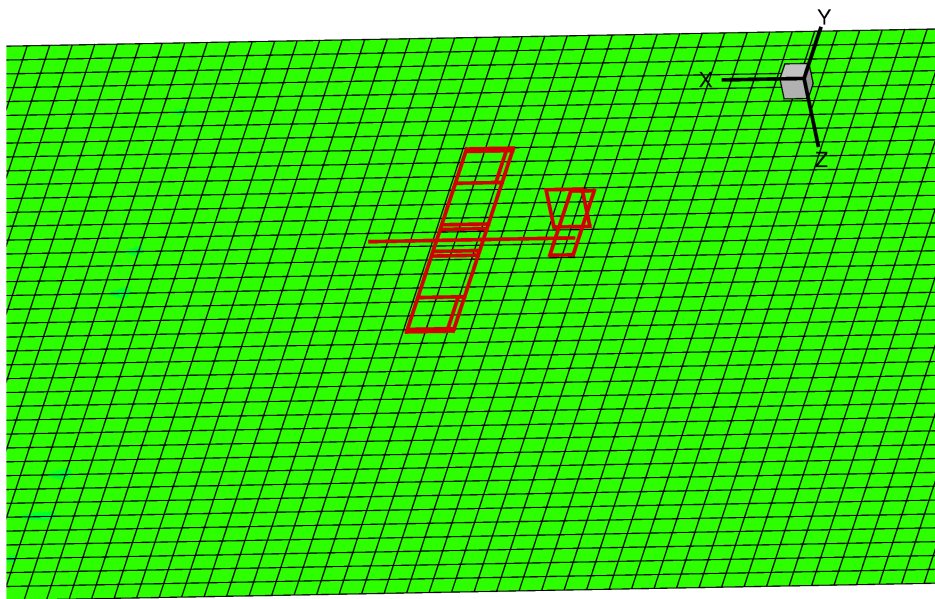


Figure 4.6: Comparison of the dimension of the induced velocity grid points and the size of a GA geometry.

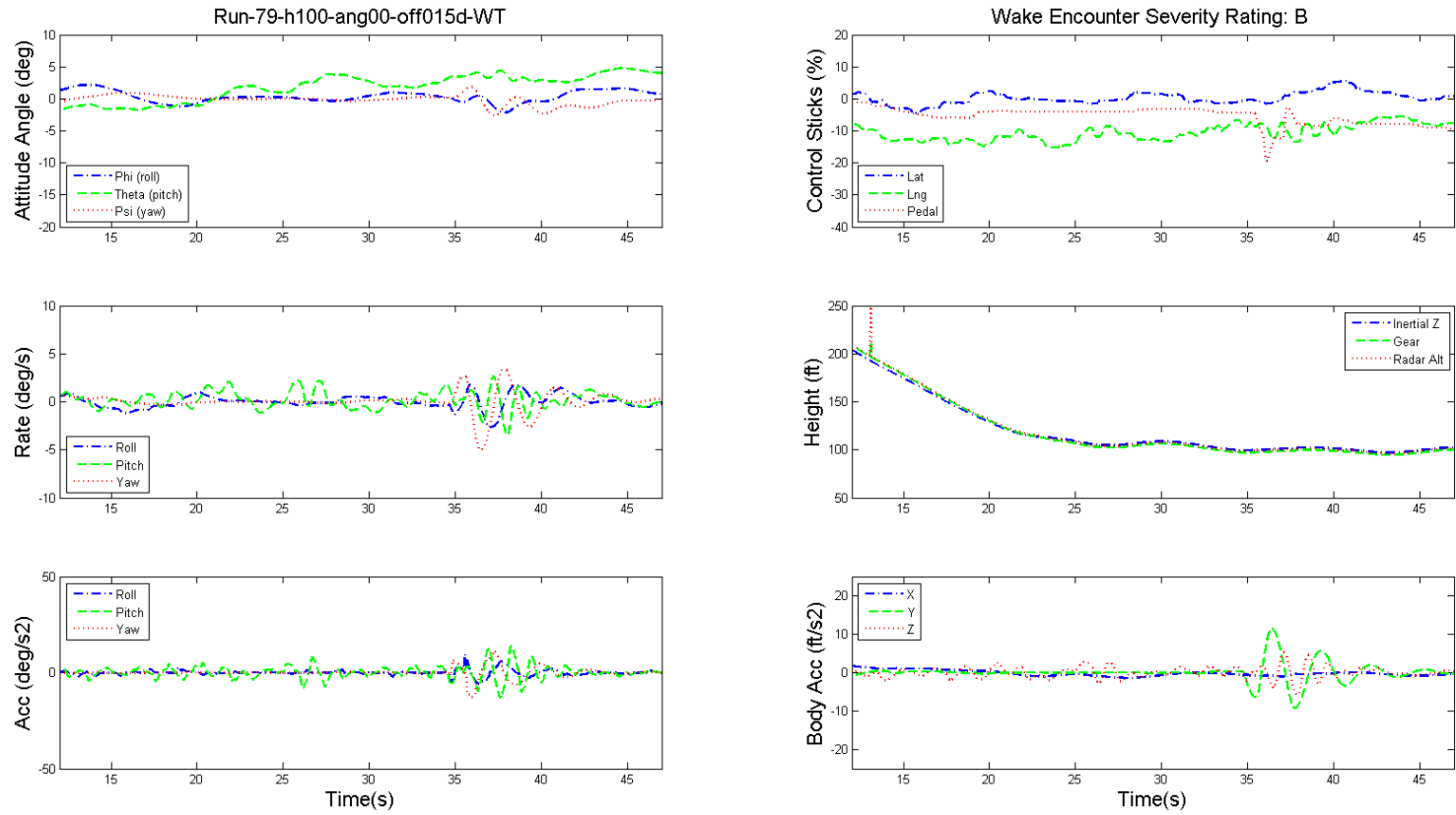


Figure 4.7: Time history of the dynamics of GA aircraft and pilot's controls during wake encounter, wind turbine hub height 100 ft, wind speed 10 m/s, angle 90.0, offset 1.5D.

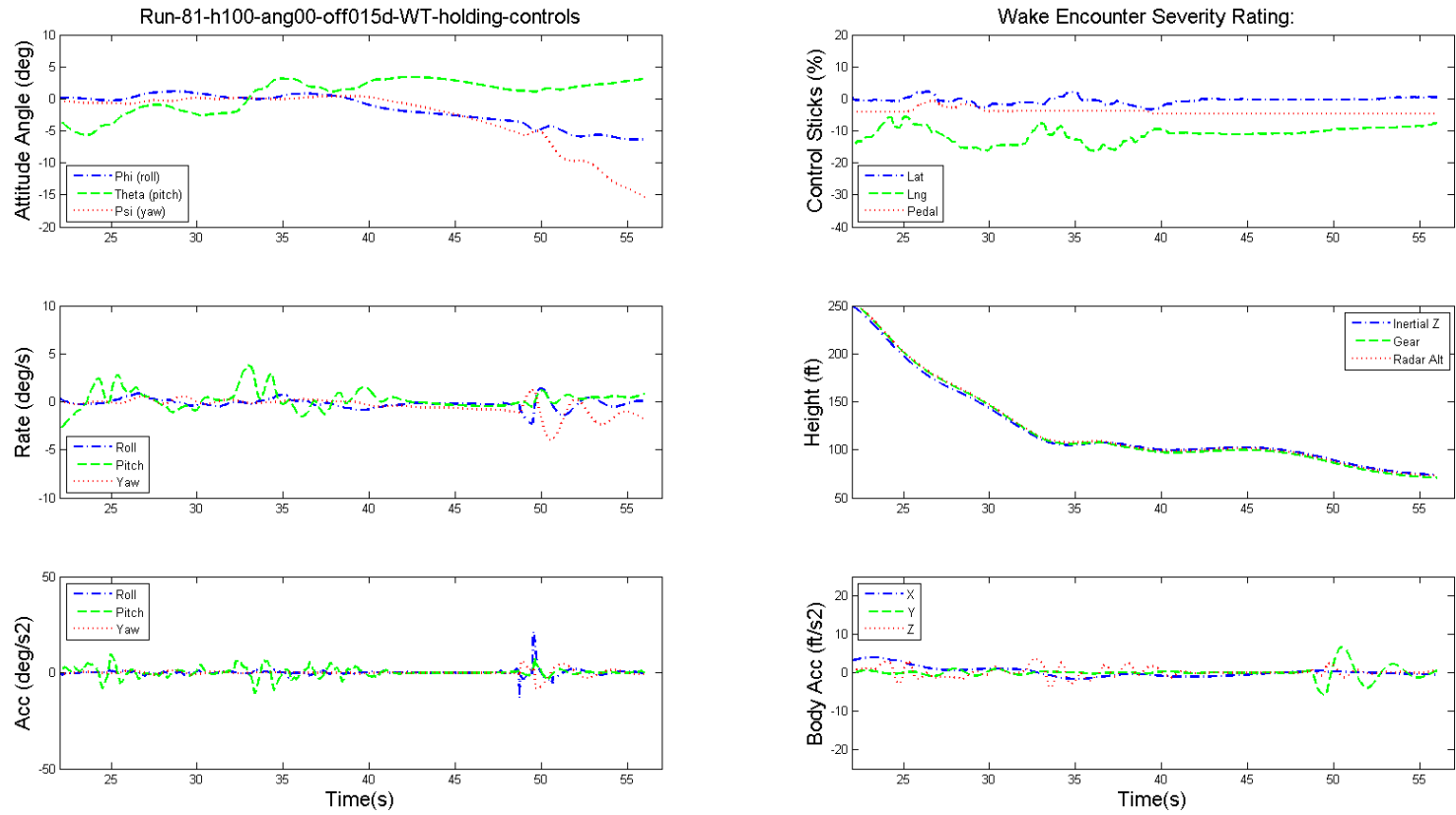


Figure 4.8: Dynamics of GA aircraft and pilot's controls during wake encounter, wind turbine hub height 100 ft, wind speed 10 m/s, angle 90.0, offset 1.5D, pilot's control holding.

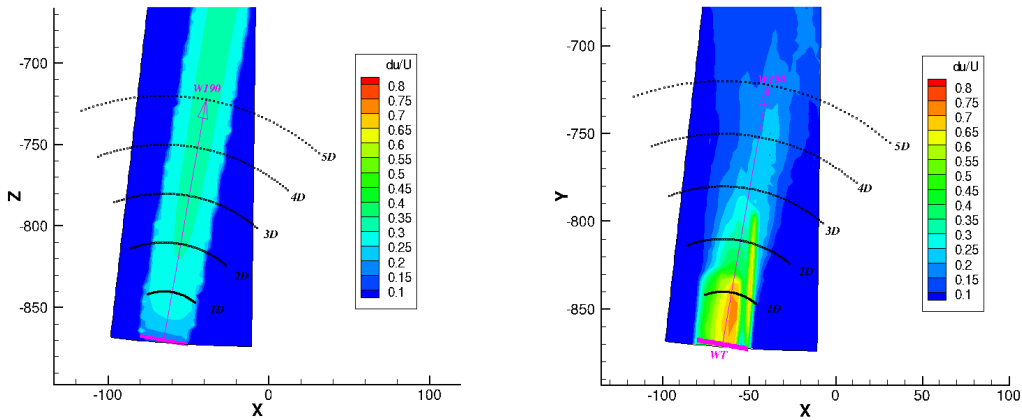
4.6 Discussion of simulation results

For the current wind turbine wake encounter scenario, the wake upsets on the encountering light aircraft were mild, in general, even if the aircraft was flying through the wake at a close distance. The wake mainly generated yaw disturbances on the aircraft which caused a yaw angle deviation no more than 10 deg. Normally only minor corrections were needed from pilots to rectify the flight path, and the B to C severity rating were awarded by the pilots.

The most significant disturbances caused by a wind turbine wake is in its axial direction and manifested as a velocity deficit in the downwind region. Although the wake vortices also caused disturbance velocities in the radial and vertical direction, they are smaller than the axial disturbance velocity. The fluctuation of these velocities, which can be seen in the full CFD simulation, were not captured in the current wind turbine wake model as the model is only for steady cases. So when the aircraft flew across or at some oblique angles through the wind turbine wake, there were only spatial axial velocity gradients that had impact on the aircraft's flight dynamics, in which case the disturbances exert side-forces on the aircraft which cause its yaw angle changes when it entered and left the wake region.

It can be imagined that if a helicopter encounters the wind turbine wake in the same fashion, the responses of the helicopter and pilots would be different due to different flight dynamics. In this respect, simulation of a helicopter encountering wind turbine wake might be more appropriate and interested.

The wake velocity deficits generated by the Kocurek wind turbine wake and measured by LIDAR were compared in Figure 4.9. At the same wind direction of 190° , the relative velocity deficits predicted by the Kocurek model are much larger than that measured by LIDAR, especially in the downstream region beyond $2D$ from the wind turbine rotor. In order words, a worse-case scenario was considered in the piloted flight simulations.



(a) Wake velocity deficits generated by the Kocurek wind turbine wake (b) Wake velocity deficits measured by LIDAR

Figure 4.9: Comparison of the relative wake velocity deficits.

Chapter 5

Off-line Flight Simulation of Wind Turbine Wake Encounter

5.1 Analysis of wind farm wake impacts on general aviation airport in the Kansas report

Recently, an analysis of wind farm turbulence impacts on a general aviation airport in Kansas, USA was reported [11]. Wind farms have been installed near the Rooks county regional airport and the Pratt regional airport in Kansas, USA. The helical vortex model was used to simulate the wind turbine wake and the aircraft wake decay rate in the atmosphere was used to model the wind turbine wake decay. Roll hazard and crosswind hazard index analyses of the wind farm on a small general aviation aircraft were detailed in the report. The roll hazard analysis showed that for the Rooks county regional airport, the potential roll hazard index is in the high range as far out as 2.84 miles. For the Pratt regional airport, the roll hazard index is in the high range as far out as 1.14 miles. In the high gust of 40 mph wind, the crosswind hazard analysis indicated that the turbine wake induced crosswind, results in identifying the majority of runway areas as high hazard areas at both of the airports.

The wind turbine rotor used in the report had a diameter of 300ft. the circulation of the wind turbine wake helical vortex was calculated based on small wind turbine wind tunnel measurements at the highest wind speed of 40 mph (58.67 ft/s). The calculated circulation might be too strong when compared with the results from other established methods for the wake vortex circulation [2]. The highest wind speed would not necessarily produce the highest thrust (or circulation) as the wind turbine would be pitch regulated to reduce its power output to the rated value as the wind speed is too high. This would result in less thrust at high wind speeds.

5.2 Off-line analysis of WTN250 wind turbine wake encounter

The analysis presented in the previous section was adopted and applied to the WTN250 wind turbine, together with the wind turbine wake modelling methodology introduced in the last chapter, to generate wind turbine wake flow for the off-line analysis.

In the off-line analysis, the GA aircraft was set to fly at different positions relative to the wind turbine location. The aircraft was first put outside the wake flow field and trimmed initially at a flight condition of 70 kts, as used in the piloted flight simulations, and then all the body states were frozen during the off-line simulations. The total forces and moments on the aircraft can be obtained by summing all the forces and moments on the individual components. The variations of forces or moments when the aircraft was outside and in the wake flow, can be used as an indication of the wake disturbance and the wake encounter severity of wind turbine wakes on an aircraft. Compared with the piloted flight simulation, the dynamic responses and the pilot controls and re-trimming were excluded in the off-line tests, which represent the quasi-steady acceleration as if the aircraft were instantaneously placed in the wake.

As mentioned in the chapter two, the initial wake vortex core is set to be 5 percent of the averaged chord [2, 10]. for the WTN250 wind turbine configuration, the initial wake vortex core is about 39 mm. The PIV measurements and CFD simulation results of the MEXICO wind turbine indicated that the vortex core size might be 2 to 4 times larger than the above estimated value [4]. In the off-line analysis the enlarged core size (20 percent chord) was also used to consider the worst-case-scenario.

For the WTN250 wind turbine rotor of 30m diameter, at a wind speed of 10 ft/s, the circulation is $7.8m^2/s$ according the Beddoes formula. While the method in the Kansas report produces a circulation of $85.33m^2/s$.

The decay of local wake vortex circulation Γ_i after time t can be calculated by

$$\Gamma_i/\Gamma_0 = \exp(-Ct\Gamma_0/(2\pi b_0^2 T_c)) \quad (5.1)$$

where Γ_0 is the initial circulation, b_0 is the vortex span, and C is a constant of 0.45.

T_c is determined by

$$\epsilon^*(T_c)^{4/3} = 0.7475 \quad (5.2)$$

$$\epsilon^* = 2\pi b_0/(\Gamma_0(\epsilon b_0)^{1/3}) \quad (5.3)$$

where ϵ is the turbulent intensity. For a high turbulence case at the turbulent intensity of 10%, ϵ is 0.01.

The final circulation decay is

$$\Gamma_i/\Gamma_0 = \exp(-Ct(\epsilon\Gamma_0)^{1/4}/(0.956(\pi)^{1/4}b_0)) \quad (5.4)$$

The wake vortex circulation decay curves are shown in Figure 5.1 for the cases of using the Beddoes and the Kansas formula to calculate the initial wake vortex circulations.

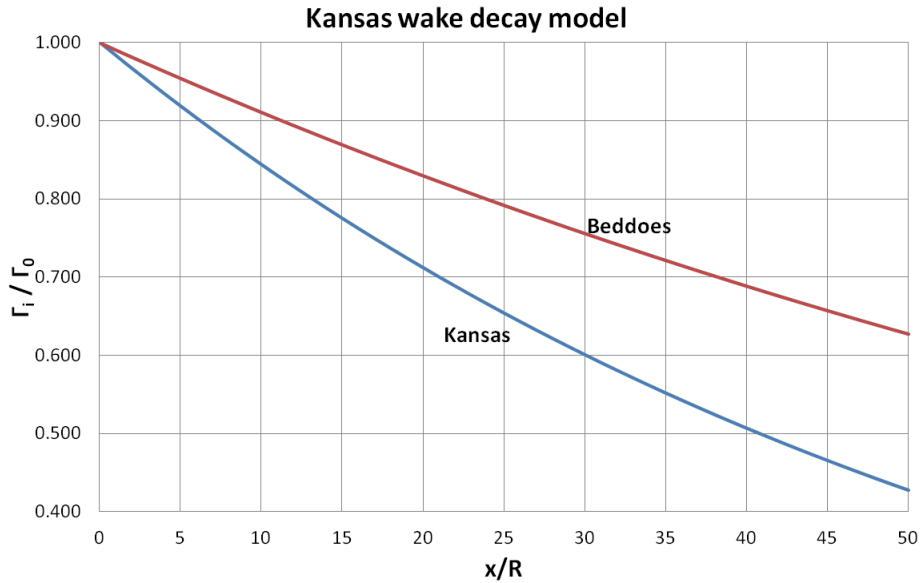


Figure 5.1: Circulation decay curves for the WTN250 wind turbine, wind speed 32.8 ft/s.

In the off-line analysis, the parameters considered include separation distances, diameters of wind turbine, wind speed, angle of encounter, wake vortex circulation, wake decay and wake vortex core size as listed in Table 5.1. This off-line analysis focused on two cases, one is the normal case, in which the Beddoes circulation formula and the 5% blade chord initial wake vortex core size were used; and the other is considered as an extreme case, in which the Kansas circulation formula and the 20% blade chord initial wake vortex core size were used.

Table 5.1: Parameters used in the off-line analysis

Parameters	Used in off-line simulations
Wind turbine diameter (m)	30, 90
Wind speed (m/s)	10, 20
Orientation angles	0° 45°, 90°
Separation	3D, 5D, 10D
Circulation	Beddoes, Kansas
Wake decay	Exponential
Wake vortex core	5 percent chord, 20 percent chord

5.2.1 Wake induced crosswinds of a WTN250 wind turbine

The wake induced velocity fields were obtained based on these parameters. Figures 5.2 and 5.3 show the U, V and W velocity contours in region from 0.5D upstream of the wind turbine to 15D downstream of the wind turbine at a wind speed of 32.8 ft/s (10 m/s). The Beddoes and the Kansas circulation formula were used to obtain the wake vortex circulations. The normal (5% of averaged blade chord) and the enlarged (20% of averaged blade chord) core sizes were applied, respectively.

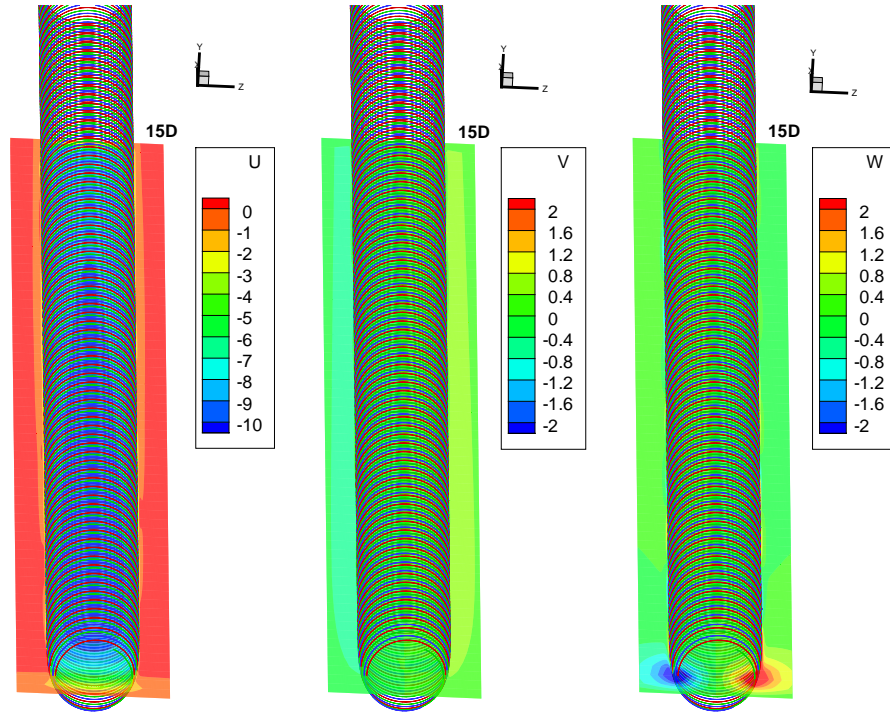


Figure 5.2: Contours of the induced velocities (ft/s) in a region form -0.5D to 15D. Beddoes circulation formula, normal core size (5%), exponential decay, wind speed 32.8 ft/s

The dominant velocity component is the axial velocity U. The V and W velocities are one order of magnitude smaller than the U velocity. In the crossing or oblique encounters, the axial velocity constitute the crosswind, which is one of the criteria that used in Kansas report. For an airport (codes A-I or B-I) that is expected to accommodate single engine aircraft, the maximum crosswind is 12.10 mph (17.75 ft/s) [11]. Figure 5.2 indicates that for the Beddoes circulation formula and the normal core size, which were used in the calculations of the wake velocities for the piloted flight simulations, the maximum induced axial velocity is in the region close to the wind turbine and its value is about 10

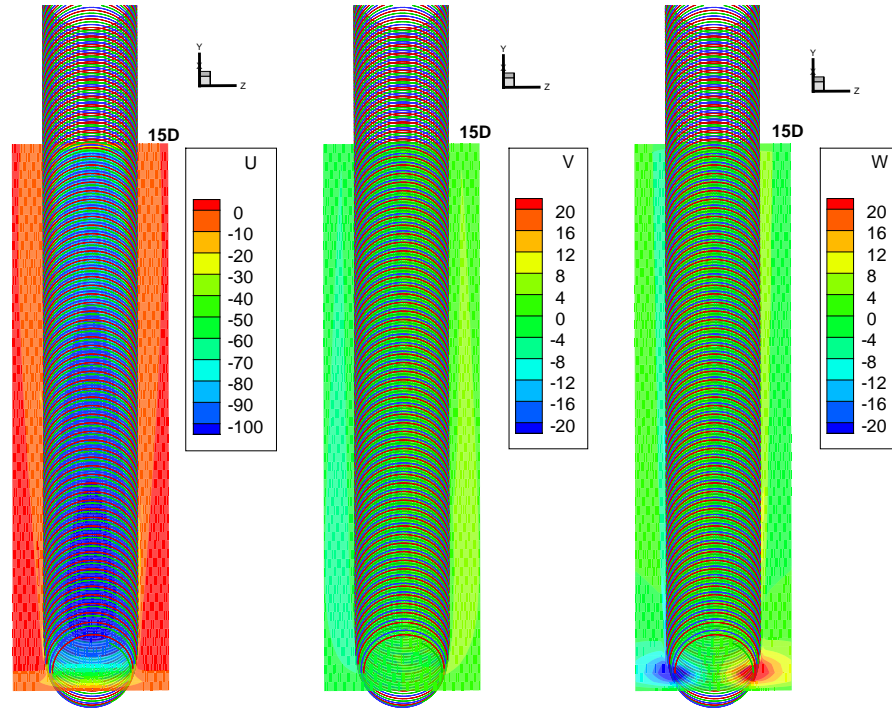


Figure 5.3: Contours of the induced velocities (ft/s) in a region from $-0.5D$ to $15D$. Kansas circulation formula, enlarged core size, exponential decay, wind speed 32.8 ft/s

ft/s. So in this case, the wake is not considered hazardous based on the crosswind criterion. However, for the Kansas circulation and the enlarged core size case (Figure 5.3), the maximum induced axial velocity is up to 100 ft/s, this value is well above the maximum crosswind criterion of 33.73 ft/s for a large air carrier airport (codes D-VI or DV-V) [11].

In the following, results are presented for two modelling approaches. The first model uses the Kocurek wake with the circulation suggested by the Beddoes model and the exponential decay of the circulation. The initial vortex core size was set to 5% of the blade chord. The second model employed the helical wake and following the approach described in the Kansas report [11], the circulation was scaled from the wind tunnel data of [11]. The same decay law was used as for the first model. The vortex core size was larger and take as 20% of the blade chord.

The wake induced crosswind speeds were plotted against the distance from the wind turbine as shown in Figure 5.4. The speeds of the maximum crosswind criteria for the AI and BI and the A-IV through D-VI airports were also plotted on the figure for comparison. The wake induced crosswind speeds calculated using the Beddoes circulation formula are less than the criteria in whole region; while when the Kansas circulation formula were used, the induced crosswind speeds exceeded the crosswind criterion of the A-IV through D-VI airports in the region within $55D$ from the wind turbine. only in the region beyond $82D$, the induced speed fell below the criterion of the AI and BI airports.

For the WTN250 wind turbine at East Midlands airport, the maximum averaged wind speed was 14 m/s (Figure 3.7). Here we also consider a wind speed of 20 m/s as a worst case scenario. At this high wind speed, the WTN250 wind turbine has to be pitch regulated to limit the power output to the rated value of 250 KW. The corresponding thrust was calculated to be 1763 lbf based on momentum theory. The wake vortex circulation is $4.73m^2/s$ according to the Beddoes formula. However, the working state of wind turbine was not considered in the Kansas circulation formula and the circulation is simply proportional to the wind speed. At wind speed of 20 m/s, the Kansas formula produce a circulation of $170.7m^2/s$.

Figures 5.5 and 5.6 show the velocity contours in region from $0.5D$ upstream of the wind turbine to $15D$ downstream of the wind turbine at a wind speed of 65.6 ft/s (20 m/s) for the Beddoes and

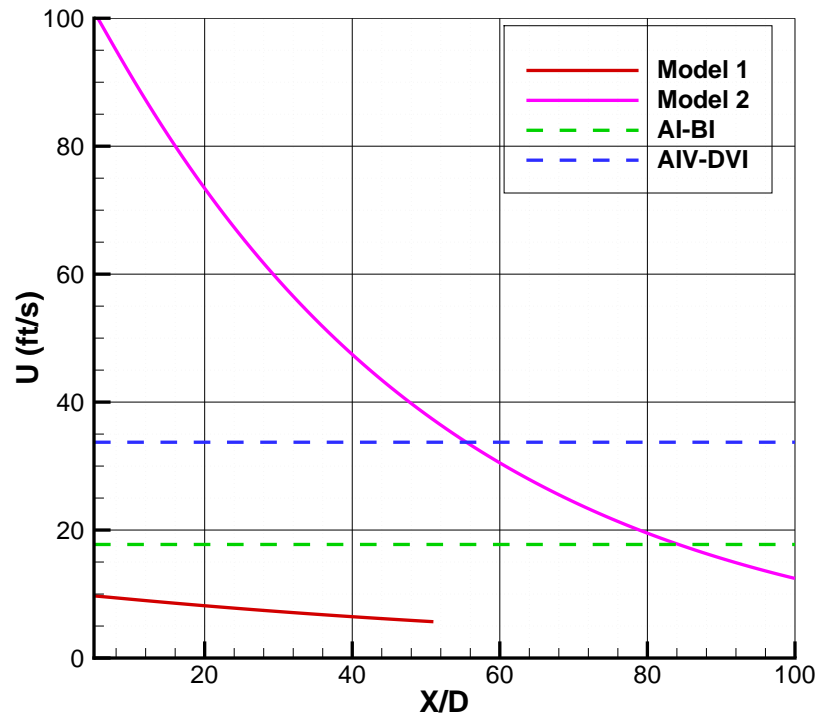


Figure 5.4: Wake induced crosswind speeds with distances, wind speed 32.8 ft/s, Model 1: Beddoes circulation formula with normal core size; Model 2: Kansas circulation formula with enlarged core size.

the Kansas cases.

Figure 5.7 shows the wake induced crosswind at the wind speed of 65.6 ft/s (20 m/s). The results of the Kansas circulation formula indicated that within a distance of 100D, the wake is hazardous as the induced velocity exceeded the crosswind criterion of the AI and BI airports, while the Beddoes formula produced much smaller induced crosswind and in all wake region the induced crosswind speeds are below the crosswind criterion of the AI and BI airports.

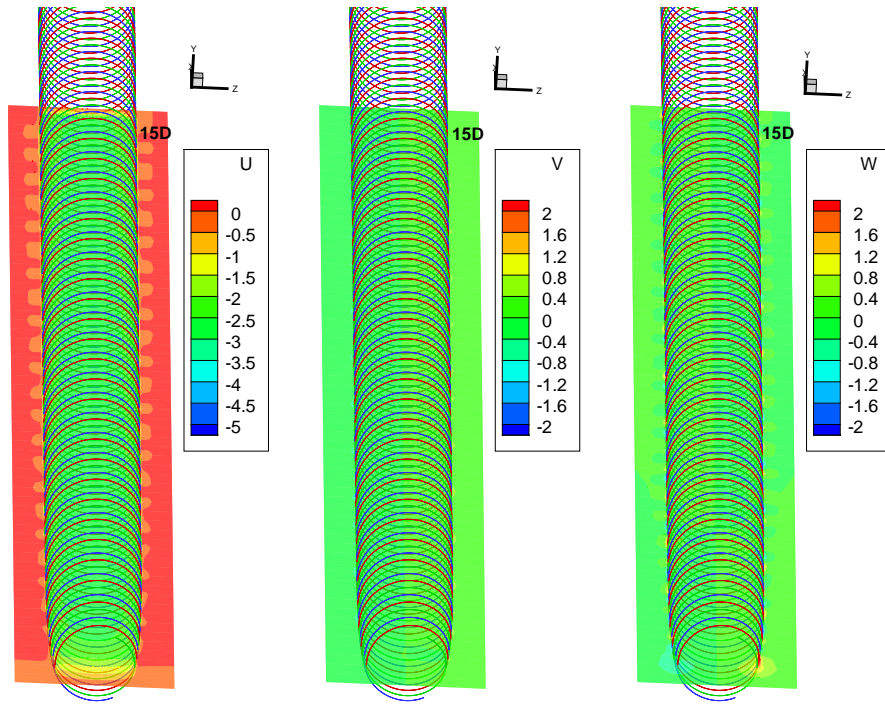


Figure 5.5: Contours of the induced velocities (ft/s) in a region form $-0.5D$ to $15D$. Beddoes circulation formula, normal core size, exponential decay, wind speed 20 m/s.

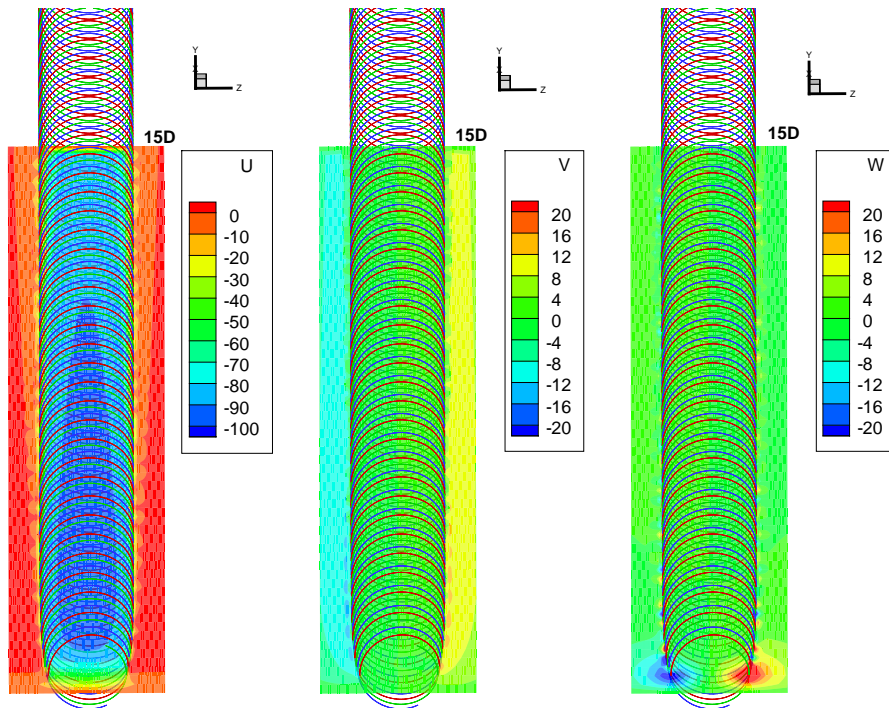


Figure 5.6: Contours of the induced velocities (ft/s) in a region form $-0.5D$ to $15D$. Kansas circulation formula, enlarged core size, exponential decay, wind speed 20 m/s.

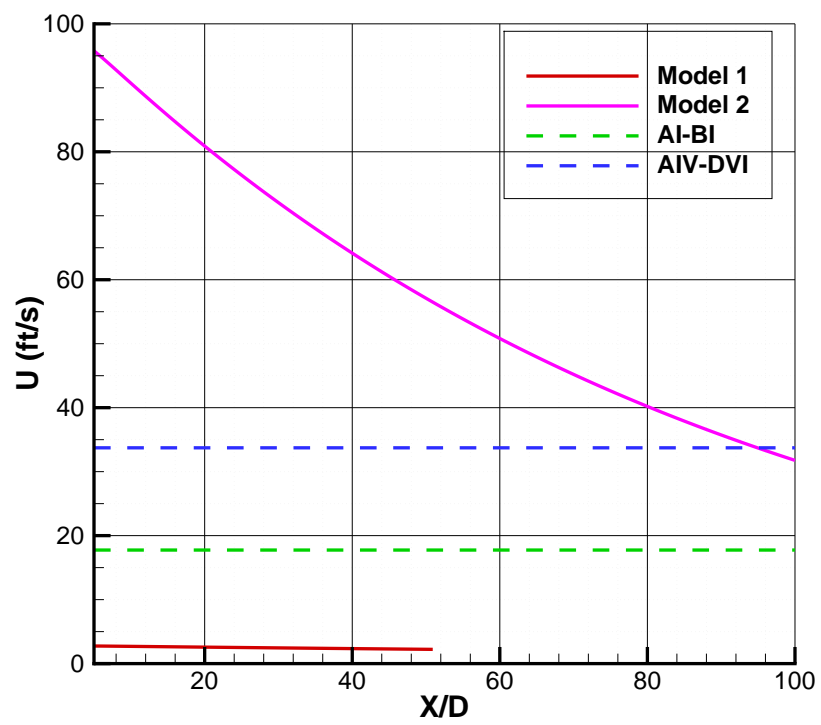


Figure 5.7: Wake induced crosswind speeds with distances, wind speed 65.6 ft/s, Model 1: Beddoes circulation formula with normal core size; Model 2: Kansas circulation formula with enlarged core size..

5.2.2 Variations of forces and moments of the GA during wake encounters

For the GA based on the Grob Tutor configuration, the wing area $S_{wing} = 131.4ft^2$ and the wind span $sp = 32.8ft$. A flight speed $wf = 70kt$ ($118ft/s$) was used in the off-line simulations. The forces and moments were normalised by $0.5\rho wf^2 S_{wing}$ and $0.5\rho wf^2 S_{wing} sp$, respectively, to obtain the force and moment coefficients. The off-line simulation results of crossing encounters are shown in Figures 5.8 and 5.9, where variations of the forces and moments coefficients on the GA as it encountered the wind turbine wake along the runway central line at an offset of 3D were plotted. The large circulation calculated from Kansas formula generated much large variations than that of the circulation calculated from the Beddoes formula. The core size also had some effects on the disturbances generated by the wake.

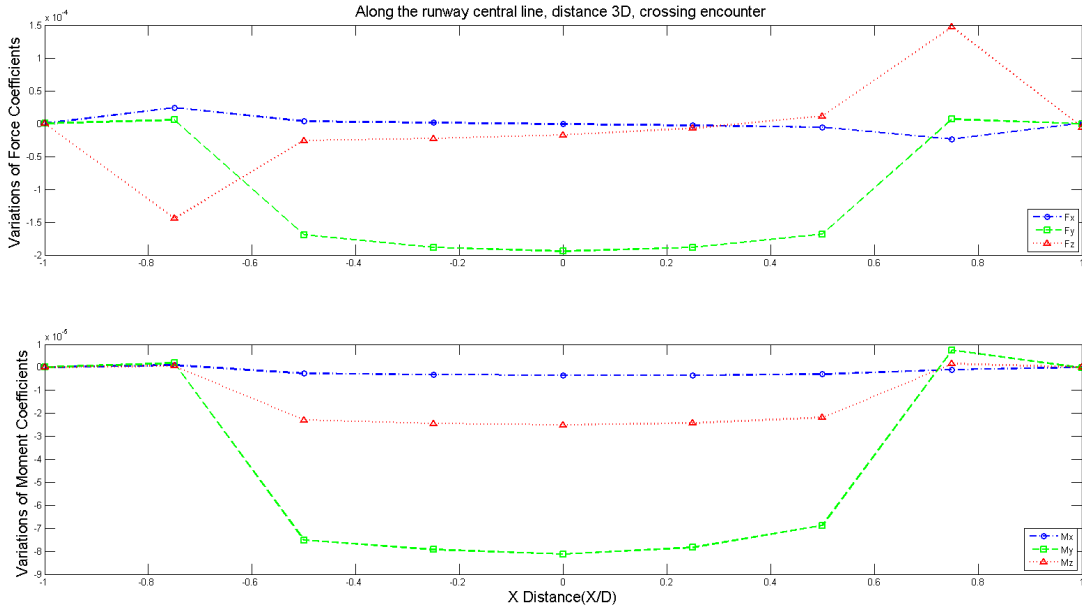


Figure 5.8: Variations of coefficients of forces and moments in off-line crossing wake encounter, GA flew along the runway Central line, offset 3D, Beddoes circulation formula, normal core size, wind speed 32.8 ft/s.

The variations of forces and moments coefficients during wake encounters at the offsets of 5D and 10D are shown in Figures 5.10, 5.11, 5.12 and 5.13.

The off-line simulation results of the 45 deg oblique encounter cases are shown in Figures 5.14 and 5.15 for the 3D offset. Figures 5.16, 5.17, 5.18 and 5.19 show the results for the 5D and 10D offsets.

As in the crossing encounters, similar trends were generally observed in the oblique encounters. The large circulation calculated from Kansas formula generated much large variations than that of the circulation calculated from the Beddoes formula.

A large wind turbine configuration with a 90m diameter was also considered in the off-line simulation. This size is similar to the wind turbine size used in the Kansas report. Again, both the Beddoes and the Kansas circulation formulae and the normal and enlarged core sizes were used to generate the wake induced velocities. Two wind speeds of 10 m/s and 20 m/s were used in the off-line simulations. The wake induced crosswind speeds of this large wind turbine in the wake region are shown in Figure 5.20. The wake induced crosswind speeds calculated using the Beddoes circulation formula (Model 1) are less than the criteria in whole region; while when the Kansas circulation formula (Model 2) were used, the induced crosswind speeds exceeded the crosswind criterion of the A-IV through D-VI airports in the region within 65D for the lower wind speed of 32.8 ft/s and in all region up to 100D for the higher wind speed of 65.6 ft/s.

The variations of coefficients of the forces and moments produced by wake on the aircraft during wake encounter are shown in Figures 5.21 and 5.22. The figures show the similar trends as the

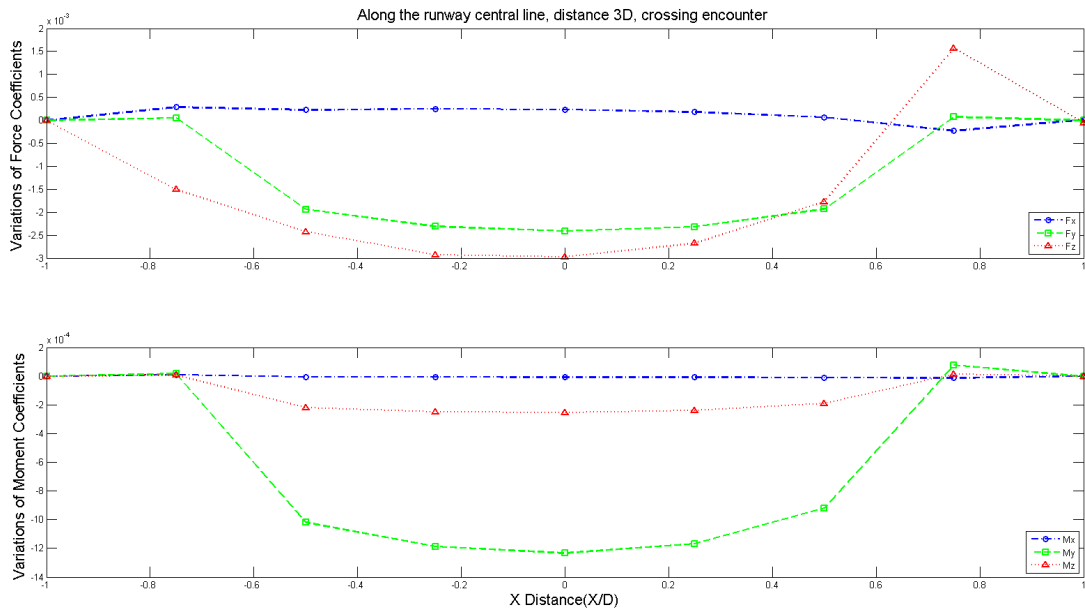


Figure 5.9: Variations of coefficients of forces and moments in off-line crossing wake encounter, GA flew along the runway central line, offset 3D, Kansas circulation formula, enlarged core size, wind speed 32.8 ft/s.

WTN250 wind turbine with a dominant yaw moment disturbance. For the large wind turbine, the magnitudes of the coefficients of the forces and moments are much larger than that of the WTN250 wind turbine.

Regardless the large diameter of the wind turbine, the roll upset calculated in FlightLab was still significantly less than what is reported using the approach described in the Kansas report [11]. We believe that this is due to the approach used by the Kansas researchers that appear to assume a vortex core large enough, comparable in size with the span of the aircraft, and of very high circulation.

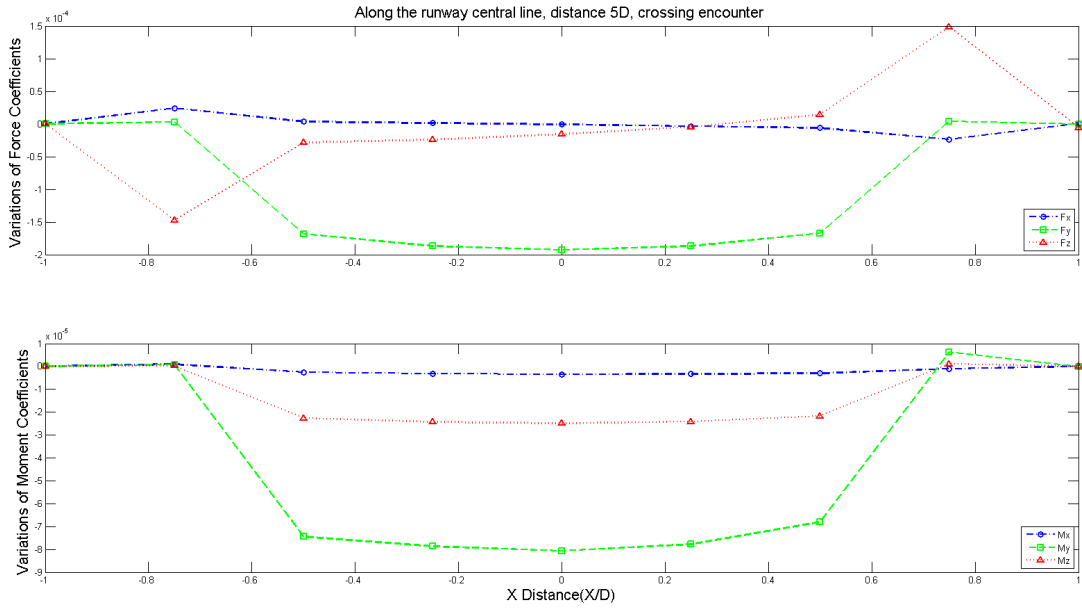


Figure 5.10: Variations of coefficients of forces and moments in off-line crossing wake encounter, GA flew along the runway Central line, offset 5D, Beddoes circulation formula, normal core size, wind speed 32.8 ft/s.

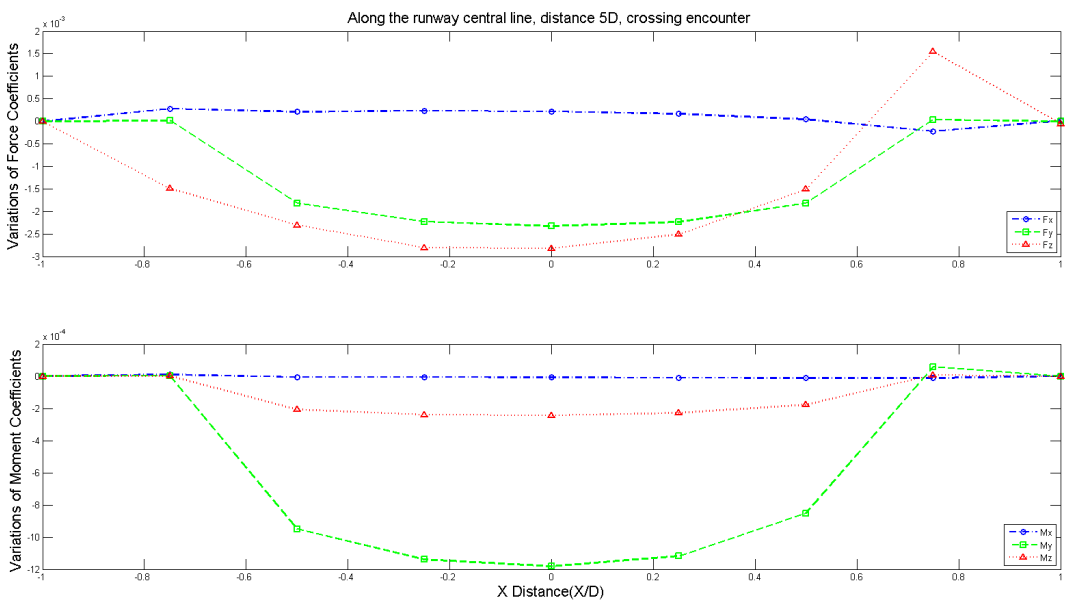


Figure 5.11: Variations of coefficients of forces and moments in off-line crossing wake encounter, GA flew along the runway central line, offset 5D, Kansas circulation formula, enlarged core size, wind speed 32.8 ft/s.

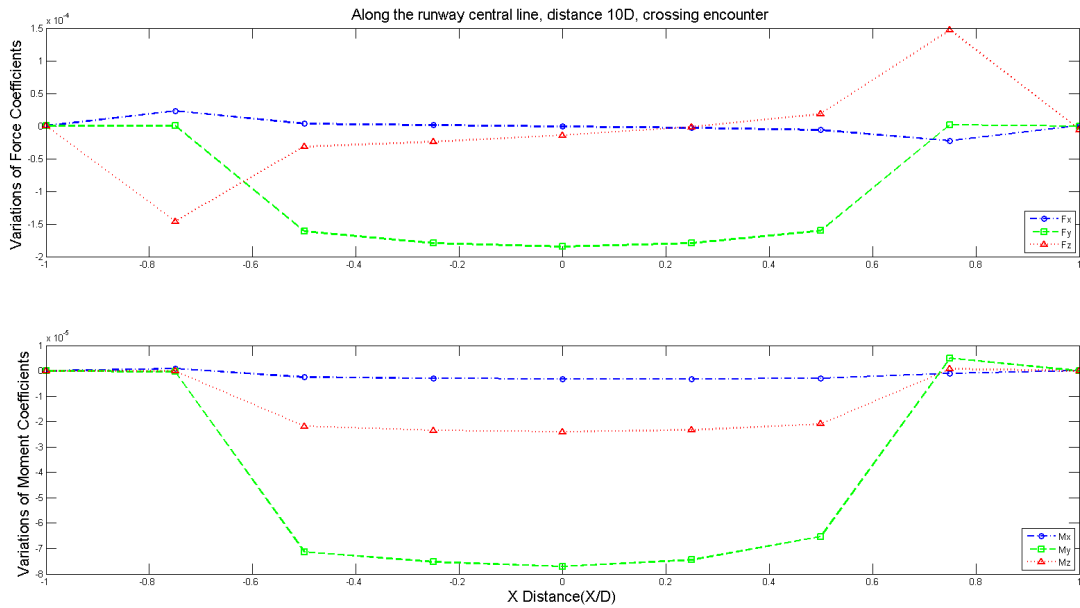


Figure 5.12: Variations of coefficients of forces and moments in off-line crossing wake encounter, GA flew along the runway Central line, offset 10D, Beddoes circulation formula, normal core size, wind speed 32.8 ft/s.

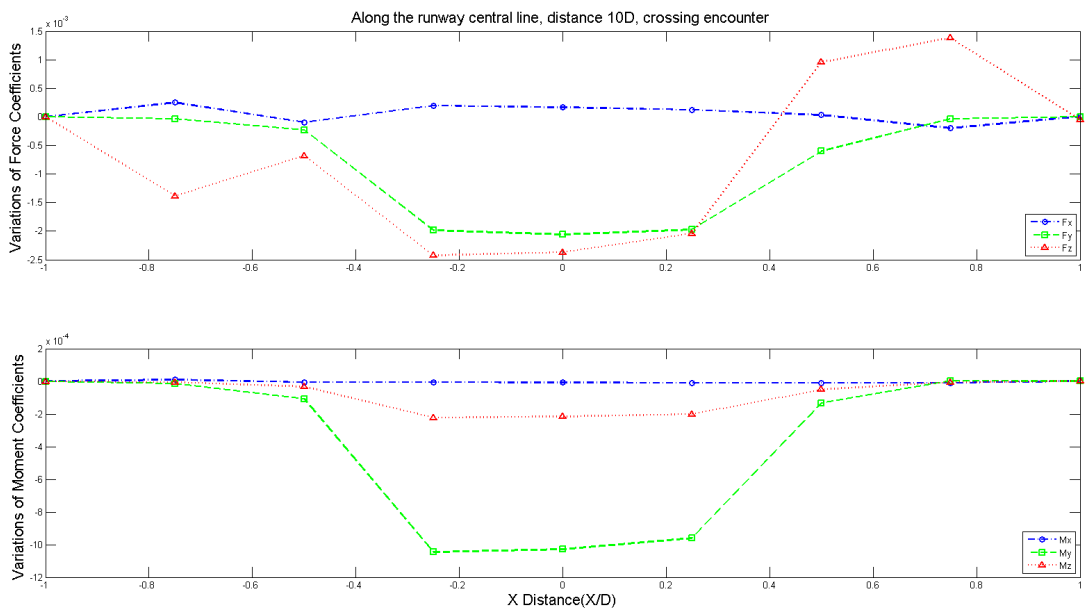


Figure 5.13: Variations of coefficients of forces and moments in off-line crossing wake encounter, GA flew along the runway central line, offset 10D, Kansas circulation formula, enlarged core size, wind speed 32.8 ft/s.

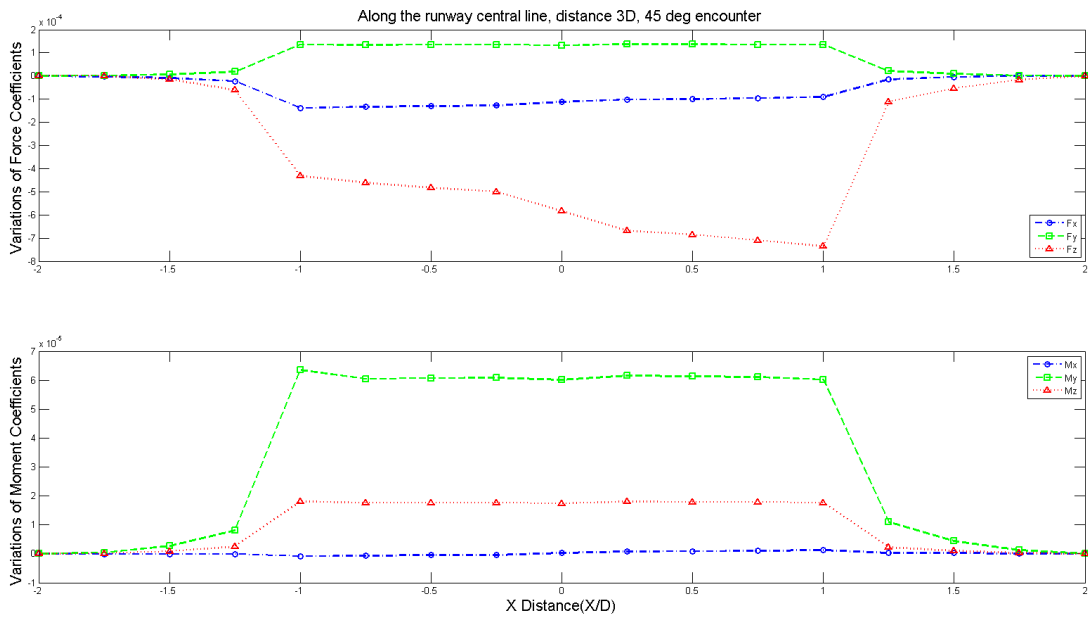


Figure 5.14: Variations of coefficients of forces and moments in off-line crossing wake encounter, GA flew along the runway Central line, offset 3D, 45 deg oblique encounter, Beddoes circulation formula, normal core size, wind speed 32.8 ft/s.

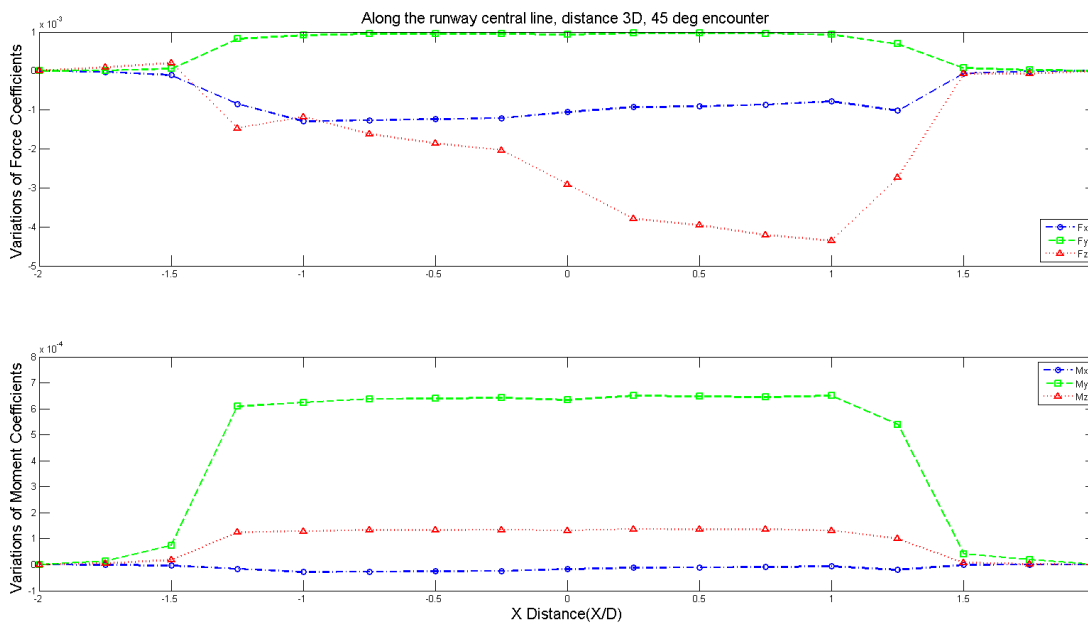


Figure 5.15: Variations of coefficients of forces and moments in off-line crossing wake encounter, GA flew along the runway Central line, offset 3D, 45 deg oblique encounter, Kansas circulation formula, enlarged core size, wind speed 32.8 ft/s.

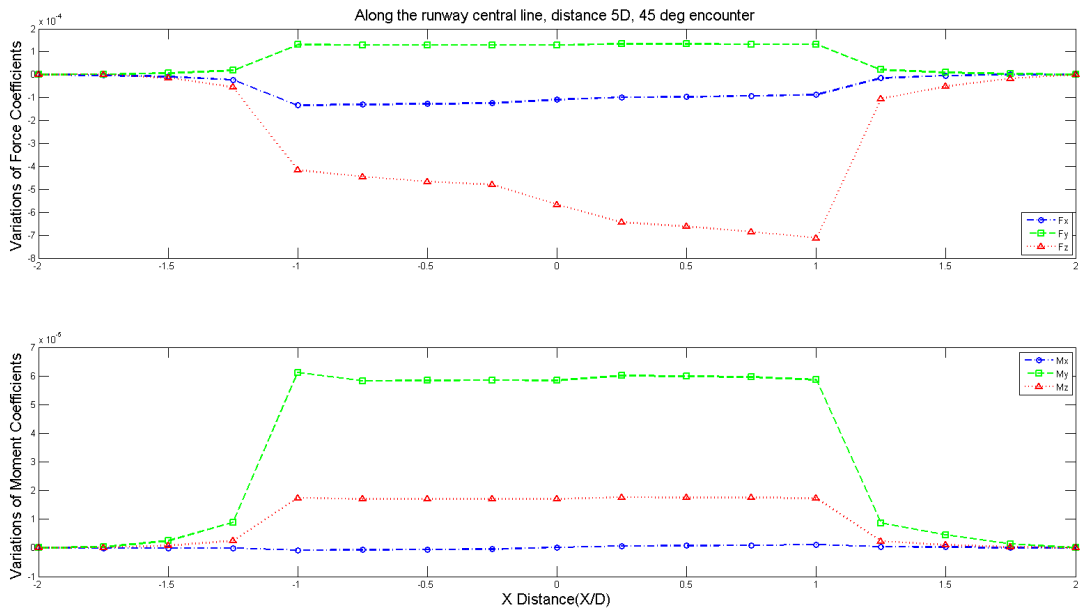


Figure 5.16: Variations of coefficients of forces and moments in off-line crossing wake encounter, GA flew along the runway Central line, offset 5D, 45 deg oblique encounter, Beddoes circulation formula, normal core size, wind speed 32.8 ft/s.

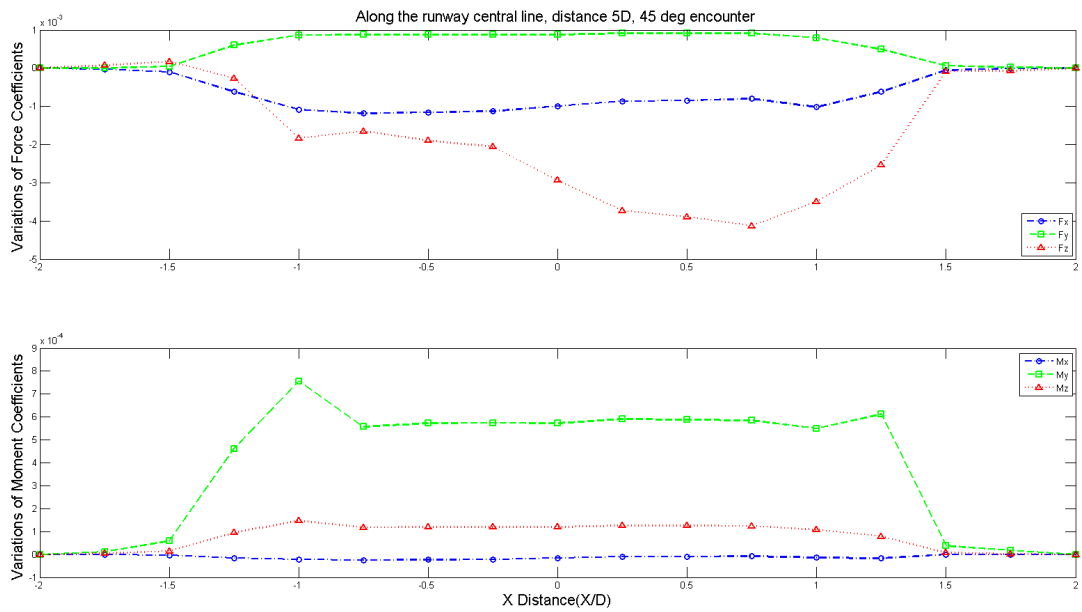


Figure 5.17: Variations of coefficients of forces and moments in off-line crossing wake encounter, GA flew along the runway Central line, offset 5D, 45 deg oblique encounter, Kansas circulation formula, enlarged core size, wind speed 32.8 ft/s.

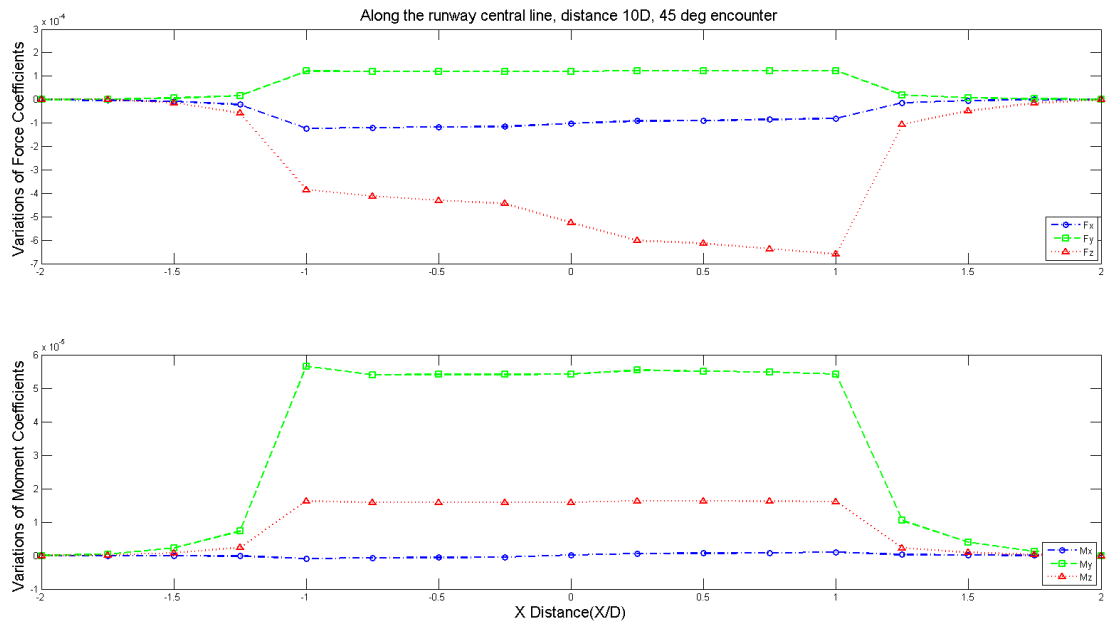


Figure 5.18: Variations of coefficients of forces and moments in off-line crossing wake encounter, GA flew along the runway Central line, offset 10D, 45 deg oblique encounter, Beddoes circulation formula, normal core size, wind speed 32.8 ft/s.

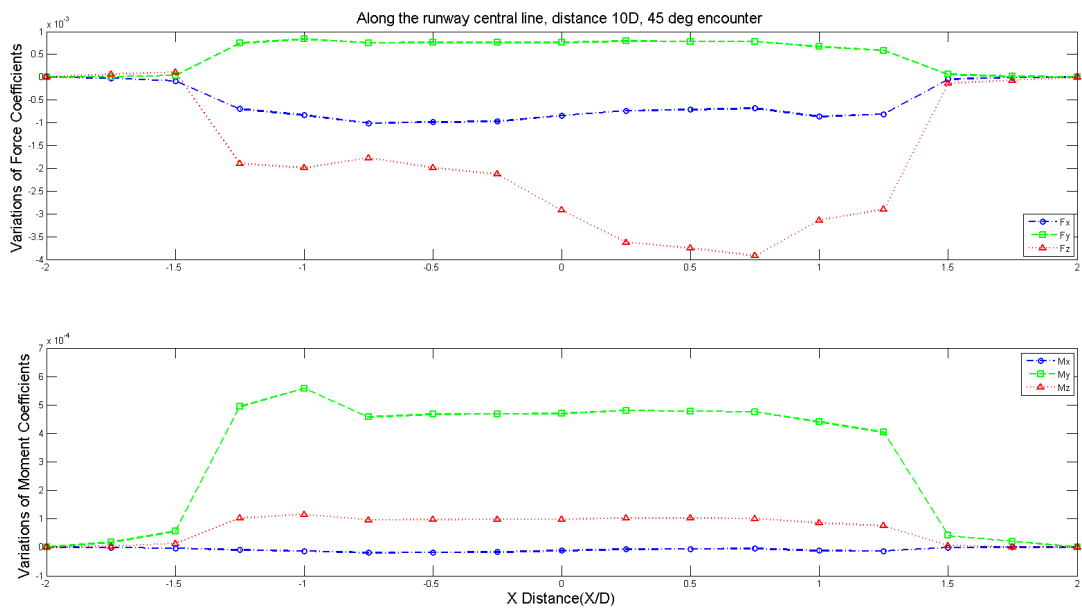


Figure 5.19: Variations of coefficients of forces and moments in off-line crossing wake encounter, GA flew along the runway Central line, offset 10D, 45 deg oblique encounter, Kansas circulation formula, enlarged core size, wind speed 32.8 ft/s.

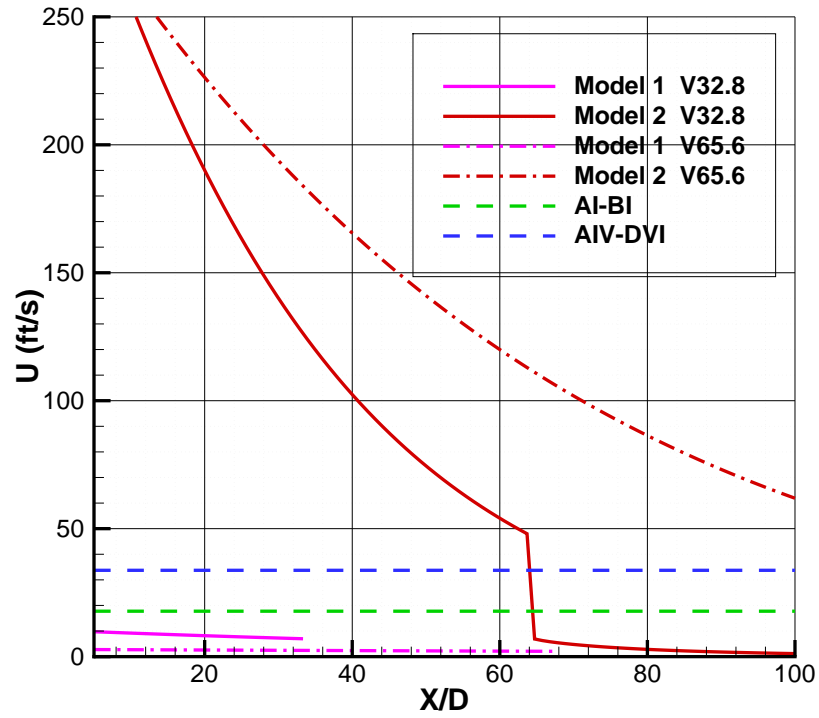


Figure 5.20: Wake induced crosswind speeds against distances, 90 m diameter large wind turbine, wind speed 32.8 ft/s and 65.6 ft/s.

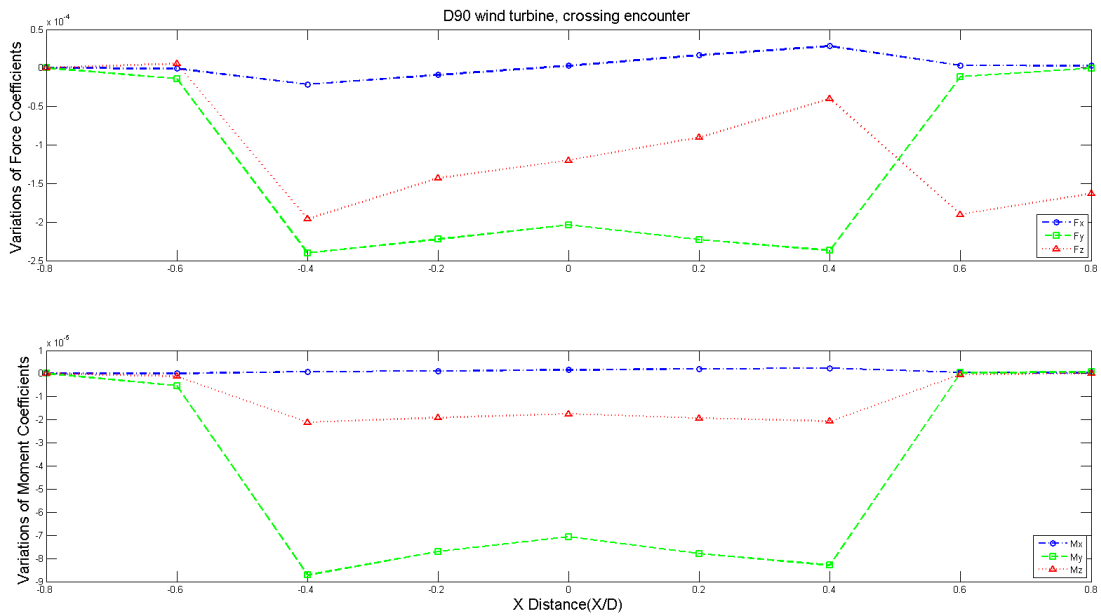


Figure 5.21: Variations of coefficients of forces and moments in off-line crossing wake encounter, GA flew along the runway Central line, offset 3D, Beddoes circulation formula, normal core size, wind speed 32.8 ft/s, large wind turbine.

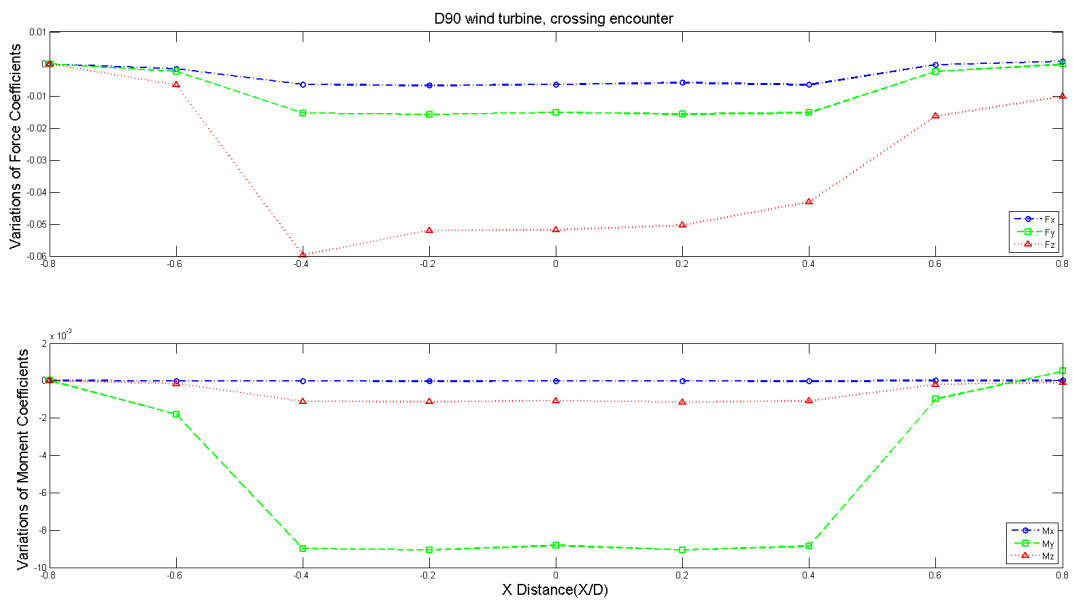


Figure 5.22: Variations of coefficients of forces and moments in off-line crossing wake encounter, GA flew along the runway central line, offset 3D, Kansas circulation formula, enlarged core size, wind speed 32.8 ft/s, large wind turbine.

5.2.3 Analysis of the roll upsets during wake encounters

In the off-line flight simulation, the aircraft might have missed the positions where the induced velocities are large. So the off-line results of the rolling moment coefficient might not account for very localized peak velocities. In this section, an analytical method was adopted to calculate the rolling moment coefficients on the points of a fine grid in the wake field. The wake induced velocity components were extracted in the regions close to the rotor tip, where the induced velocities reach the maximum and minimum values with rapid changes. According to the Kansas report [11], this is the area that the wake caused the largest roll upsets on the encountering aircraft. Because in the Kansas report, the helical vortex core was assumed to be comparable with the aircraft wind span, and when the aircraft was positioned in the helical vortex center and was orientated with the vortex axis, the vortex produced upwash on one side of the wing and downwash on the other side, which resulted maximum induced velocities in the vertical direction and hence generated a large roll moment on the aircraft. The same methodology of calculating the roll moment was adopted and applied to the GA encountering the WTN 250 wind turbine. The wake induced velocity components were obtained using a fine grid with resolution of 1 ft in the regions close to the vortex tip-path. The closer views of the induced velocities are shown in Figure 5.23. The aircraft was perceived flying in an orientation that the three velocity components could be treated as the vertical velocities on the wing. An integration of the induced velocities at the computing points were then carried out to obtain the coefficients of the roll moments at each positions.

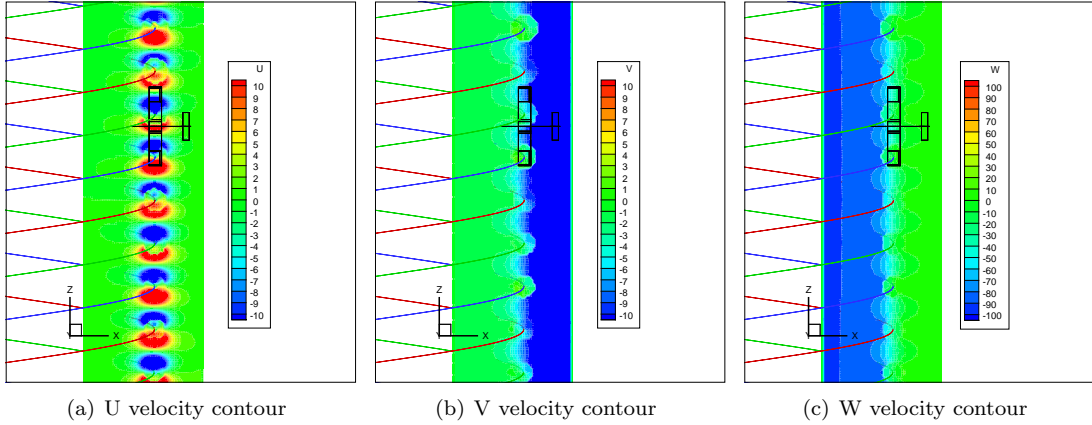


Figure 5.23: Wake induced velocities in the regions close to the rotor blade tip, WTN250 wind turbine, wind speed 32.8 ft/s.

The wake induced rolling moment coefficients on the GA that flies through the wake were calculated for a flight speed of $wf = 70kt$ ($118ft/s$). At each position, the rolling moment coefficients were integrated over 8 points on each side of the wing, which gave a spanwise resolution of 2.05 ft (the span of the GA wing was 32.8 ft). The slope of the lifting coefficient with angle of attack equals to 4.3 /rad, which is the same number as used in the Kansas report [11]. The spanwise changes of the chord length were calculated using the following formula:

$$c_i/c_{avg} = 20/13(1 - 0.7(x_i/b)) \quad (5.5)$$

where i is the computing point, c_{avg} is the average chord length, x_i is the spanwise distance from the wing center and b is the wing span length.

The contours of the wake induced rolling moment coefficients by the velocity component V_y on the GA that flies through the wake are shown in Figure 5.24. The peaks and valleys of the rolling moment coefficients were well captured by using the fine grid. The maximum rolling moment coefficients were approximately 0.002 and 0.02 for the cases with the Beddoes and Kansas circulation formulae, respectively. The criteria of the rolling moment coefficient is 0.28, which was calculated by considering

the maximum rolling moment that the aileron on a normal aircraft can generate at the maximum deflection angle. Even using the Kansas circulation formula, the maximum rolling moment coefficient is still well below the roll criteria.

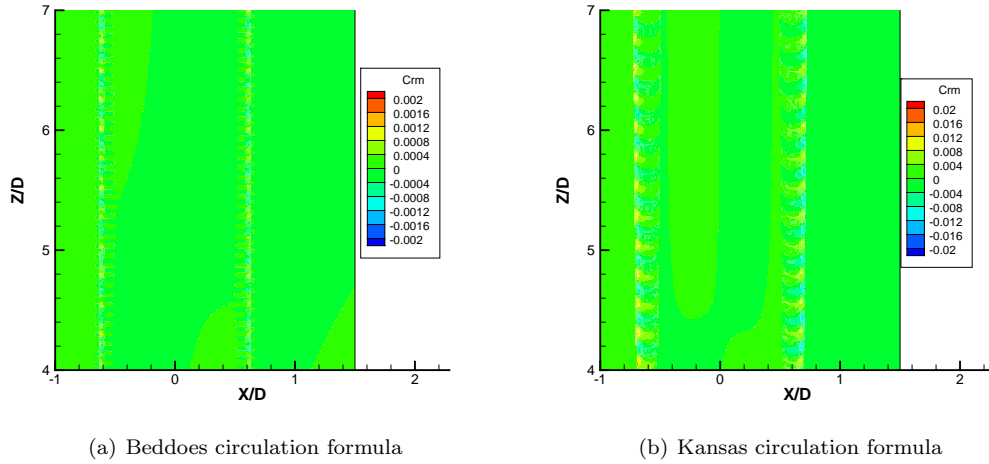


Figure 5.24: Wake induced rolling moment coefficients by V_y , WTN250 wind turbine, wind speed 32.8 ft/s.

For the high wind cases of the 20 m/s wind speed, the wake induced rolling moment coefficients are shown in Figure 5.25. The high wind speed caused the helix stretched further in the axial direction. Combined with the change of the circulation, the wake induced rolling moment coefficients changed. For the case of using Kansas circulation formula, the maximum rolling moment coefficient reached to 0.04. While in the case of using the Beddoes formula, the maximum rolling moment coefficient reduced to 0.001 due to the fact that the thrust was actually reduced at the higher wind speed.

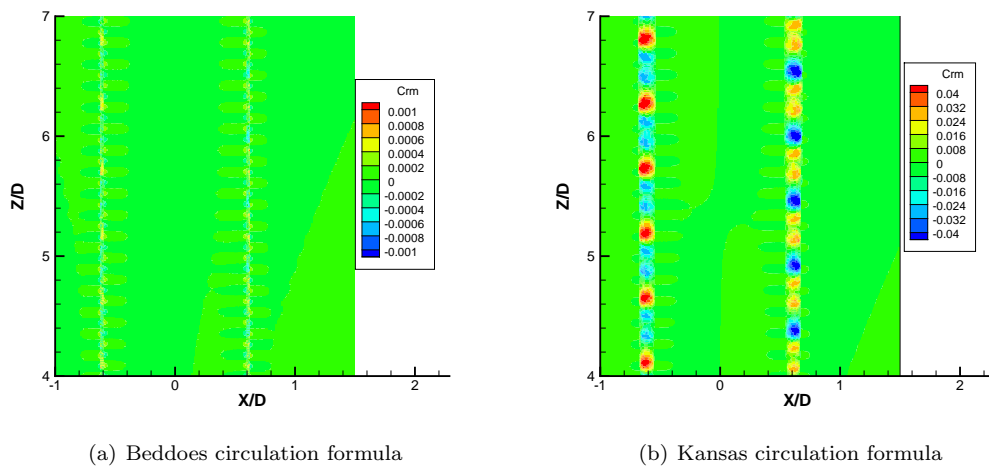


Figure 5.25: Wake induced rolling moment coefficients by V_y , WTN250 wind turbine, wind speed 65.6 ft/s.

The contours of the wake induced rolling moment coefficients by velocity component V_x are shown in Figures 5.26 and 5.27. This is the case that the aircraft flies along the tangent of the helical vortices at the blade tip. If the velocity component V_x is used as the vertical velocity on the wing, the rolling

moment coefficients are almost one order of magnitude larger than that is caused by V_y at the same condition,

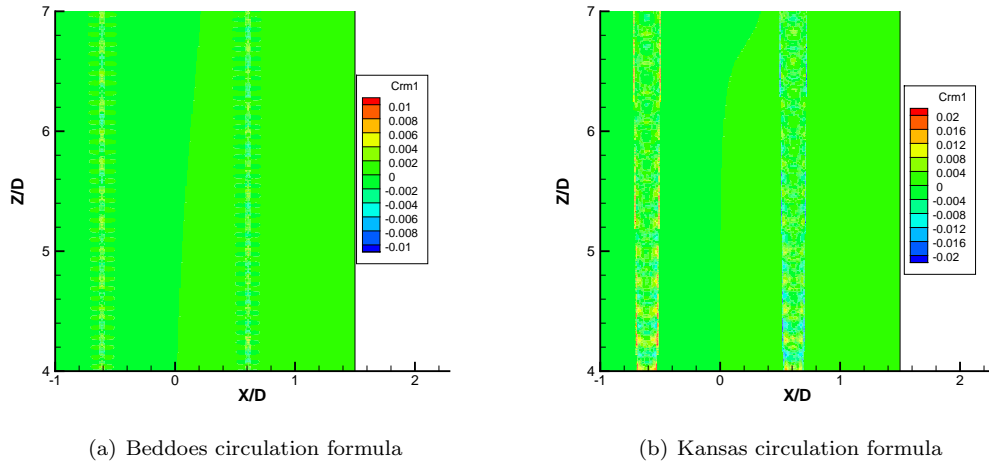


Figure 5.26: Wake induced rolling moment coefficients by V_x , WTN250 wind turbine, wind speed 32.8 ft/s.

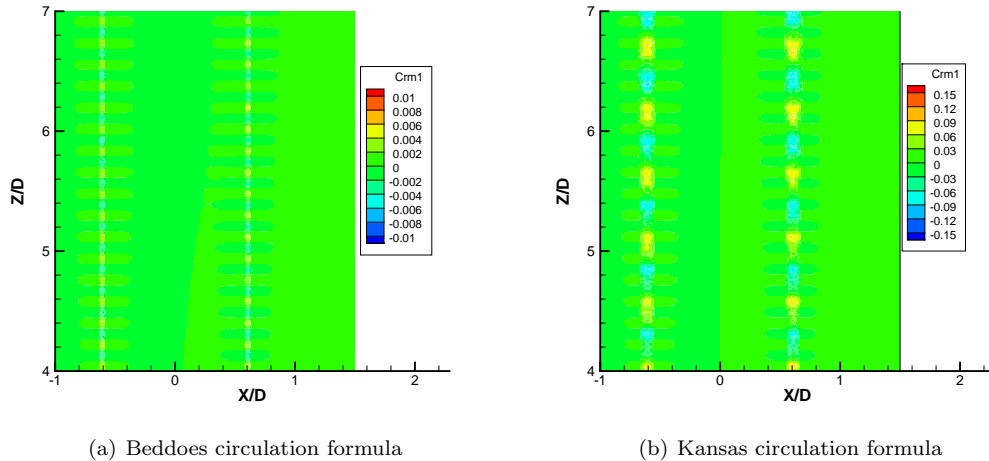


Figure 5.27: Wake induced rolling moment coefficients by V_x , WTN250 wind turbine, wind speed 65.6 ft/s.

A sensitive study of the number of computing points of the integration of the rolling moment coefficient was also carried out using 8, 16 and 32 spanwise points on the wing. Figure 5.28 shows the comparison of the rolling moment coefficients calculated using these different numbers of computing points. The results indicate that the integration of 16 points produced similar contour as that of the 32 points. So the 16 points integration of the rolling moment coefficient is sufficient for the off-line roll upsets study.

The contours of the wake induced rolling moment coefficients of a large wind turbine with 90m diameter are shown in Figure 5.29. A high wind speed of 20 m/s, the Kansas circulation formula and the enlarged core size were used in the calculations of the wake induced rolling moment coefficients. This was considered to be the worst case scenario. The maximum wake induced rolling moment coefficient reached 0.1.

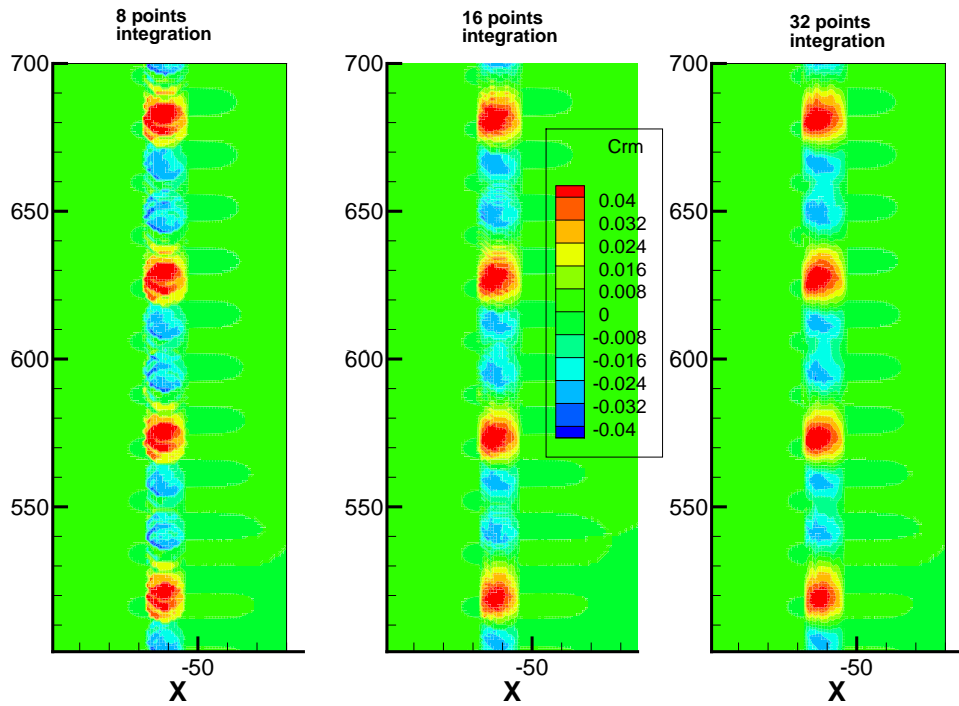


Figure 5.28: Wake induced rolling moment coefficients calculated from different numbers of spanwise computing points, WTN250 wind turbine, wind speed 65.6 ft/s.

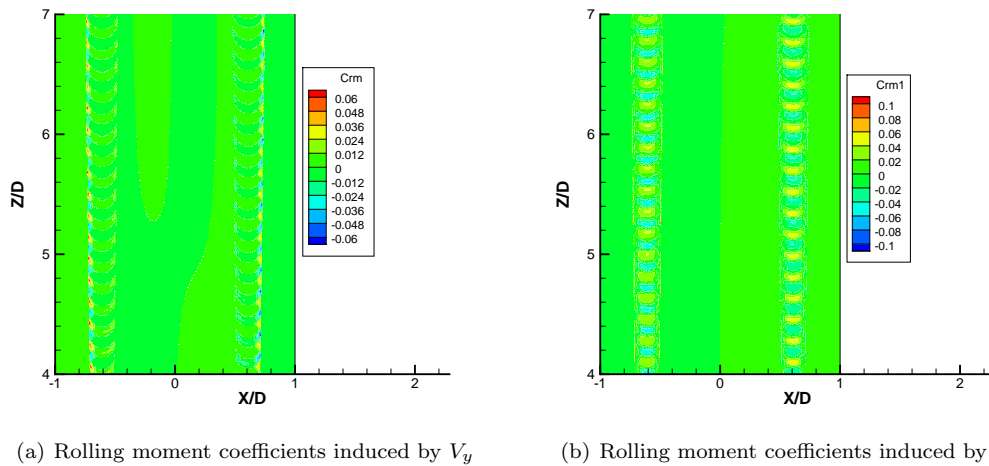


Figure 5.29: Wake induced rolling moment coefficients, large wind turbine with a 90m diameter, wind speed 65.6 ft/s.

5.3 Discussion of off-line simulation results

For a wind turbine with size similar to the WTN250, and using the Beddoes circulation formula, the off-line simulation results indicate that the wind turbine wake did not pose any hazards to the encountering aircraft 5 diameters further from the wind turbine. The dominant upset that the wake generated is a yawing moment on the aircraft. The wake generated crosswind, is smaller than the maximum crosswind of 17.75 ft/s for an airport (codes A-I or B-I) that is expected to accommodate single engine aircraft. These conclusions are in line with that found in the piloted flight simulation.

However, using the Kansas circulation formula, the dominant upset that the wake generated is still a yaw moment on the aircraft. But the wake generated crosswind was found to be above the crosswind criterion of 17.75 ft/s. According to the exponential decay law, the wake induced crosswinds reduced to a level below the criterion only in the region after 82D downwind at 10 m/s wind speed. For a high wind speed of 20 m/s, the wakes in the region up to 100D downstream of the wind turbine were found to be hazardous as the induced crosswind speeds were larger than the crosswind criterion of the AI and BI airports.

In these off-line simulated wake encounters, the size of vortex core generated by the wake model is much smaller than the aircraft span (even in the enlarged core size cases). The aircraft wing covered several helices when it penetrated the wind turbine wake coherent vortices. The dominant upset of the wind turbine wake on the aircraft was the yaw moment during the crossing and oblique encounters. The other overall forces and moments generated by the wind turbine wakes were relatively smaller. The off-line simulations indicated that the rolling moments were small for the WTN250 wind turbine wake. The roll hazards produced in the wake encounters were not significant even in the cases that the Kansas circulation formula and the enlarged vortex core size were used. This is completely different with the analysis in the Kansas report, where a single helix with a core size compatible to the aircraft wing span was assumed. The highest rolling moment occurred when the aircraft was at the center of the helical vortex core. Although the approach taken in the Kansas report appears to be extreme, it certainly shows the variability of the predictions based on the employed models.

For wind turbines smaller than the WTN250 for which LIDAR measurements are available, the approach based on the Beddoes circulation formula appears to give predictions in line with the measurements.

Chapter 6

Conclusions and Future Work

Different wind turbine wake models, namely the Kocurek wind turbine wake vortex model, far-wake velocity deficit models, and full CFD method have been used. The Kocurek wake model has been validated with wind tunnel experimental measurements on the MEXICO wind turbine. The wake induced velocities have also been compared with the full CFD results. These comparisons indicated that the Kocurek model predicted wind turbine wake with a reasonable accuracy.

The Kocurek wind turbine vortex model was then applied to a WTN250 wind turbine, which is installed at the East Midlands Airport, UK, where wind turbine wake field measurements using LIDAR were also carried out. The LIDAR measurements captured the wake flow patterns in terms of wake induced mean velocity deficit. The statistical LIDAR data indicated that for this particular wind turbine the wake mean velocities recovered to the free stream speed at a position about five rotor diameters downstream. The LIDAR measurements were compared with the results of a full CFD simulation conducted for the MEXICO wind turbine with a similar tip speed ratio, and also compared with the velocity deficit wake models. In general, reasonable agreement was found.

The WTN250 wake induced velocity fields generated by the Kocurek wake vortex model, were integrated into an aircraft flight dynamics model based on a GA configuration to simulate the wind turbine wake encounter scenario of a light aircraft approaching an airport. Piloted flight simulations were carried out to study the severity of this type of wake encounter. The flight simulation results suggest that the WTN250 wind turbine wake mainly generated yaw disturbances on the encountering aircraft and caused a yaw angle deviation less than 10 deg. The wake encounter severity is regarded as minor according to the wake vortex severity rating scale.

The current results show that for the small-size WTN250 wind turbine the wake is not strong to cause any significant upset to the aircraft at distances of 5 wind turbine diameters and longer. However, the validation of the models, currently, allows for no extrapolation to larger wind turbines.

It is recognised that both the Kocurek wake model and the current LIDAR measurements only show the wake velocity deficit flow fields. The mean velocity deficit in wind turbine wake normally decays faster than wake turbulence, and the wake turbulence might be persistent longer downstream the wind turbine. If the length scales of the wake turbulence are comparable with the size of aircraft lifting surfaces, it could cause unsteady upsets on the encountering aircraft. So methods of modelling and measuring wind turbine wake turbulence will be sought and be implemented in the future wake encounter flight simulations. A helicopter model was developed to simulate the wind turbine wake encounter in the same fashion. The responses of the helicopter and the pilots' controls are anticipated to be different due to the different flight dynamics.

The current LIDAR wake measurements only resolve the velocity along the line of the laser beam, A truly 3-D velocity vector at a spatial point needs 3 measurements at different laser beam angles. Flow turbulence measurements also need the LIDAR scan to be carried out simultaneously with small interval to resolve the small scale of wake vortices. These requirements pose a challenge to the LIDAR technology. A nacelle mounted LIDAR system is ideal to achieve wake measurements for all-wind directions. These future high quality LIDAR data will be used to validate different wind turbine wake models as the off-line analysis shows the variability of the predictions based on the employed models.

Further simulation trials are needed with unsteady wake models, like the CFD, freewake or at least synthetic eddy models. Due to the sensitivity of the models on the core size and circulation, their evolution and decay, detailed CFD studies should be conducted and compared with the new LIDAR measurements.

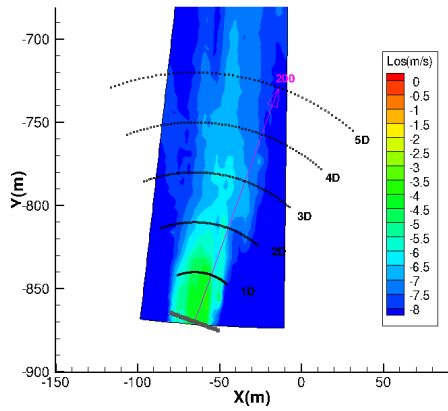
Bibliography

- [1] A. Becnmann, N.N. Sorensen, and F. Zahle. CFD simulations of the MEXICO rotor. *Wind Energy*, 14(5):677–689, 2011.
- [2] T.S. Beddoes. A Wake Model for High Resolution Airloads. *U.S. Army/AHS Conference on Rotorcraft Basic Research*, February 1985.
- [3] CAA. CAA Policy and Guidelines on Wind Turbines. Technical report, Civil Aviation Authority, January 2012.
- [4] M. Carrion, R. Steijl, M. Woodgate, and G. Barakos. CFD Analysis of the Wake of the MEXICO Wind Turbine. *Wind Energy*, 00:1–17, 2012.
- [5] M. Carrion, M. Woodgate, R. Steijl, G. Barakos, S. Gomez-Iradi, and X. Munduate. Understanding Wind Turbine Wake Breakdown Using CFD. *Journal of AIAA*, Accepted, 2014.
- [6] J. W. Castles and R.B. Gray. Empirical relation between induced velocity, thrust and rate of descent of a helicopter rotor as determined by wind-tunnel tests on four model rotors. Technical Report NACA TN 2474, NASA, 19651.
- [7] I. Katic, J. Jojstrup, and N.O. Jensen. A Simple Model for Cluster Efficiency. *Proc. EWEC*, 1:407–410, 1986.
- [8] D. Kocurek. Lifting Surface Performance Analysis for Horizontal Axis Wind Turbines. Technical Report SERI/STR-217-3163, Solar energy research institute, US department of energy, 1987.
- [9] J.D. Kocurek and J.L. Tangler. A Prescribed Wake Lifting Surface Hover Performance Analysis. *Journal of the American Helicopter Society*, 22(1):24–35, January 1977.
- [10] G. Leishman. *Principles of Helicopter Aerodynamics*. Cambridge aerospace series book, Cambridge, UK, second edition, 2007.
- [11] T.E. Mulinazzi and Z.C. Zheng. Wind Farm Turbulence Impacts on General Aviation Airports in Kansas. Technical Report K-TRAN KU-13-6, Kansas State University, January 2014.
- [12] G.D. Padfield, B. Manimala, and G.P. Turner. A Severity Analysis for Rotorcraft Encounters with Vortex Wakes. *Journal of American Helicopter Society*, 49(4):445–456, 2004.
- [13] G.D. Padfield and M.D. White. Flight simulation in academia - heliflight in its first year of operation at the university of liverpool. *The Aeronautical Journal*, 107(1075):529–538, 2003.
- [14] B. Sanderse. Aerodynamics of Wind Turbine Wakes. Technical Report ECN-E-09-016, Energy research centre of the Netherlands, 2000.
- [15] H. Snel, J.G. Schepers, and B. Montgomerie. The MEXICO project: the database and first results of data processing and interpretation. *Journal of Physics: Conference Series*, 75(012014), 2007.
- [16] N. Troldborg, J.N. Sorensen, and R. Mikkelsen. Numerical Simulations of Wake Characteristics of a Wind Turbine in Uniform Inflow. *Wind Energy*, 13:86–99, 2010.

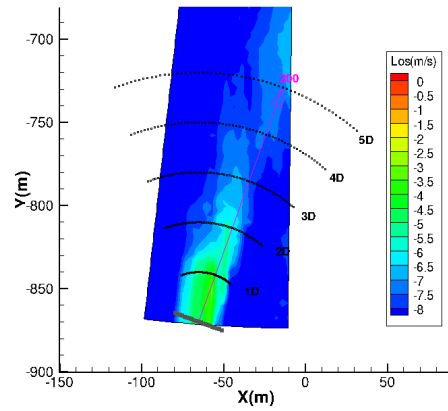
- [17] L. Vermeer, J. Sorensen, and A. Crespo. Wind Turbine Wake Aerodynamics. *Progress in Aerospace Sciences*, 39:467–510, 2003.

Chapter 7

Appendix: WTN250 Wake LIDAR Measurements

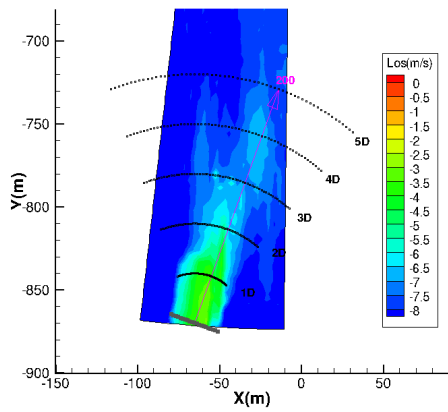


(a) Ten minutes average of 13:00 -13:10

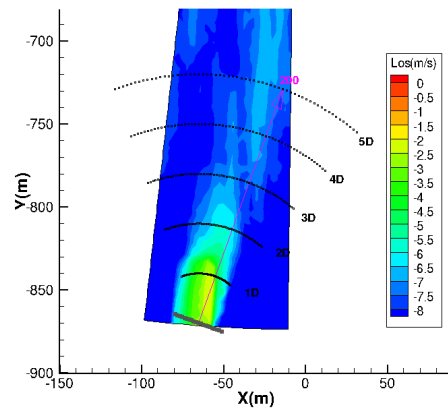


(b) Ten minutes average of 13:10 -13:20

Figure 7.1: Ten-minutes averaged line of sight velocity measured on 07-04-2014.

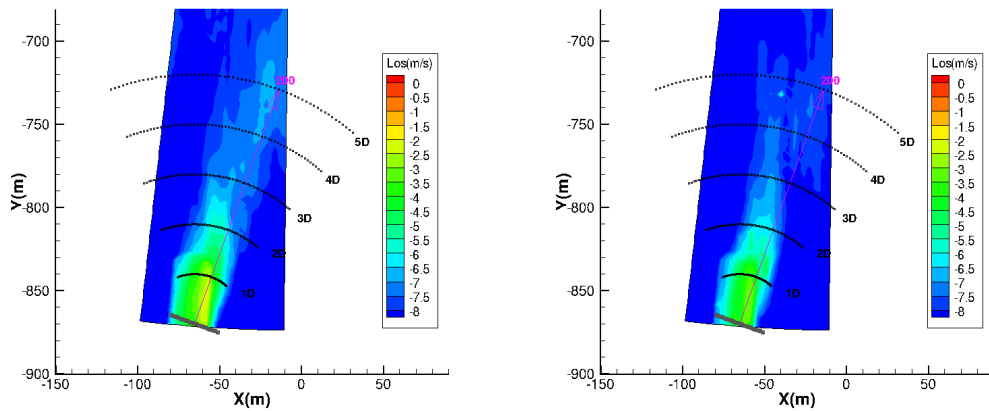


(a) Ten minutes average of 13:20 -13:30



(b) Ten minutes average of 13:30 -13:40

Figure 7.2: Ten-minutes averaged line of sight velocity measured on 07-04-2014.



(a) Ten minutes average of 13:40 -13:50

(b) Ten minutes average of 13:50 -13:60

Figure 7.3: Ten-minutes averaged line of sight velocity measured on 07-04-2014.

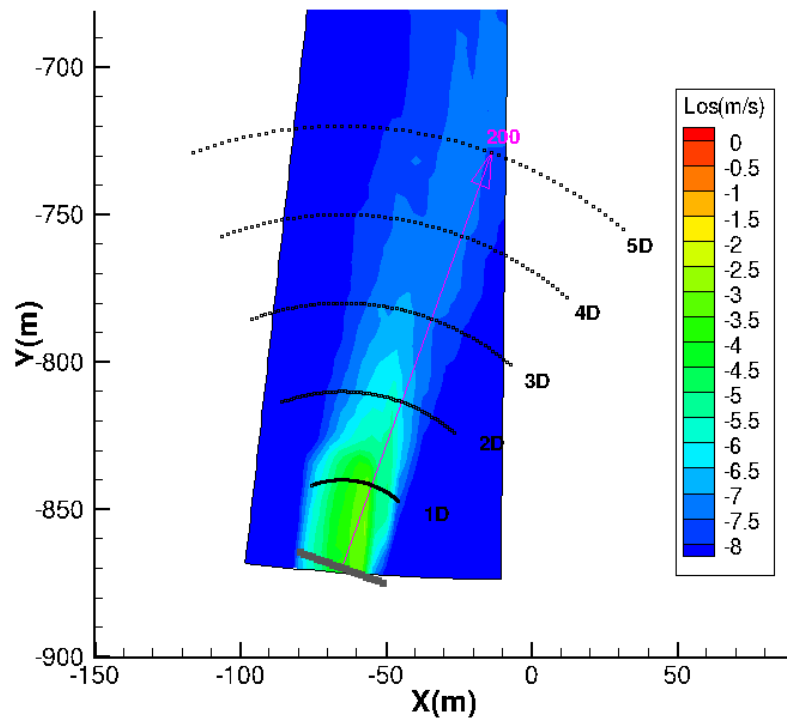
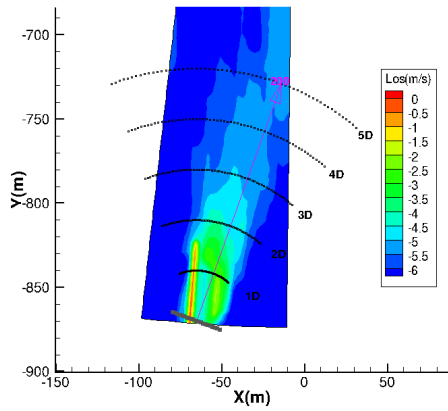
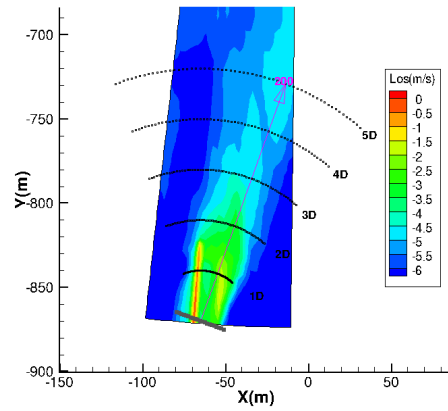


Figure 7.4: One-hour (13-14) averaged Line of sight velocity measured on 07-04-2014.

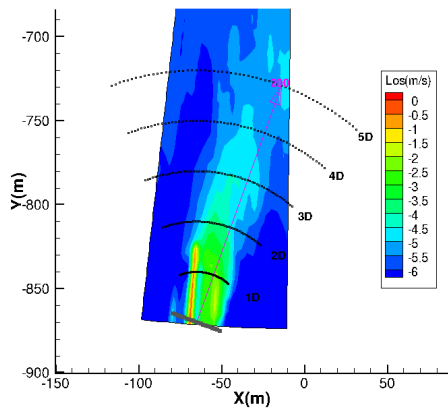


(a) Ten minutes average of 05:00 -05:10

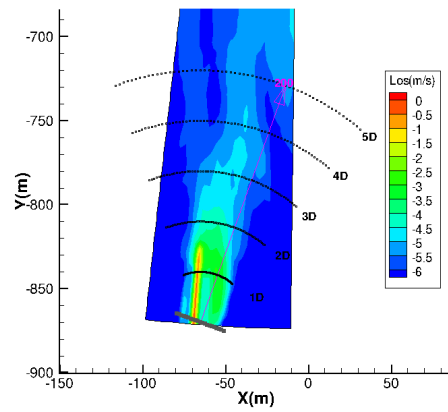


(b) Ten minutes average of 05:10 -05:20

Figure 7.5: Ten-minutes averaged line of sight velocity measured on 06-04-2014.

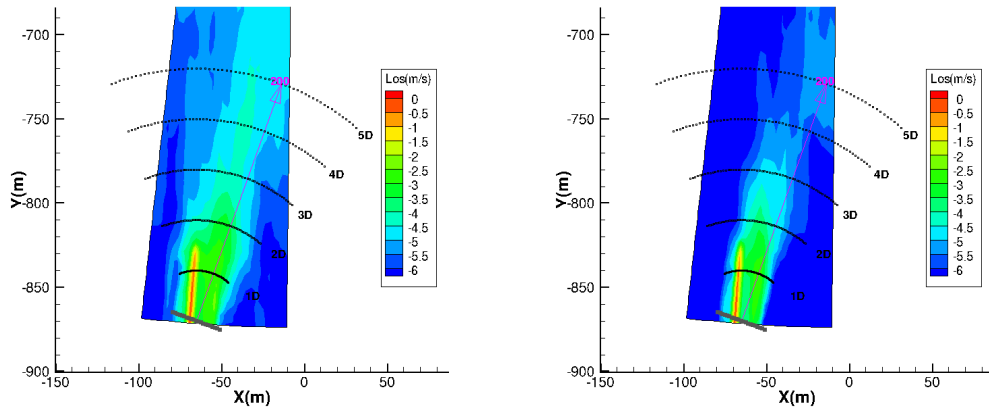


(a) Ten minutes average of 05:20 -05:30



(b) Ten minutes average of 05:30 -05:40

Figure 7.6: Ten-minutes averaged line of sight velocity measured on 06-04-2014.



(a) Ten minutes average of 05:40 -05:50

(b) Ten minutes average of 05:50 -05:60

Figure 7.7: Ten-minutes averaged line of sight velocity measured on 06-04-2014.

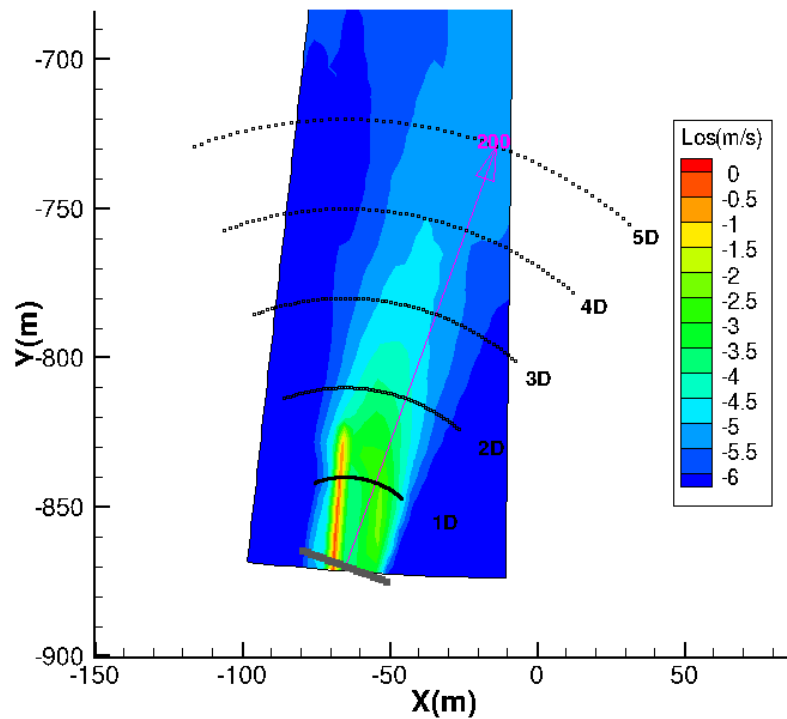
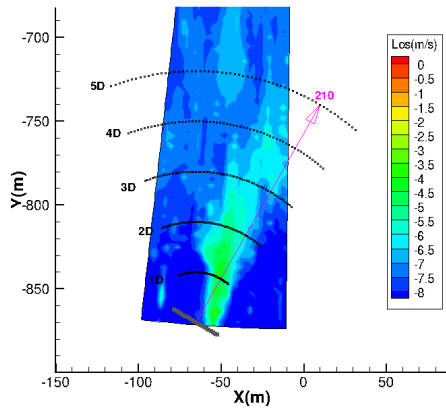
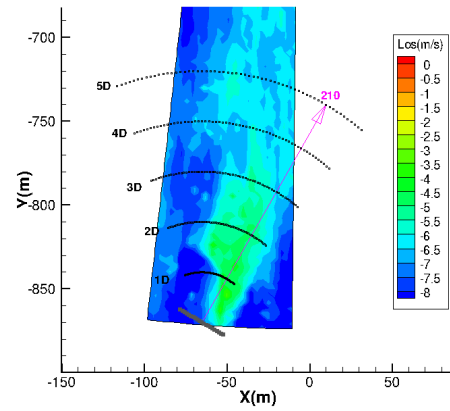


Figure 7.8: One-hour (05-06) averaged Line of sight velocity measured on 06-04-2014.

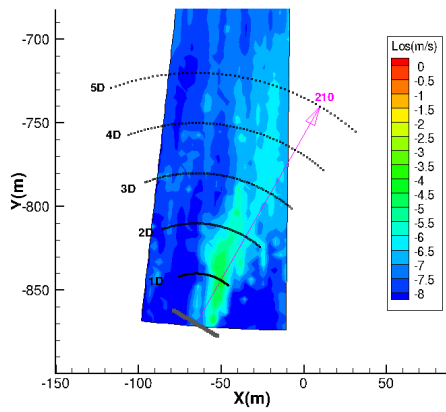


(a) Ten minutes average of 15:00 -15:10

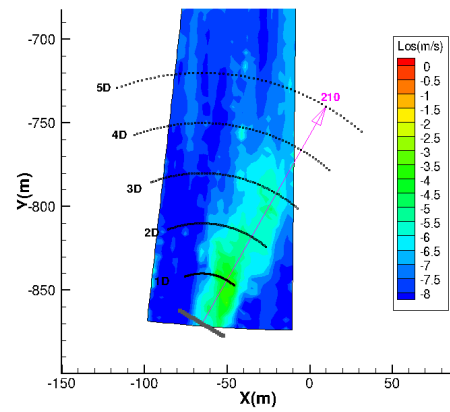


(b) Ten minutes average of 15:10 -15:20

Figure 7.9: Ten-minutes averaged line of sight velocity measured on 06-04-2014.

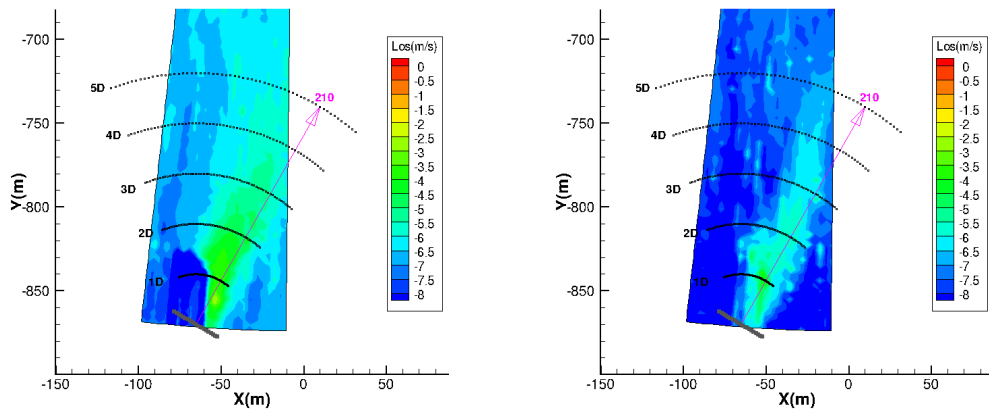


(a) Ten minutes average of 15:20 -15:30



(b) Ten minutes average of 15:30 -15:40

Figure 7.10: Ten-minutes averaged line of sight velocity measured on 06-04-2014.



(a) Ten minutes average of 15:40 -15:50

(b) Ten minutes average of 15:50 -15:60

Figure 7.11: Ten-minutes averaged line of sight velocity measured on 06-04-2014.

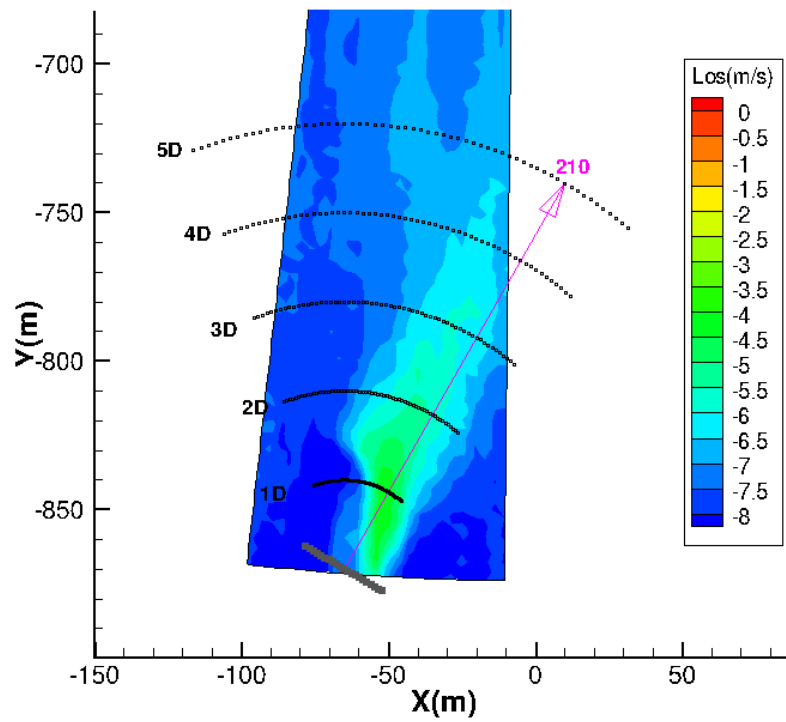
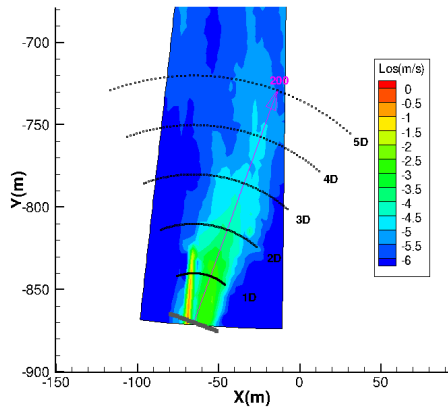
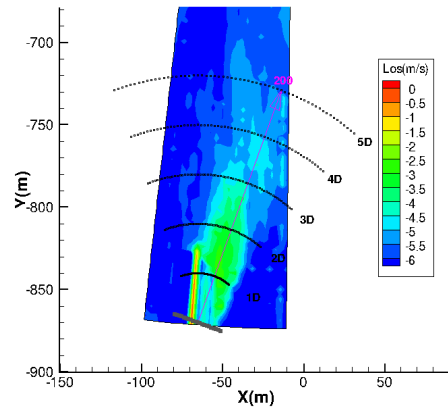


Figure 7.12: One-hour (15-16) averaged Line of sight velocity measured on 06-04-2014.

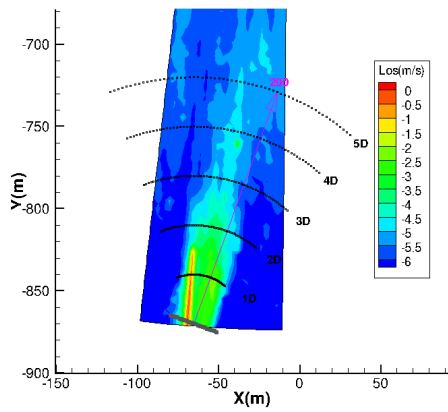


(a) Ten minutes average of 16:00 -16:10

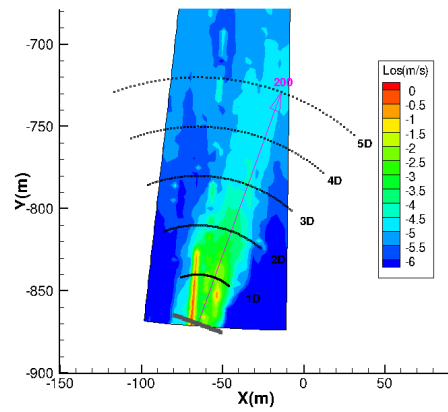


(b) Ten minutes average of 16:10 -16:20

Figure 7.13: Ten-minutes averaged line of sight velocity measured on 05-04-2014.

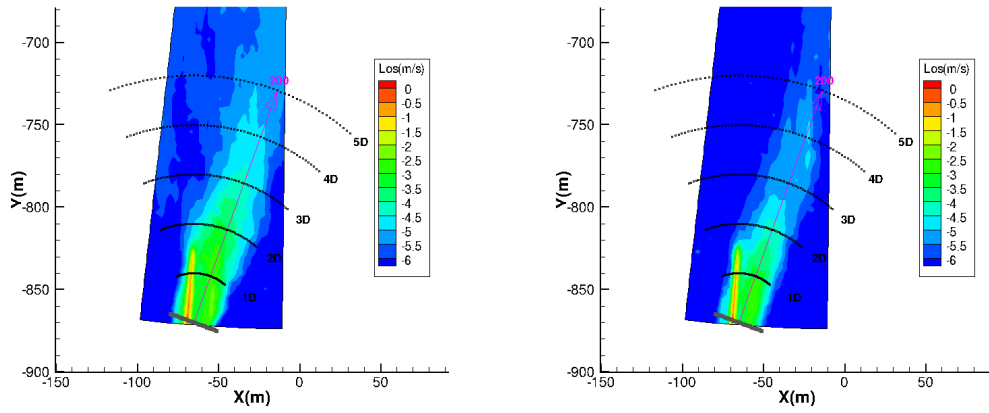


(a) Ten minutes average of 16:20 -16:30



(b) Ten minutes average of 16:30 -16:40

Figure 7.14: Ten-minutes averaged line of sight velocity measured on 05-04-2014.



(a) Ten minutes average of 16:40 -16:50

(b) Ten minutes average of 16:50 -16:60

Figure 7.15: Ten-minutes averaged line of sight velocity measured on 05-04-2014.

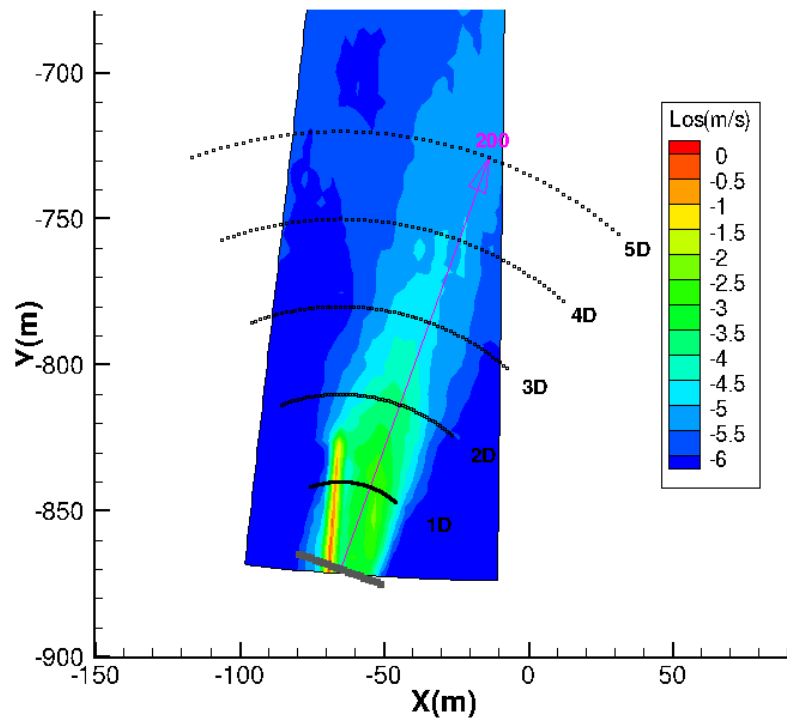
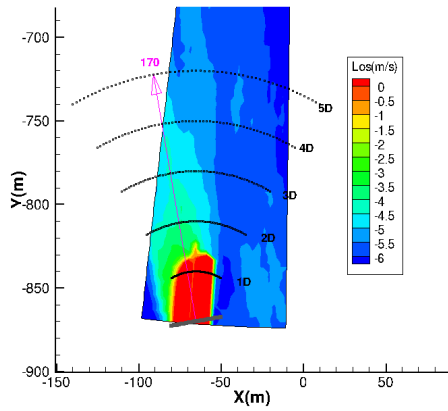
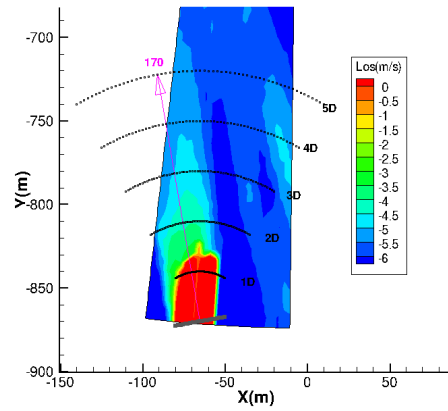


Figure 7.16: One-hour (16-17) averaged Line of sight velocity measured on 05-04-2014.

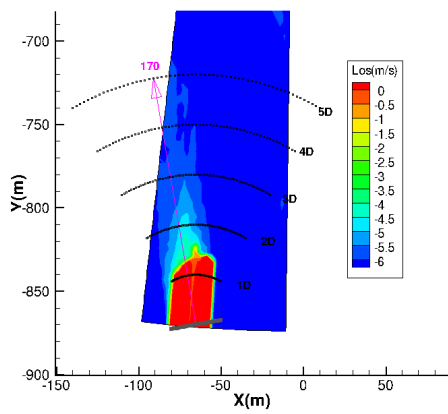


(a) Ten minutes average of 16:00 -16:10

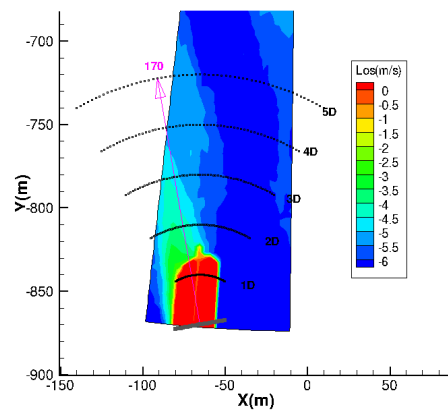


(b) Ten minutes average of 16:10 -16:20

Figure 7.17: Ten-minutes averaged line of sight velocity measured on 24-03-2014.

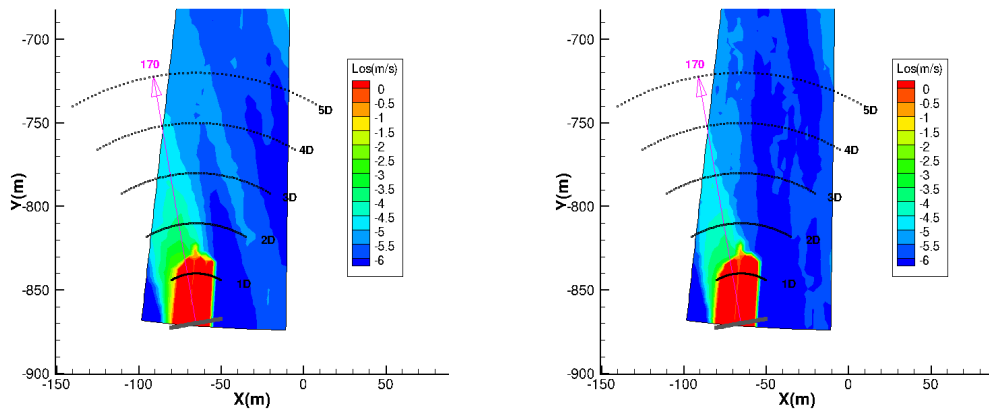


(a) Ten minutes average of 16:20 -16:30



(b) Ten minutes average of 16:30 -16:40

Figure 7.18: Ten-minutes averaged line of sight velocity measured on 24-03-2014.



(a) Ten minutes average of 16:40 -16:50

(b) Ten minutes average of 16:50 -16:60

Figure 7.19: Ten-minutes averaged line of sight velocity measured on 24-03-2014.

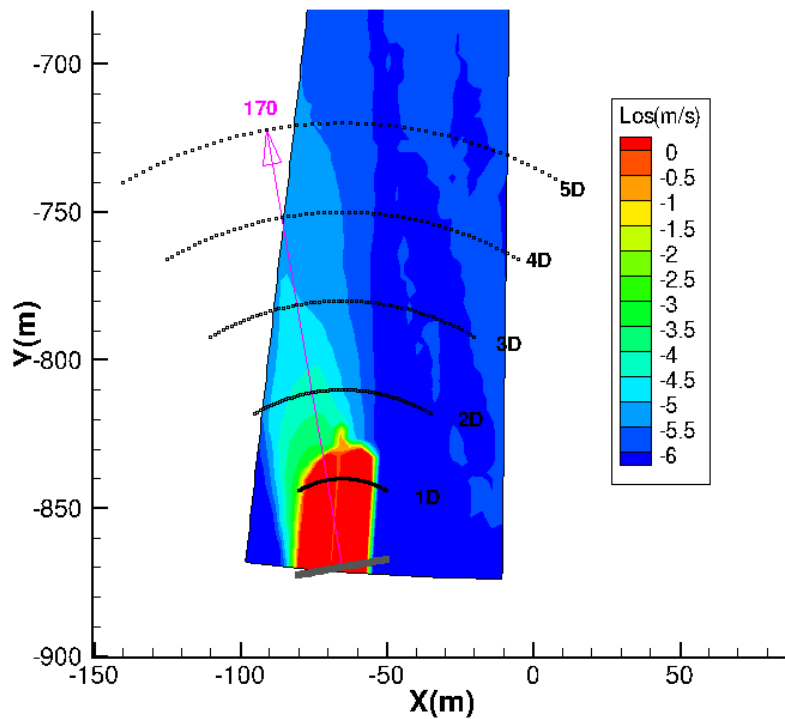
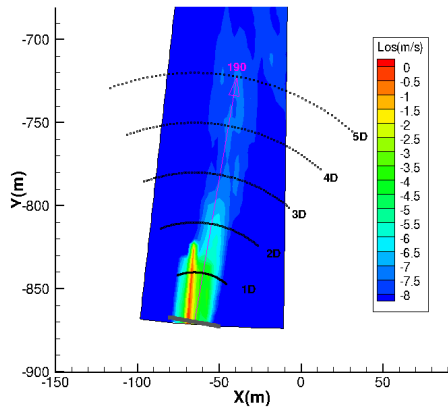
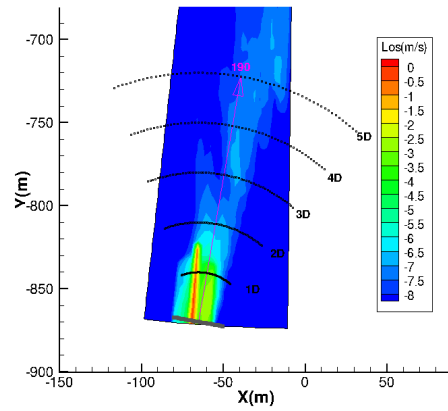


Figure 7.20: One-hour (16-17) averaged Line of sight velocity measured on 24-03-2014.

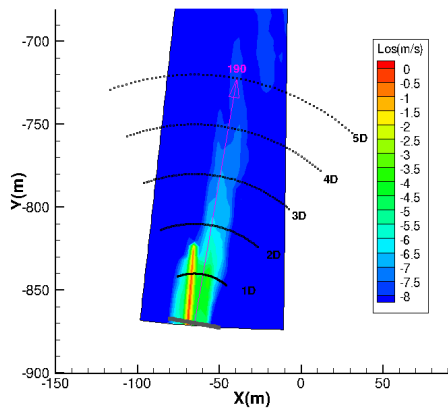


(a) Ten minutes average of 21:00 -21:10

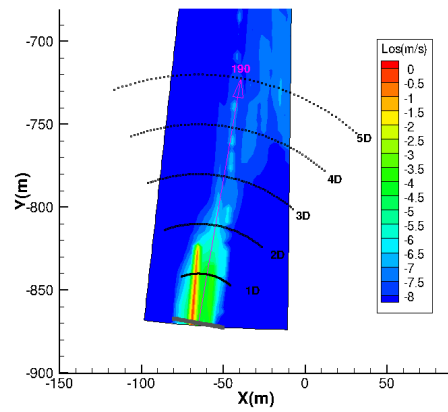


(b) Ten minutes average of 21:10 -21:20

Figure 7.21: Ten-minutes averaged line of sight velocity measured on 21-03-2014.

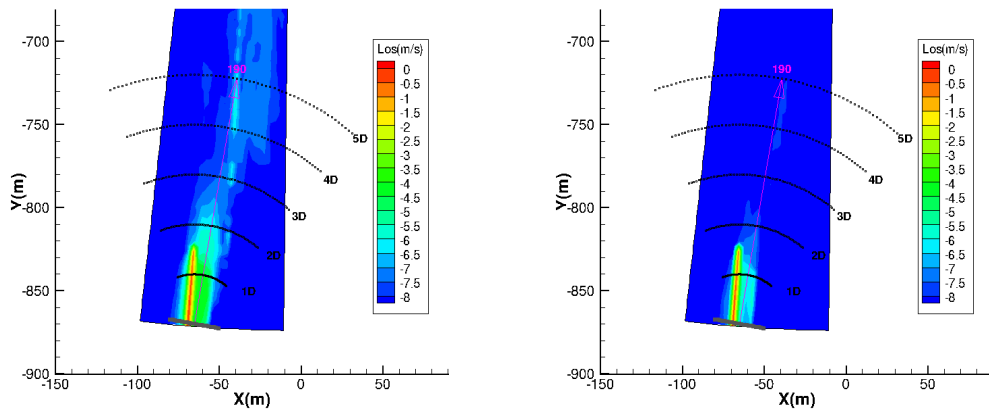


(a) Ten minutes average of 21:20 -21:30



(b) Ten minutes average of 21:30 -21:40

Figure 7.22: Ten-minutes averaged line of sight velocity measured on 21-03-2014.



(a) Ten minutes average of 21:40 -21:50

(b) Ten minutes average of 21:50 -21:60

Figure 7.23: Ten-minutes averaged line of sight velocity measured on 21-03-2014.

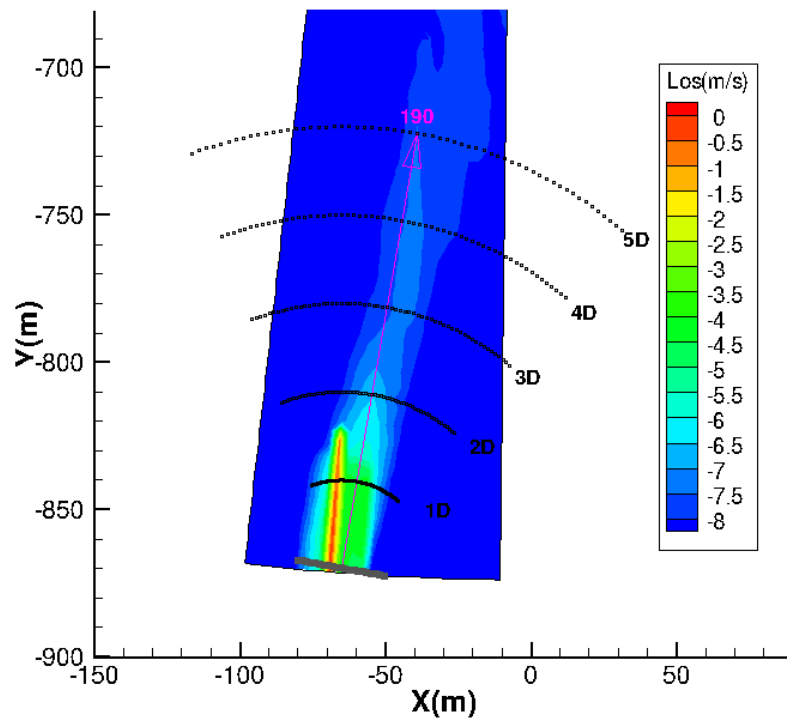
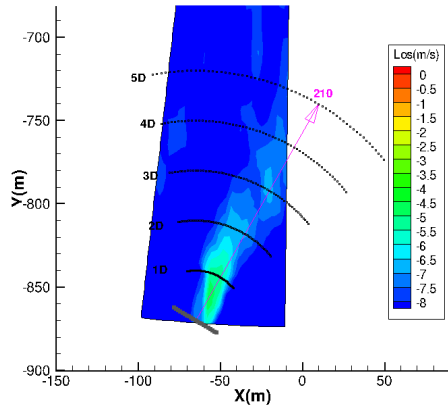
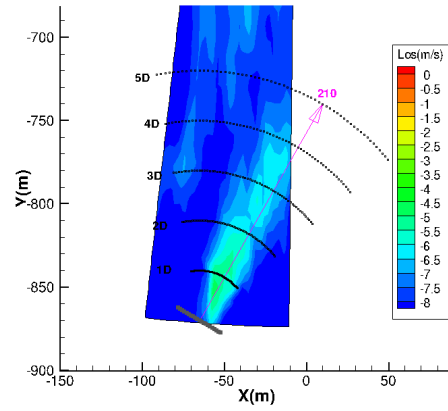


Figure 7.24: One-hour (21-22) averaged Line of sight velocity measured on 21-03-2014.

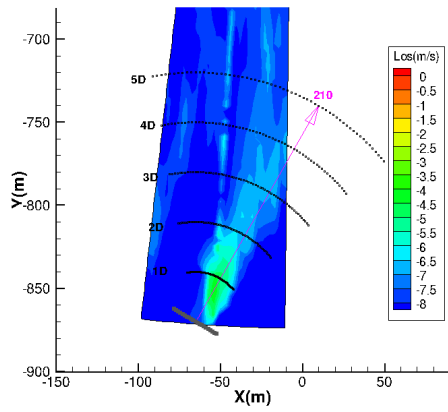


(a) Ten minutes average of 04:00 -04:10

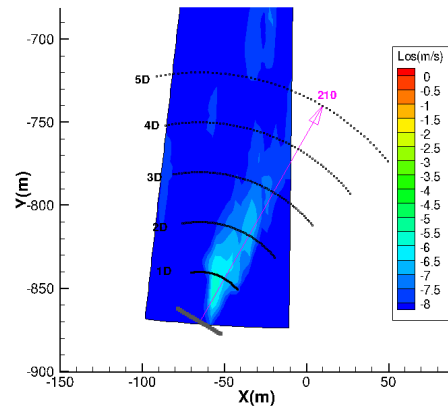


(b) Ten minutes average of 04:10 -04:20

Figure 7.25: Ten-minutes averaged line of sight velocity measured on 20-03-2014.

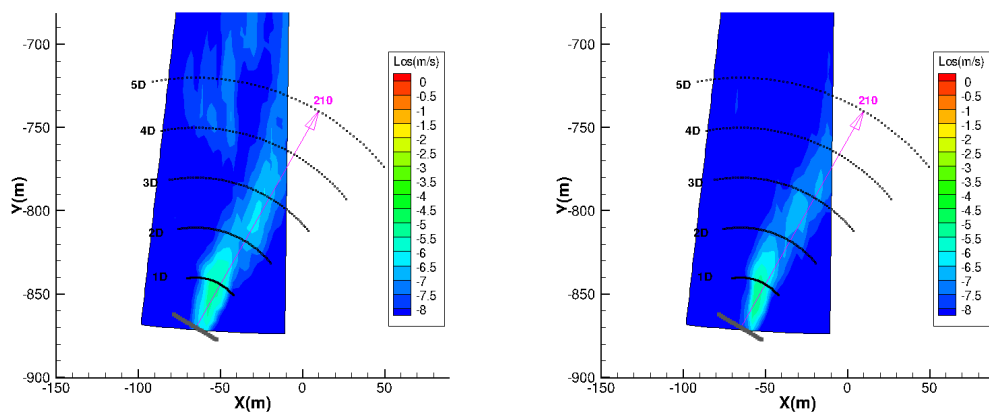


(a) Ten minutes average of 04:20 -04:30



(b) Ten minutes average of 04:30 -04:40

Figure 7.26: Ten-minutes averaged line of sight velocity measured on 20-03-2014.



(a) Ten minutes average of 04:40 -04:50

(b) Ten minutes average of 04:50 -04:60

Figure 7.27: Ten-minutes averaged line of sight velocity measured on 20-03-2014.

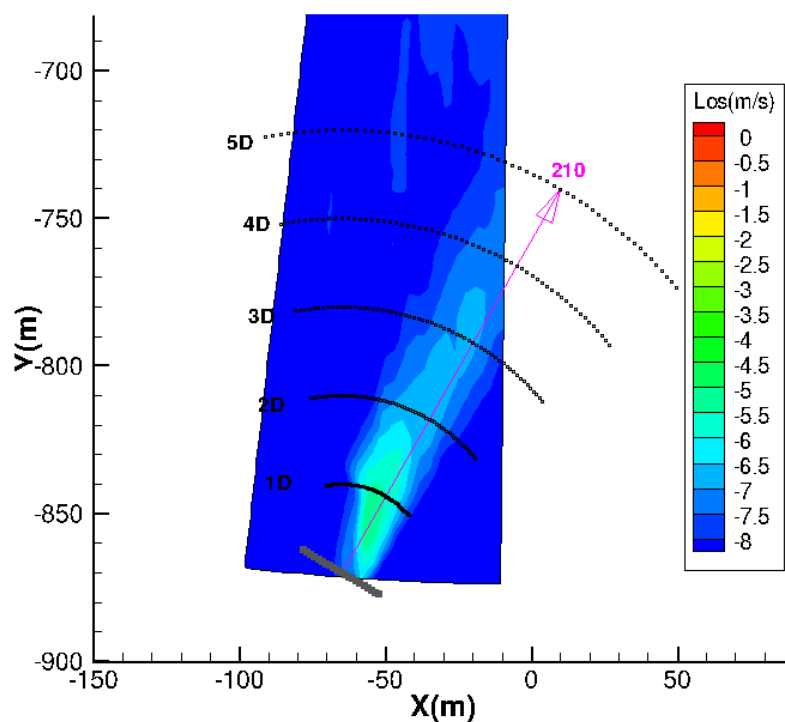


Figure 7.28: One-hour (04-05) averaged Line of sight velocity measured on 20-03-2014.

Chapter 8

Appendix: Piloted Flight Simulation Results

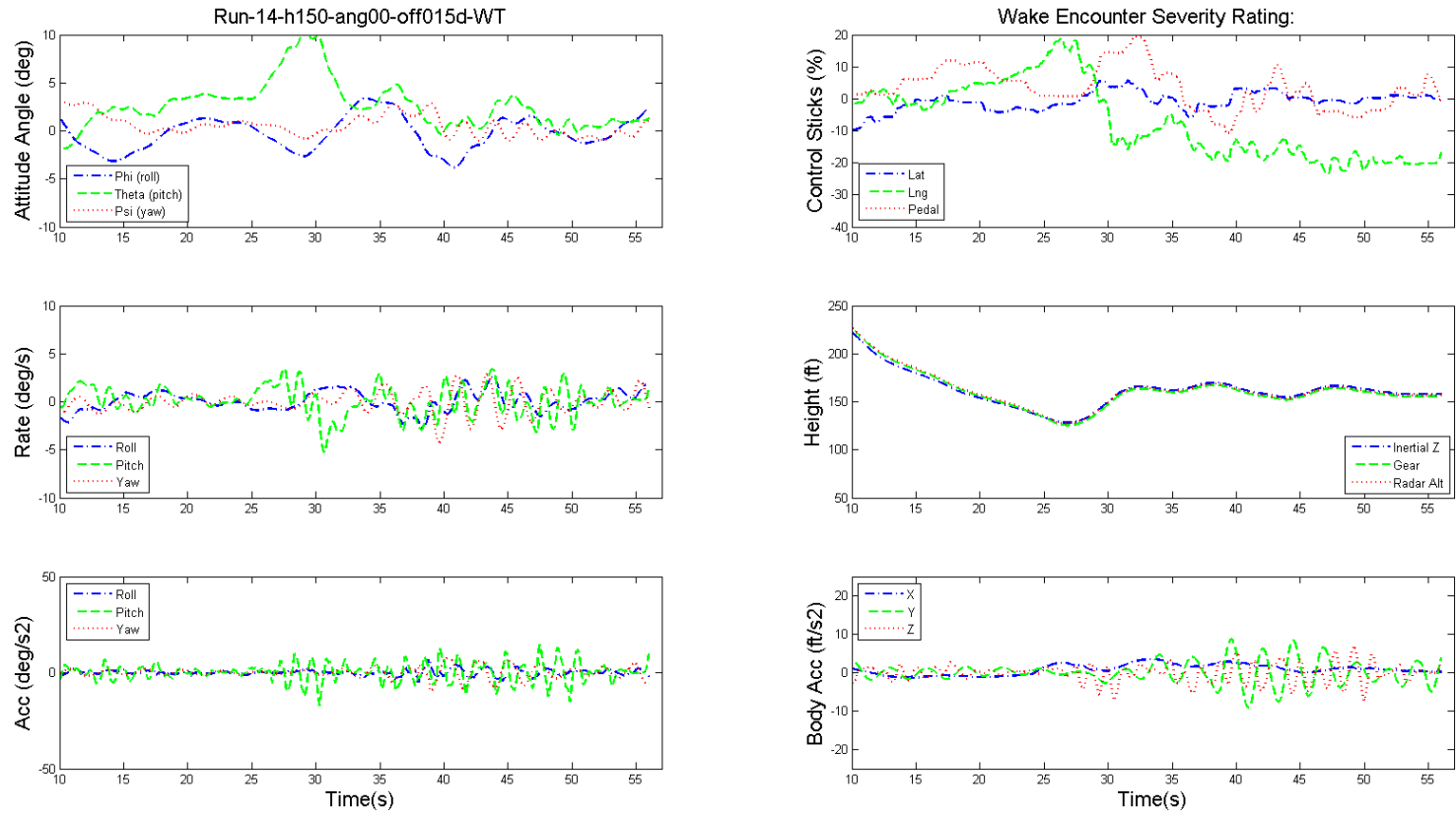


Figure 8.1: Time history of the dynamics of GA aircraft and pilot's controls during wake encounter, wind turbine hub height 150 ft, wind speed 10 m/s, angle 90.0, offset 3D.

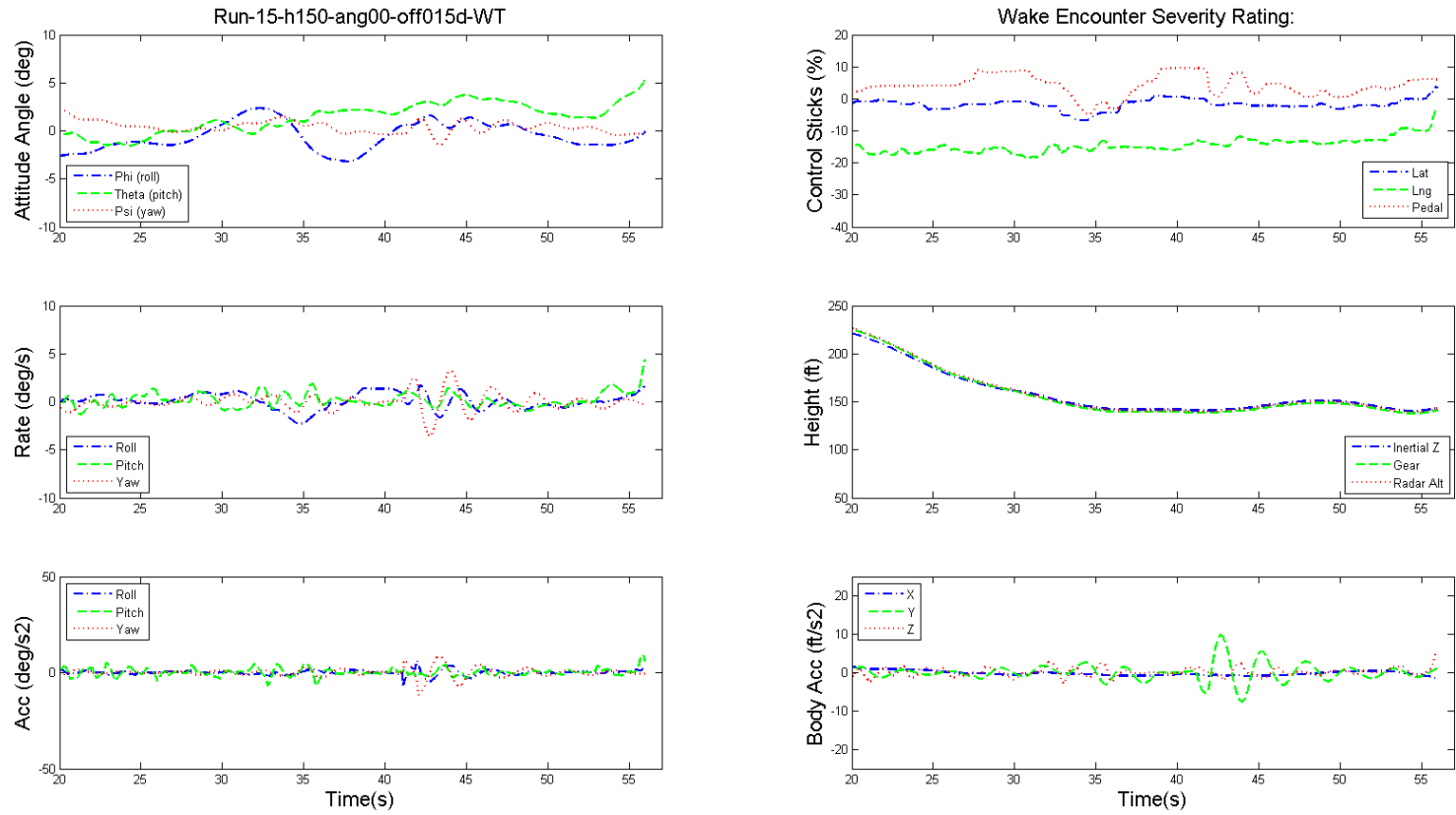


Figure 8.2: Time history of the dynamics of GA aircraft and pilot's controls during wake encounter, wind turbine hub height 150 ft, wind speed 10 m/s, angle 90.0, offset 3D.

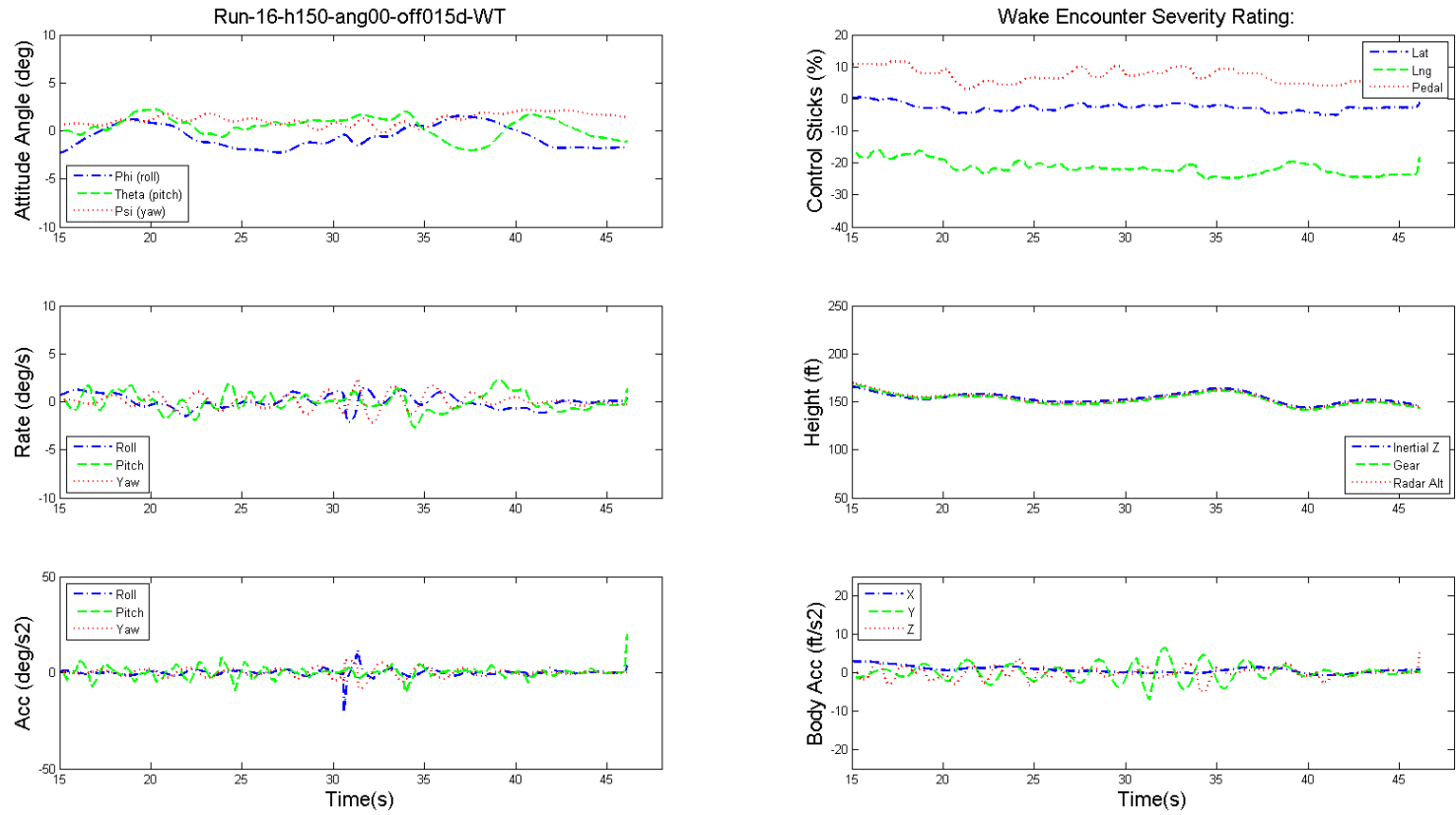


Figure 8.3: Time history of the dynamics of GA aircraft and pilot's controls during wake encounter, wind turbine hub height 150 ft, wind speed 10 m/s, angle 90.0, offset 1.5D.

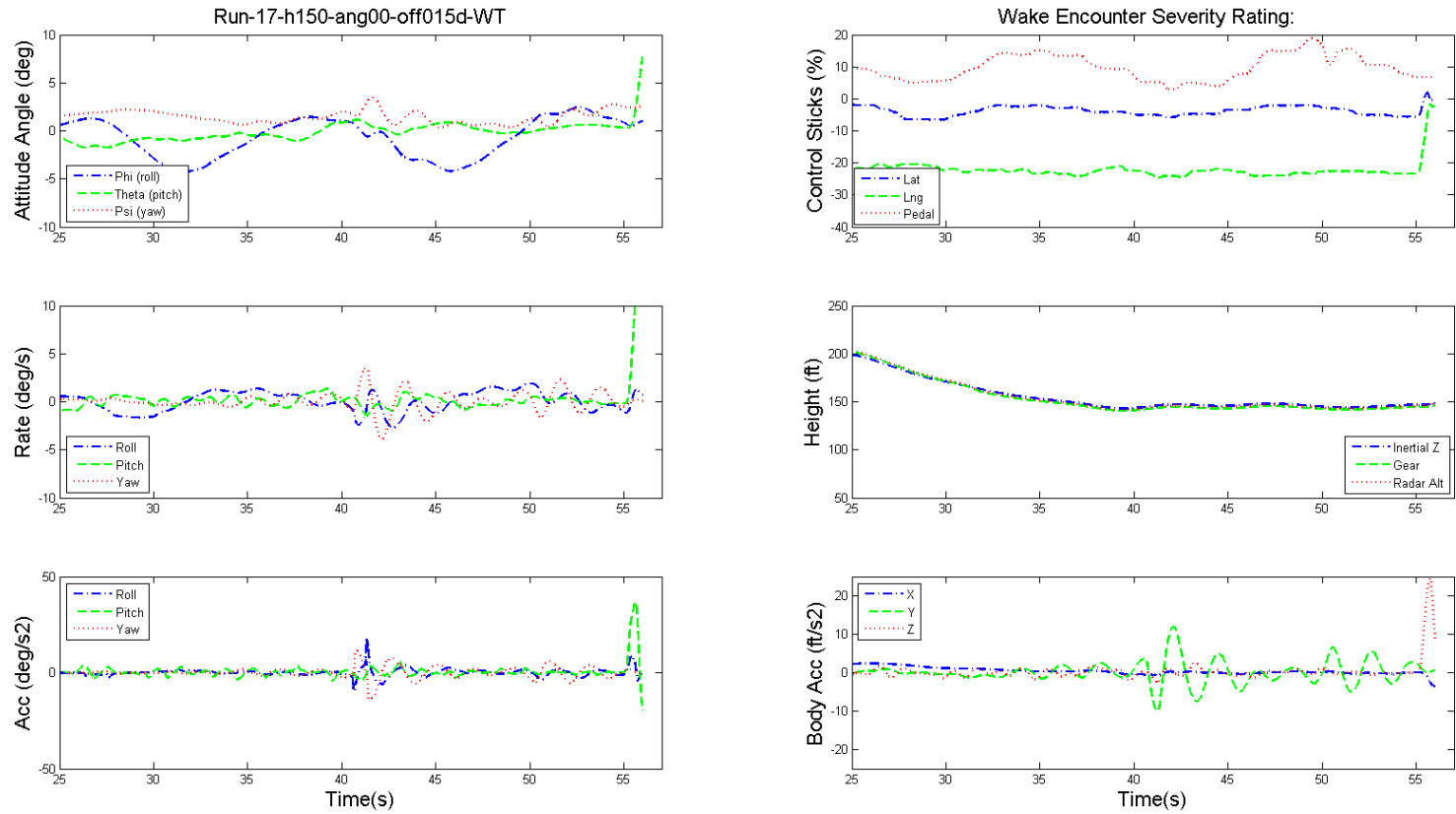


Figure 8.4: Time history of the dynamics of GA aircraft and pilot's controls during wake encounter, wind turbine hub height 150 ft, wind speed 10 m/s, angle 90.0, offset 1.5D.

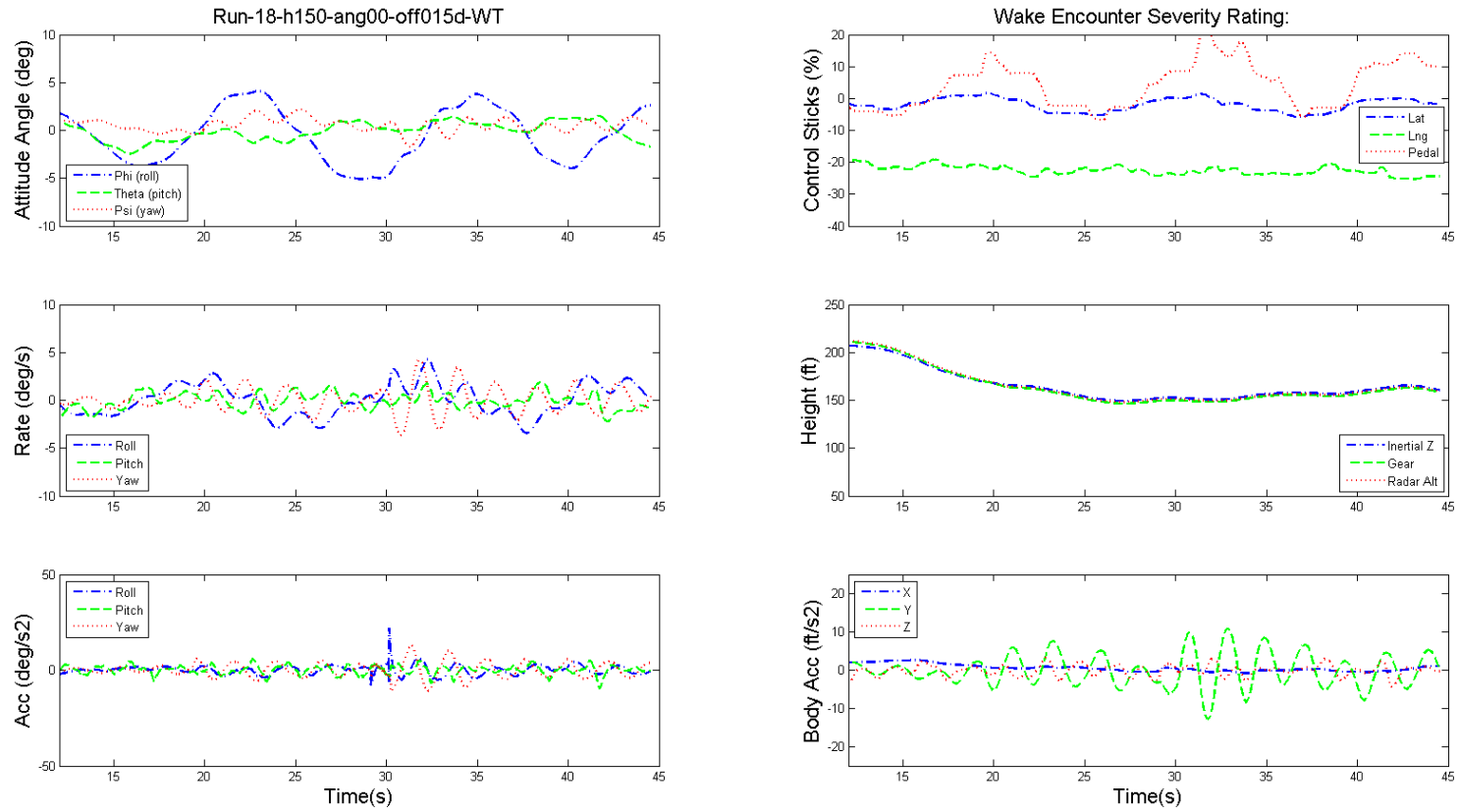


Figure 8.5: Time history of the dynamics of GA aircraft and pilot's controls during wake encounter, wind turbine hub height 150 ft, wind speed 10 m/s, angle 45.0, offset 1.0D.

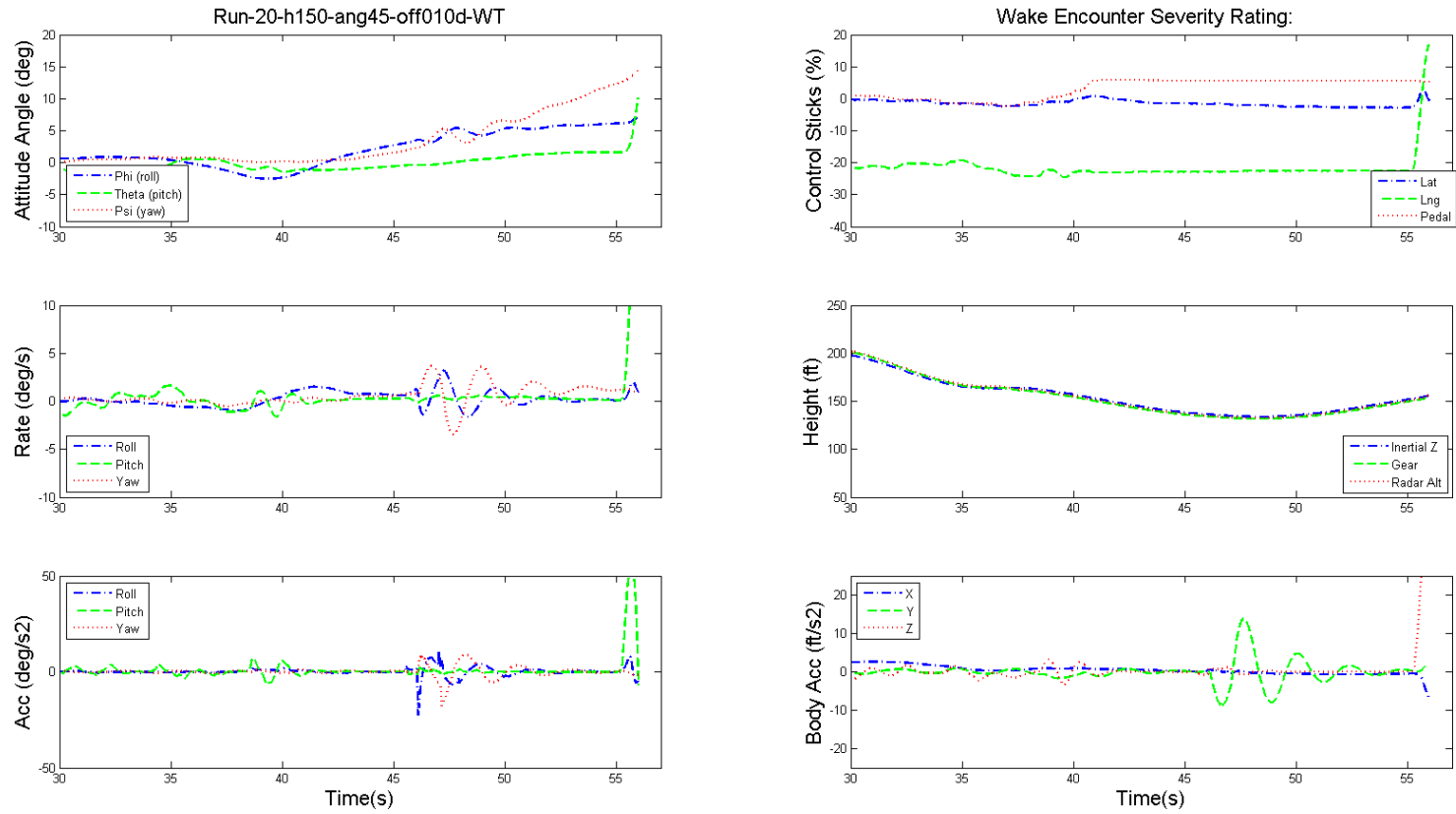


Figure 8.6: Time history of the dynamics of GA aircraft and pilot's controls during wake encounter, wind turbine hub height 150 ft, wind speed 10 m/s, angle 45.0, offset 1.0D, hands-off.

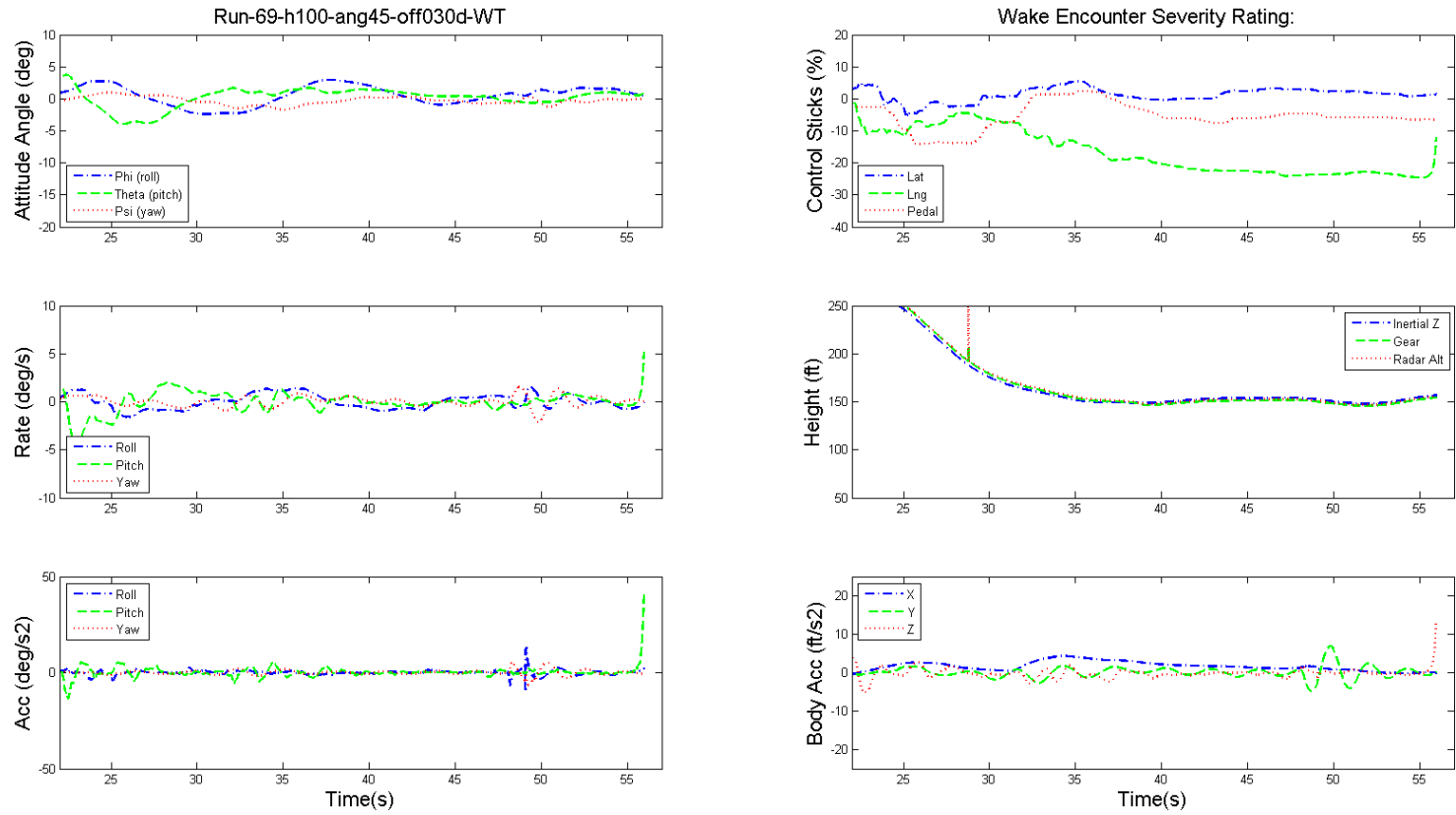


Figure 8.7: Time history of the dynamics of GA aircraft and pilot's controls during wake encounter, wind turbine hub height 150 ft, wind speed 10 m/s, angle 45.0, offset 3.0D.

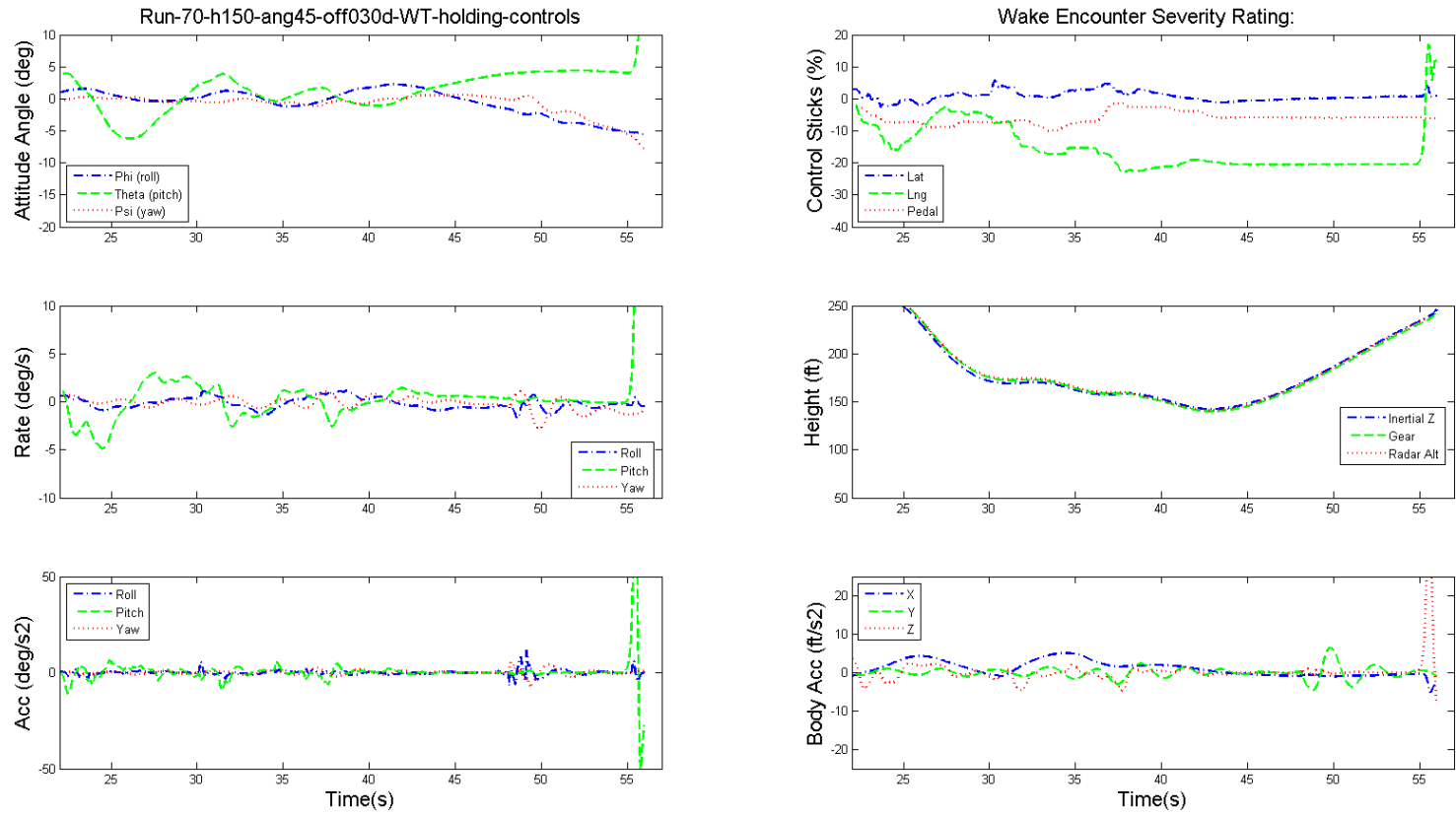


Figure 8.8: Time history of the dynamics of GA aircraft and pilot's controls during wake encounter, wind turbine hub height 150 ft, wind speed 10 m/s, angle 45.0, offset 3.0D, hands-off.

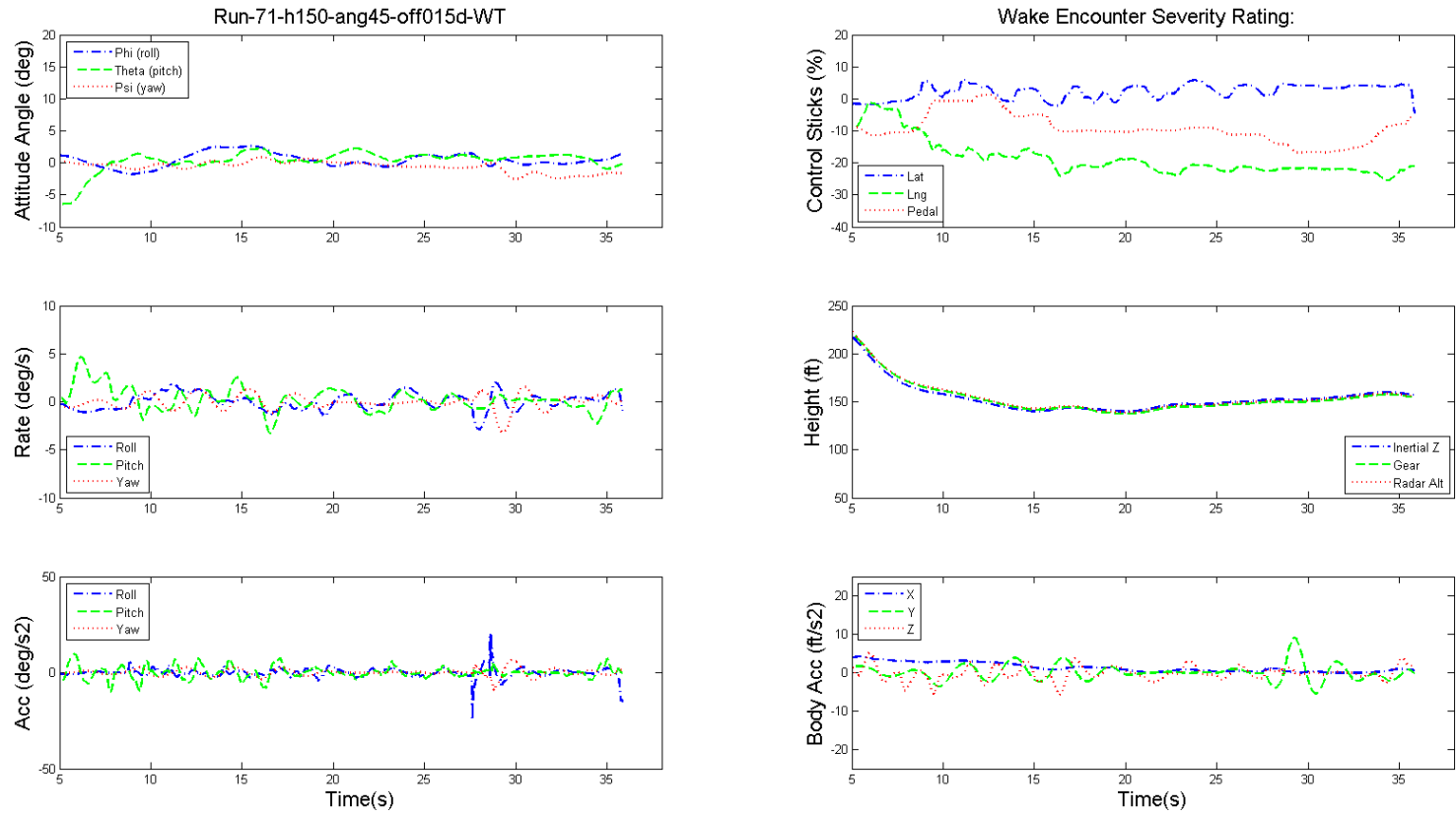


Figure 8.9: Time history of the dynamics of GA aircraft and pilot's controls during wake encounter, wind turbine hub height 150 ft, wind speed 10 m/s, angle 45.0, offset 1.5D.

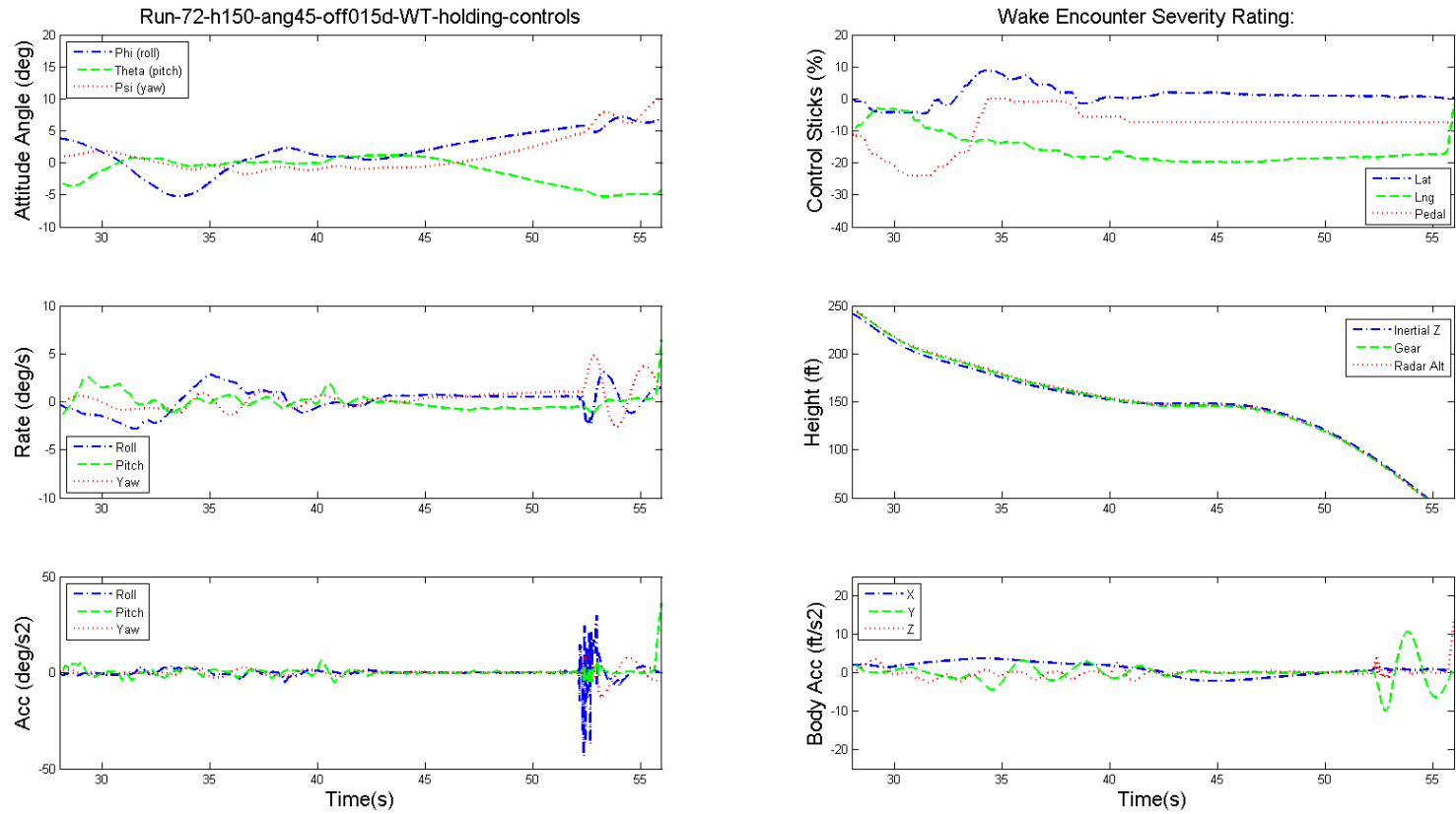


Figure 8.10: Time history of the dynamics of GA aircraft and pilot's controls during wake encounter, wind turbine hub height 150 ft, wind speed 10 m/s, angle 45.0, offset 1.5D, hands-off.

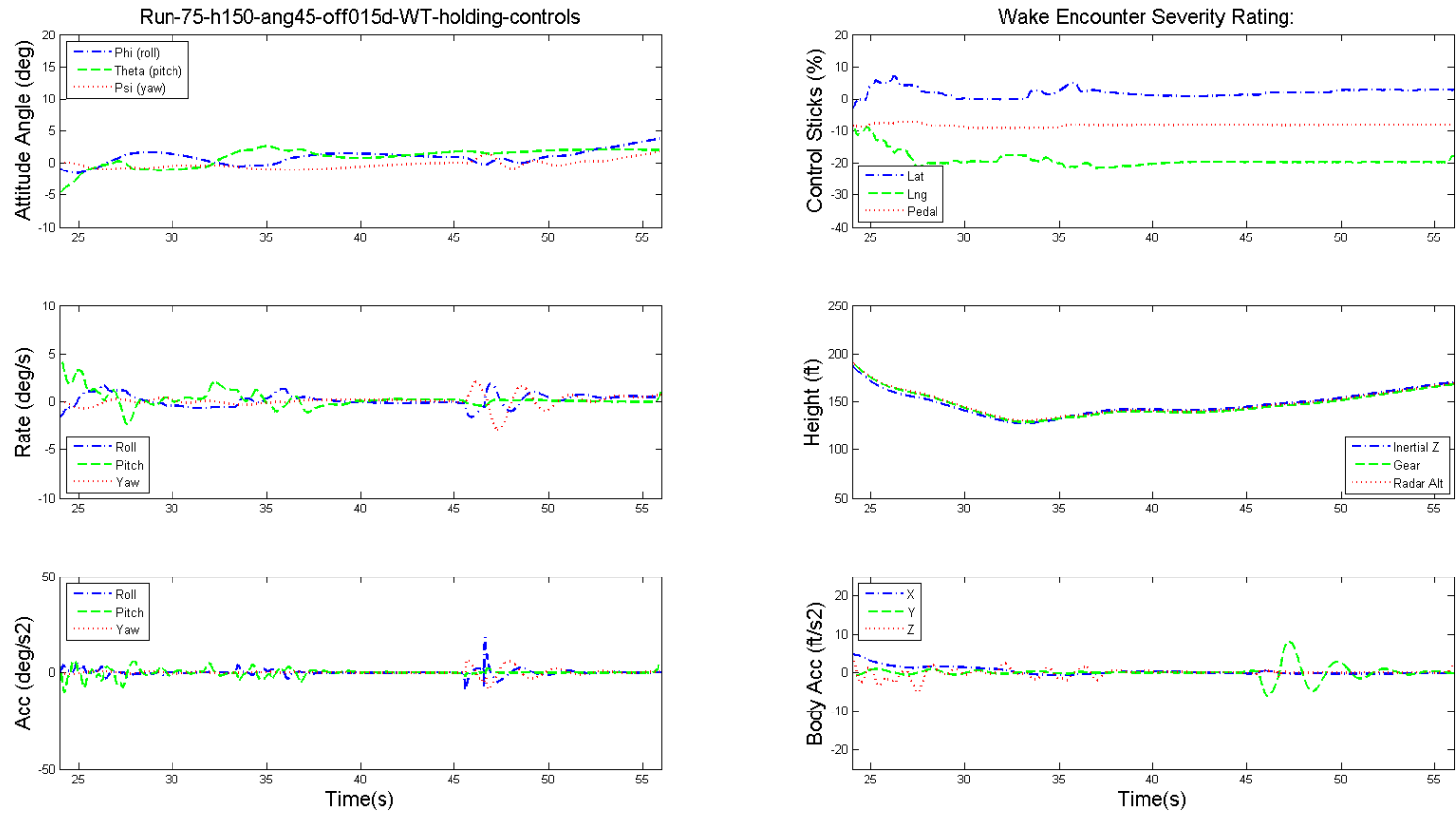


Figure 8.11: Time history of the dynamics of GA aircraft and pilot's controls during wake encounter, wind turbine hub height 150 ft, wind speed 10 m/s, angle 45.0, offset 1.5D, hands-off.

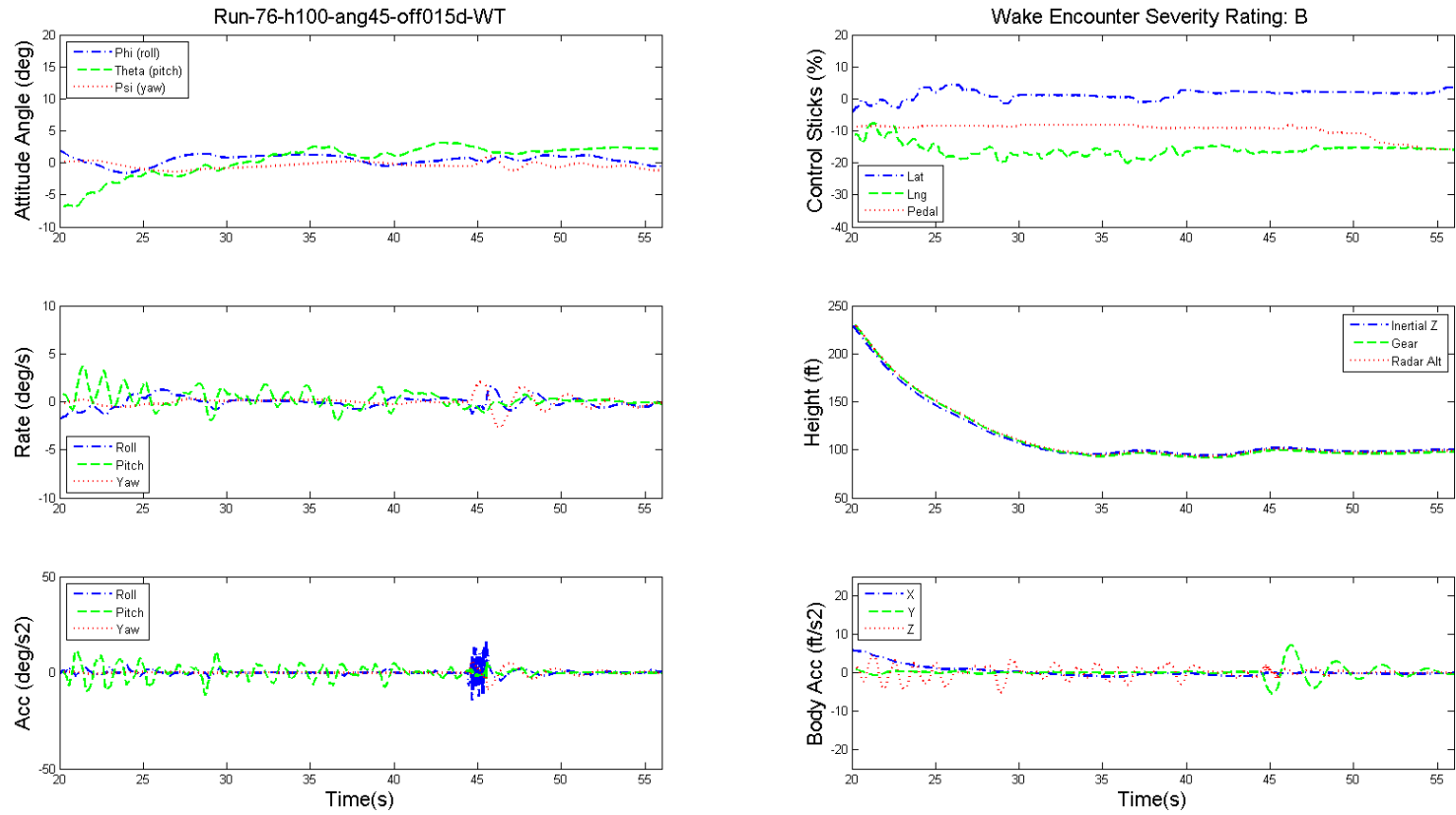


Figure 8.12: Time history of the dynamics of GA aircraft and pilot's controls during wake encounter, wind turbine hub height 100 ft, wind speed 10 m/s, angle 45.0, offset 1.5D.

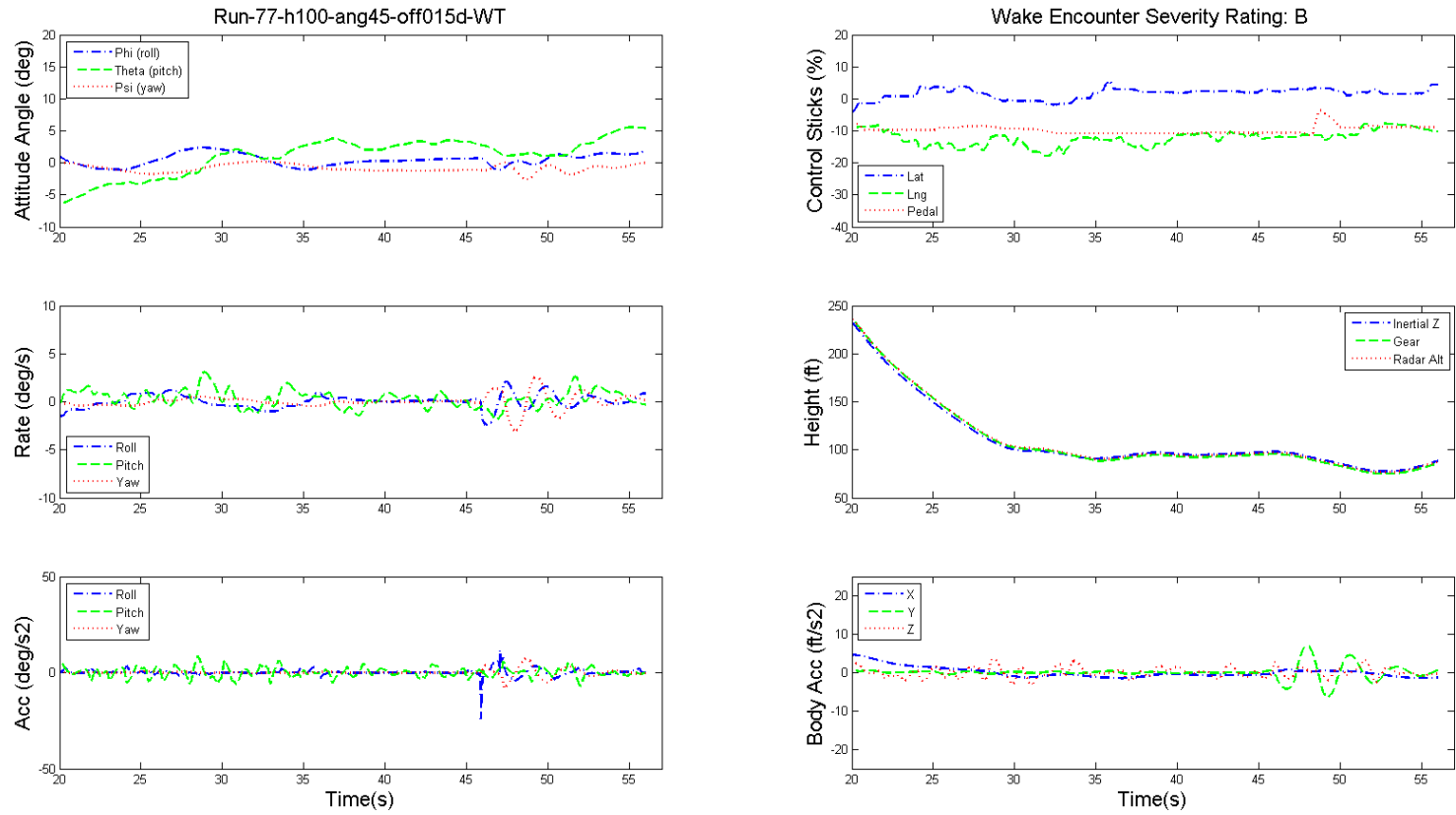


Figure 8.13: Time history of the dynamics of GA aircraft and pilot's controls during wake encounter, wind turbine hub height 100 ft, wind speed 10 m/s, angle 45.0, offset 1.5D.

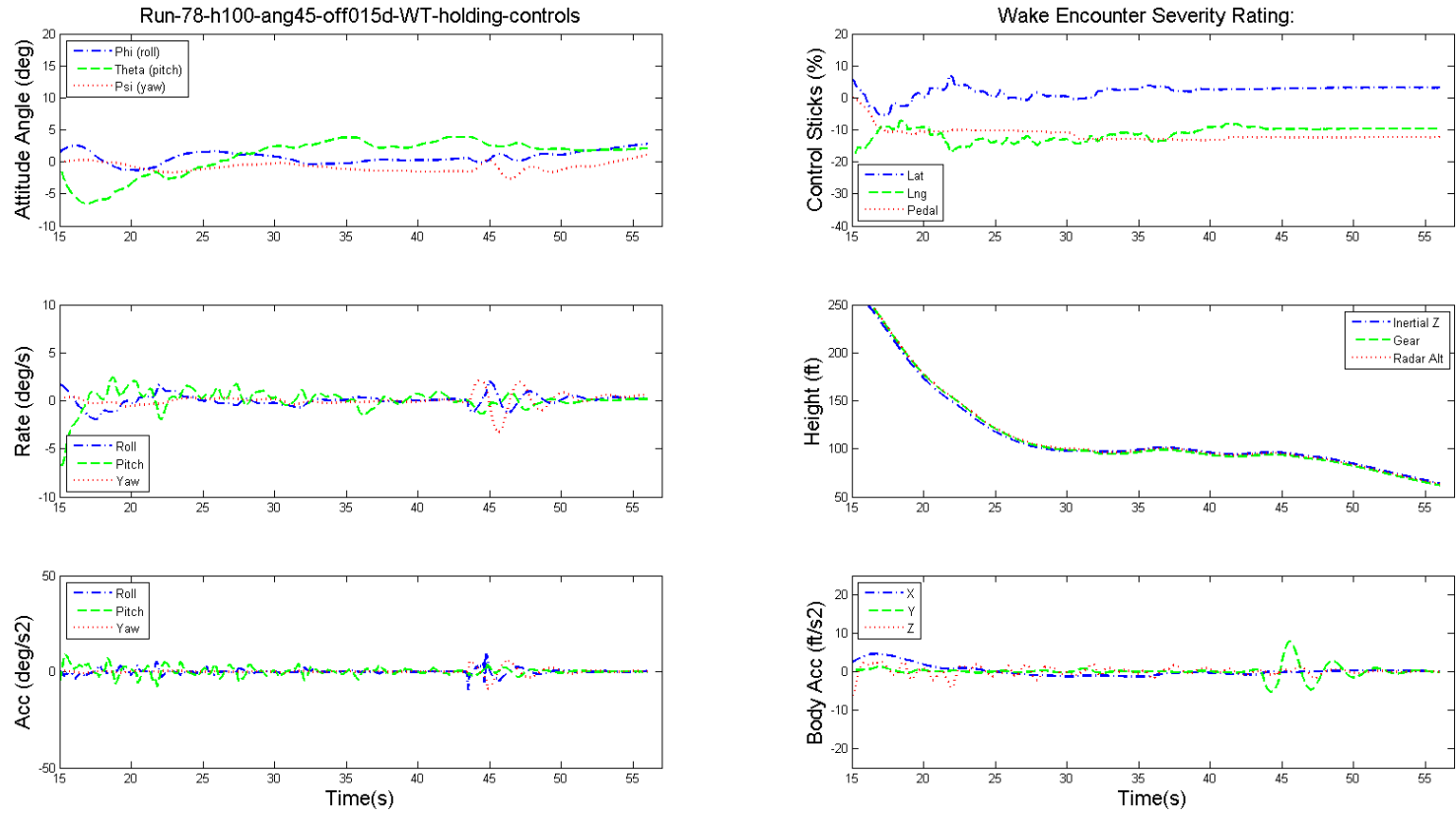


Figure 8.14: Time history of the dynamics of GA aircraft and pilot's controls during wake encounter, wind turbine hub height 100 ft, wind speed 10 m/s, angle 45.0, offset 1.5D, hands-off.

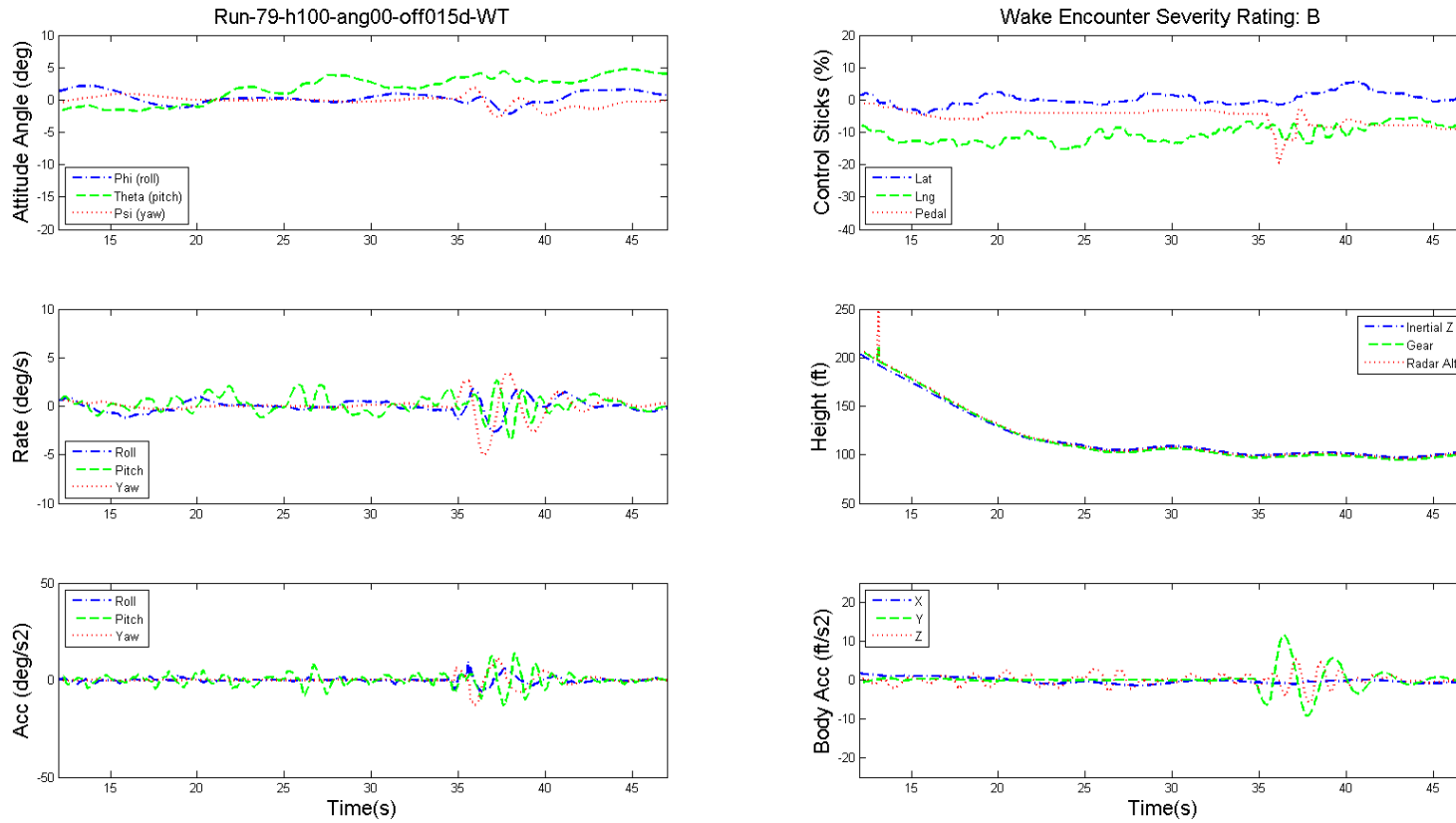


Figure 8.15: Time history of the dynamics of GA aircraft and pilot's controls during wake encounter, wind turbine hub height 100 ft, wind speed 10 m/s, angle 90.0, offset 1.5D.

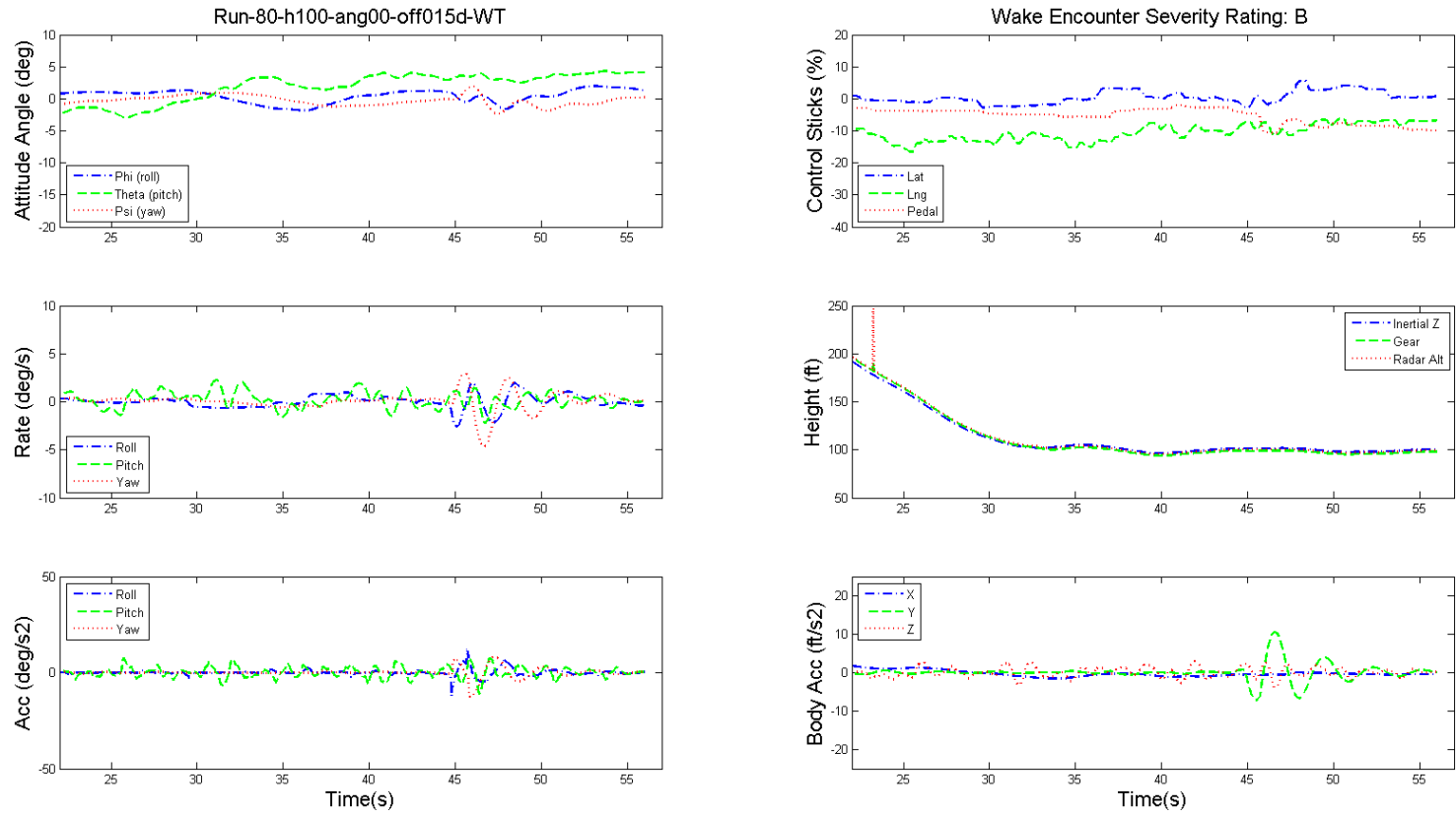


Figure 8.16: Time history of the dynamics of GA aircraft and pilot's controls during wake encounter, wind turbine hub height 100 ft, wind speed 10 m/s, angle 90.0, offset 1.5D.

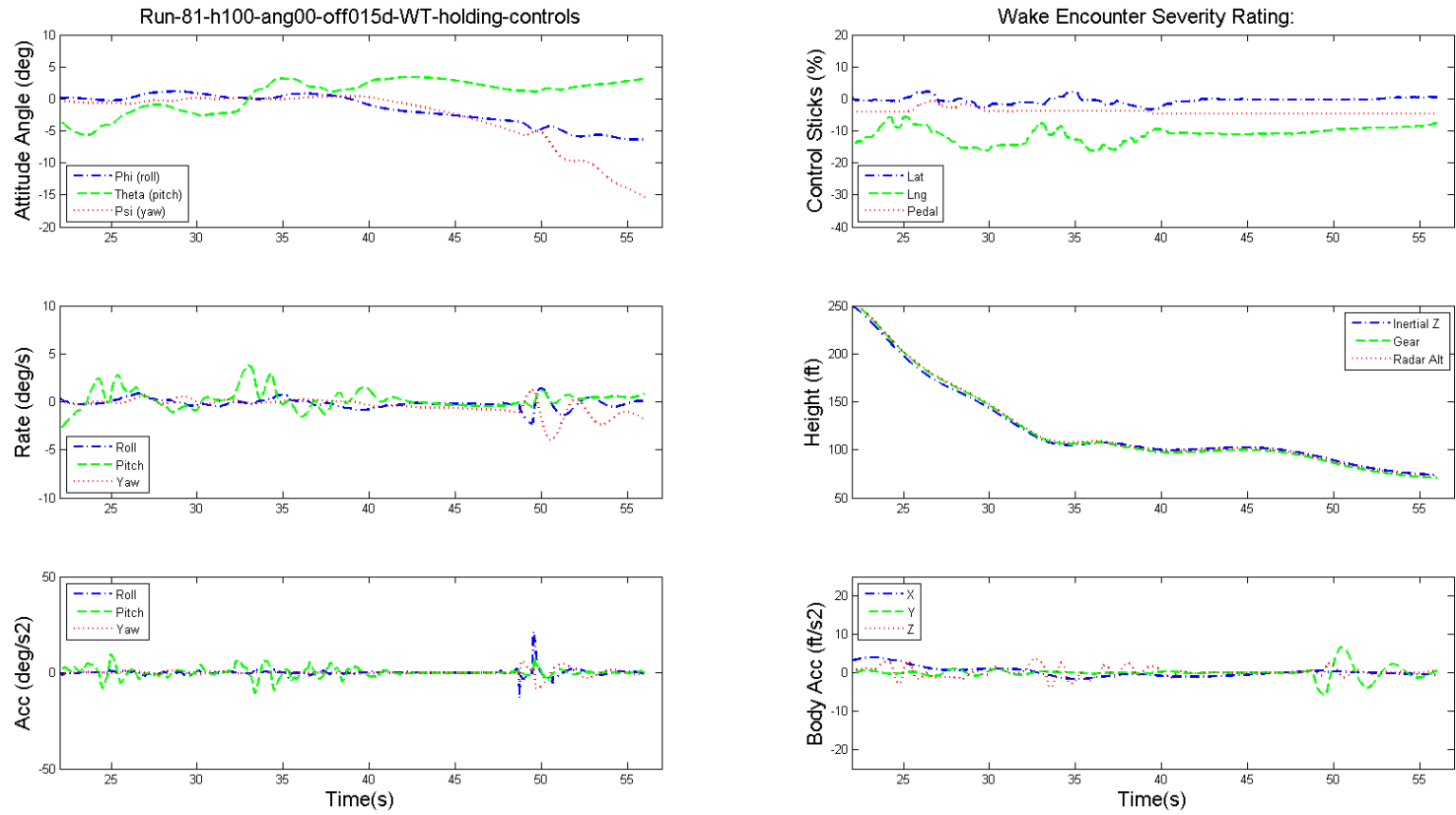


Figure 8.17: Time history of the dynamics of GA aircraft and pilot's controls during wake encounter, wind turbine hub height 100 ft, wind speed 10 m/s, angle 90.0, offset 1.5D, hands-off.

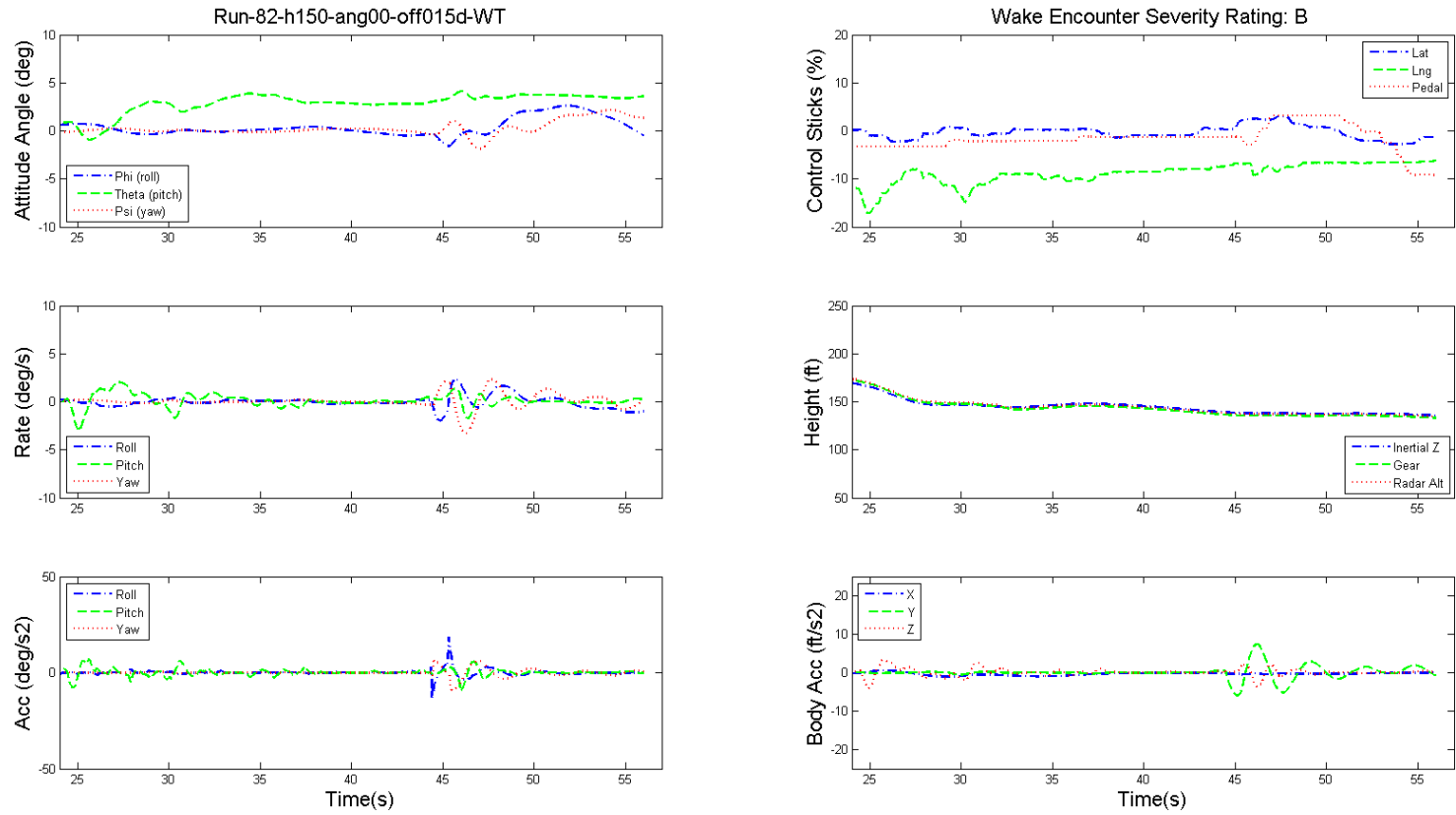


Figure 8.18: Time history of the dynamics of GA aircraft and pilot's controls during wake encounter, wind turbine hub height 150 ft, wind speed 10 m/s, angle 90.0, offset 1.5D.

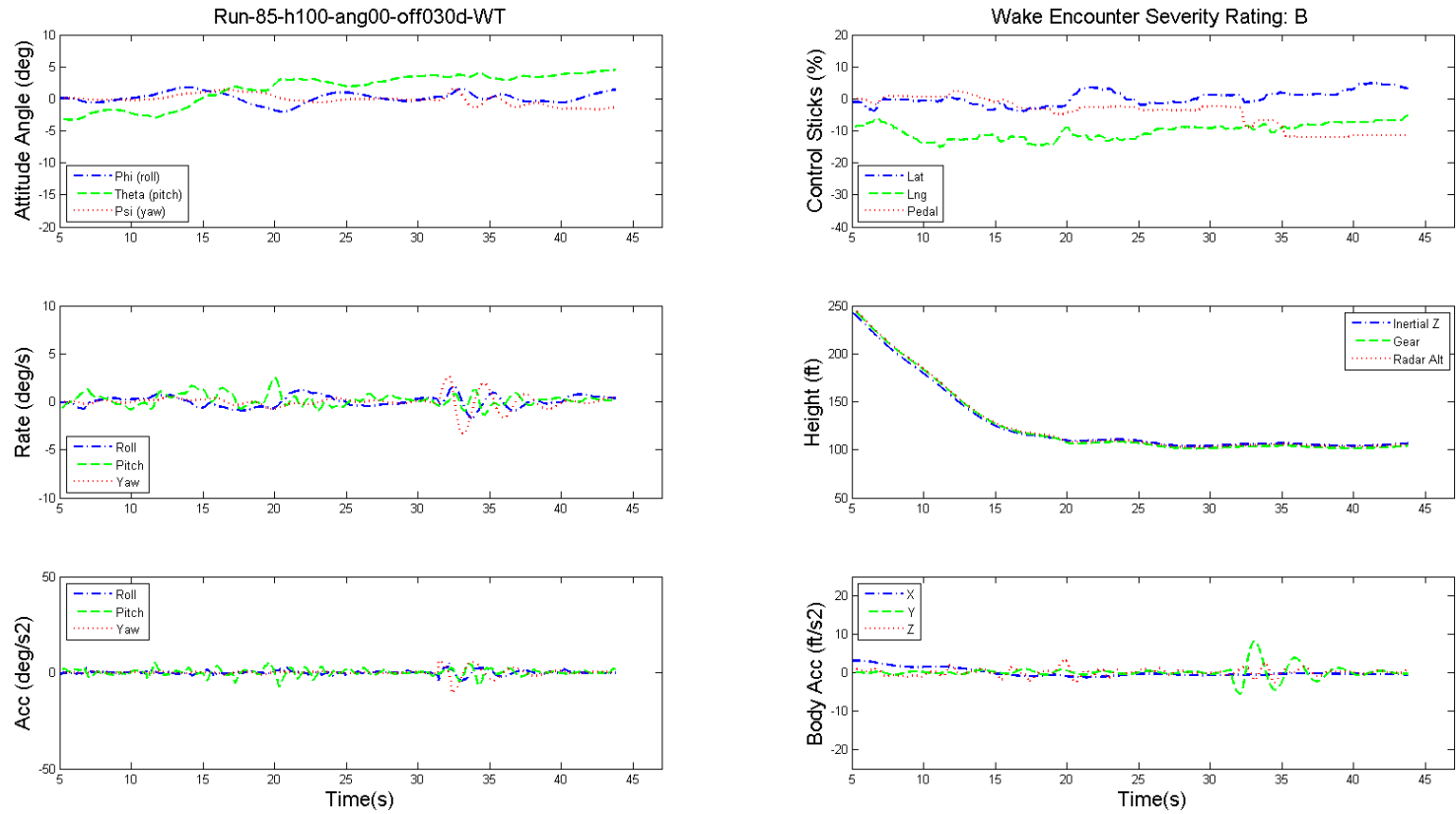


Figure 8.19: Time history of the dynamics of GA aircraft and pilot's controls during wake encounter, wind turbine hub height 100 ft, wind speed 10 m/s, angle 90.0, offset 3.0D.

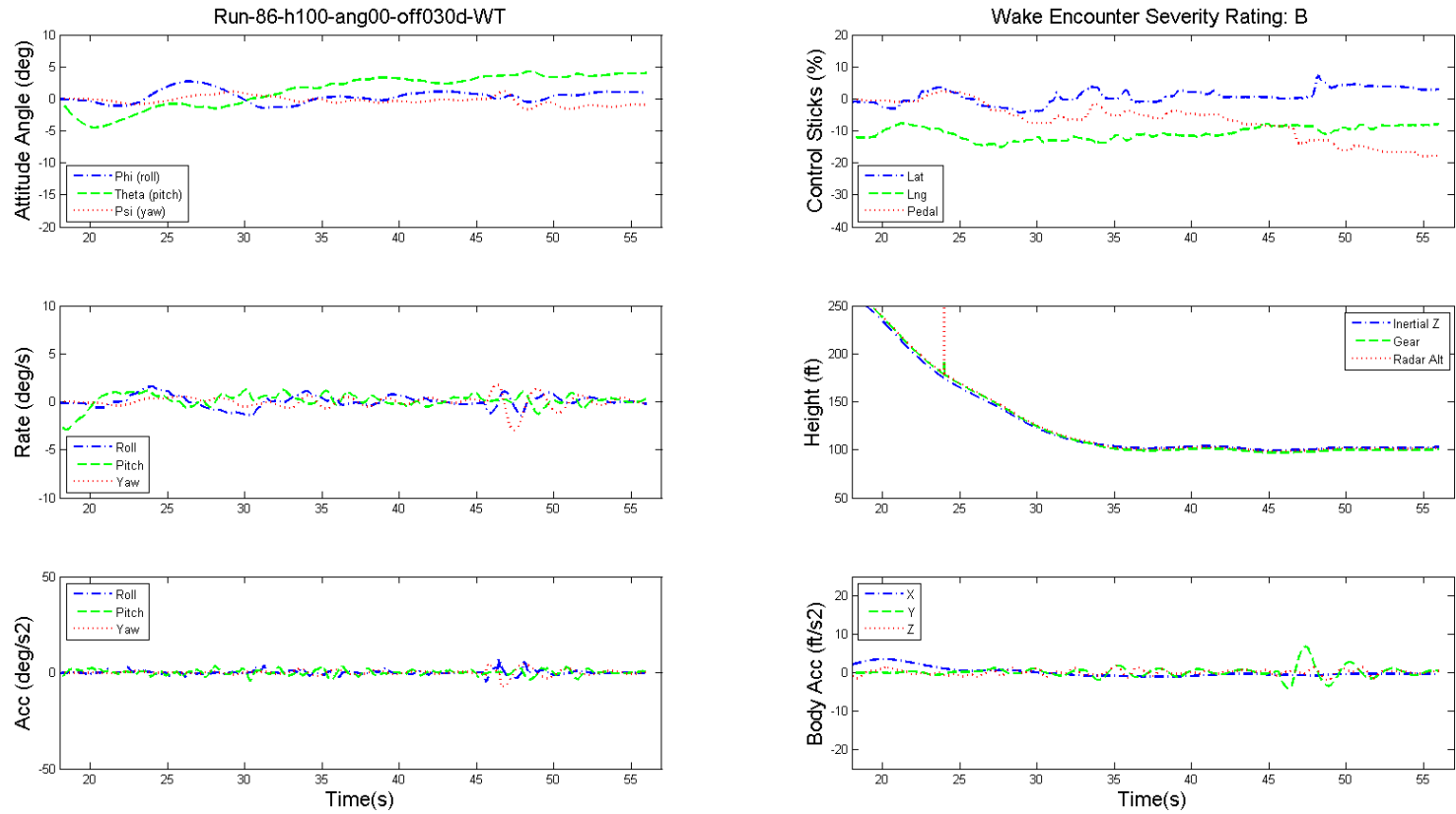


Figure 8.20: Time history of the dynamics of GA aircraft and pilot's controls during wake encounter, wind turbine hub height 100 ft, wind speed 10 m/s, angle 90.0, offset 3.0D.

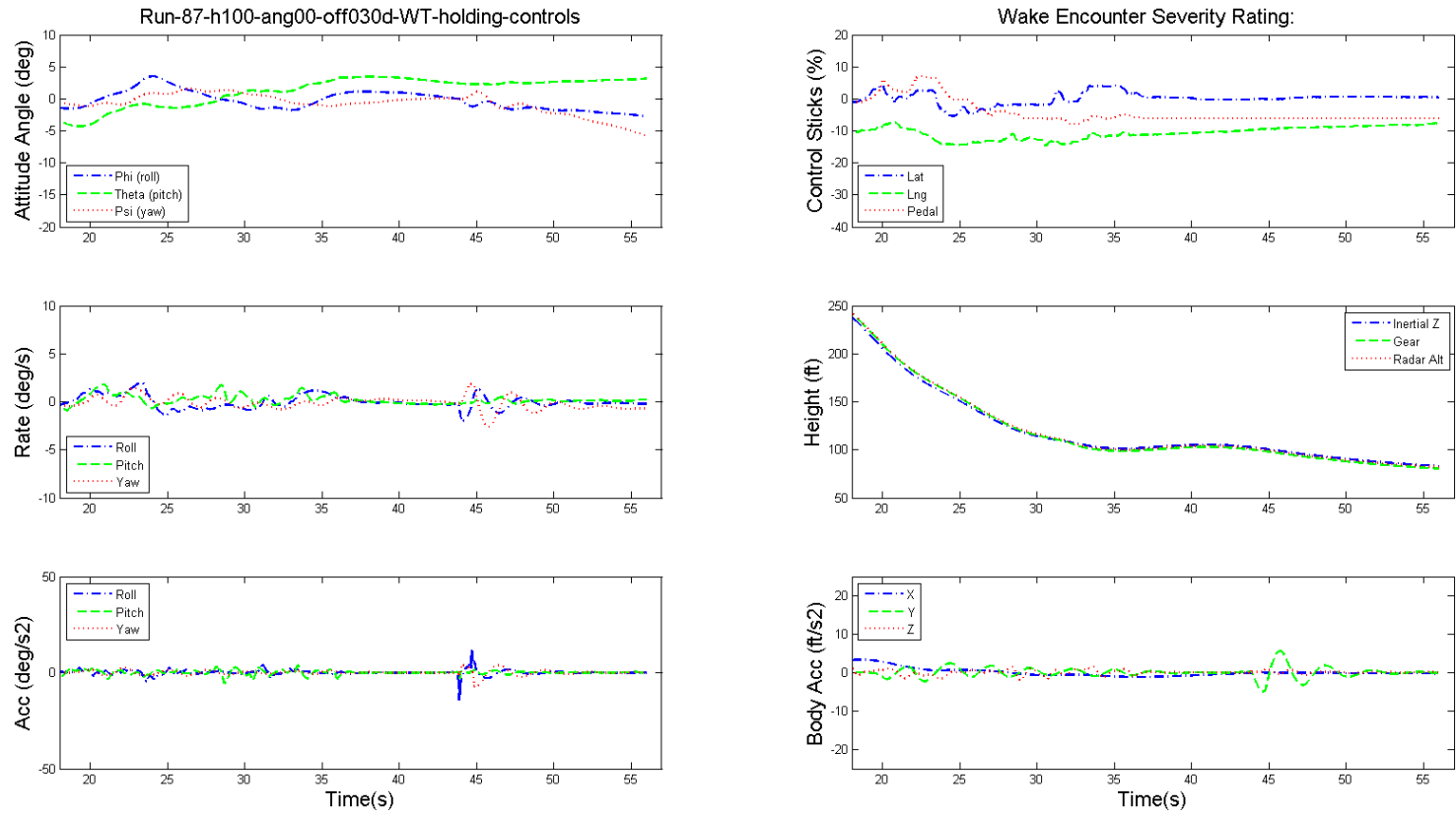


Figure 8.21: Time history of the dynamics of GA aircraft and pilot's controls during wake encounter, wind turbine hub height 100 ft, wind speed 10 m/s, angle 90.0, offset 3.0D, hands-off.

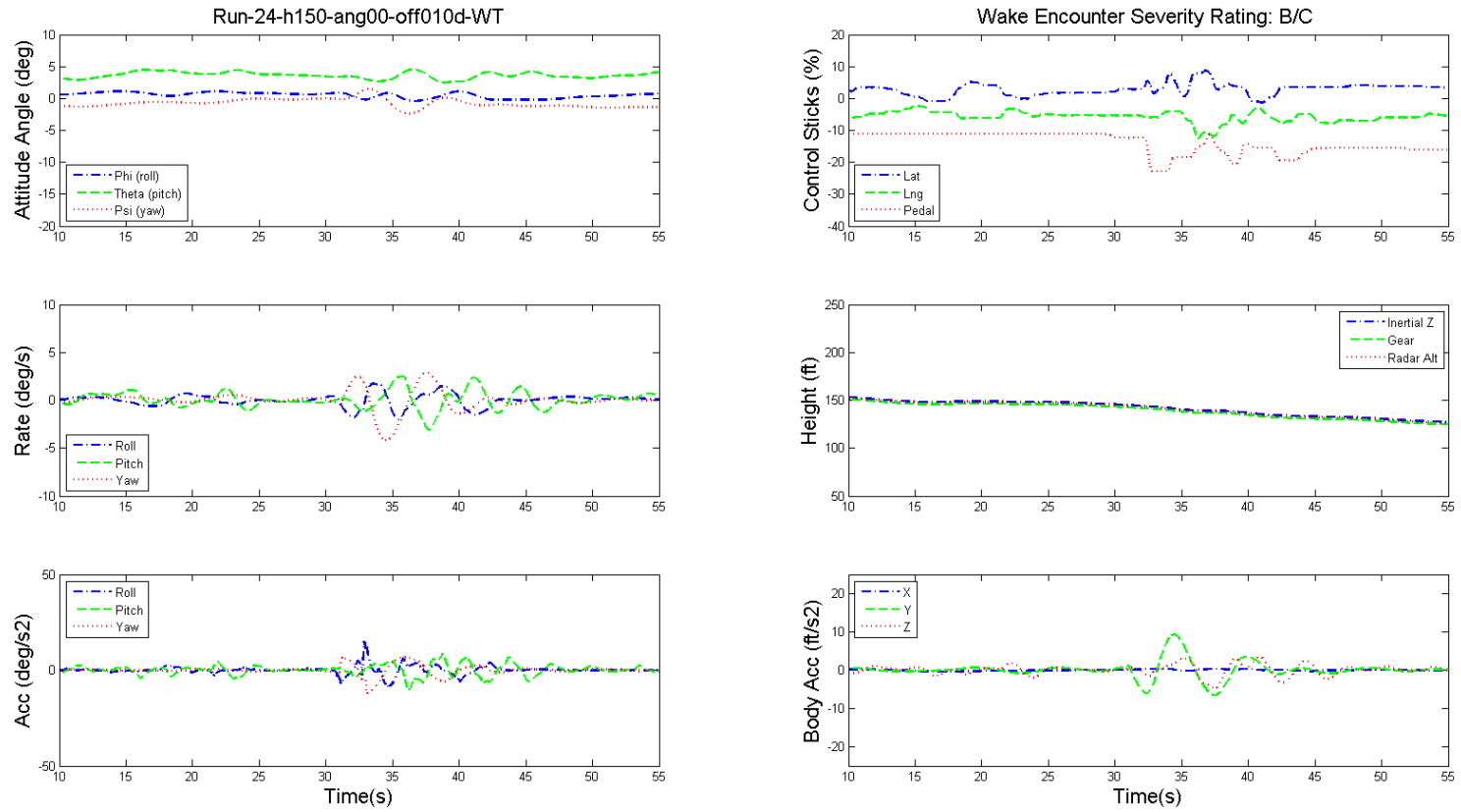


Figure 8.22: Time history of the dynamics of GA aircraft and pilot's controls during wake encounter, wind turbine hub height 150 ft, wind speed 10 m/s, angle 90.0, offset 1.0D.

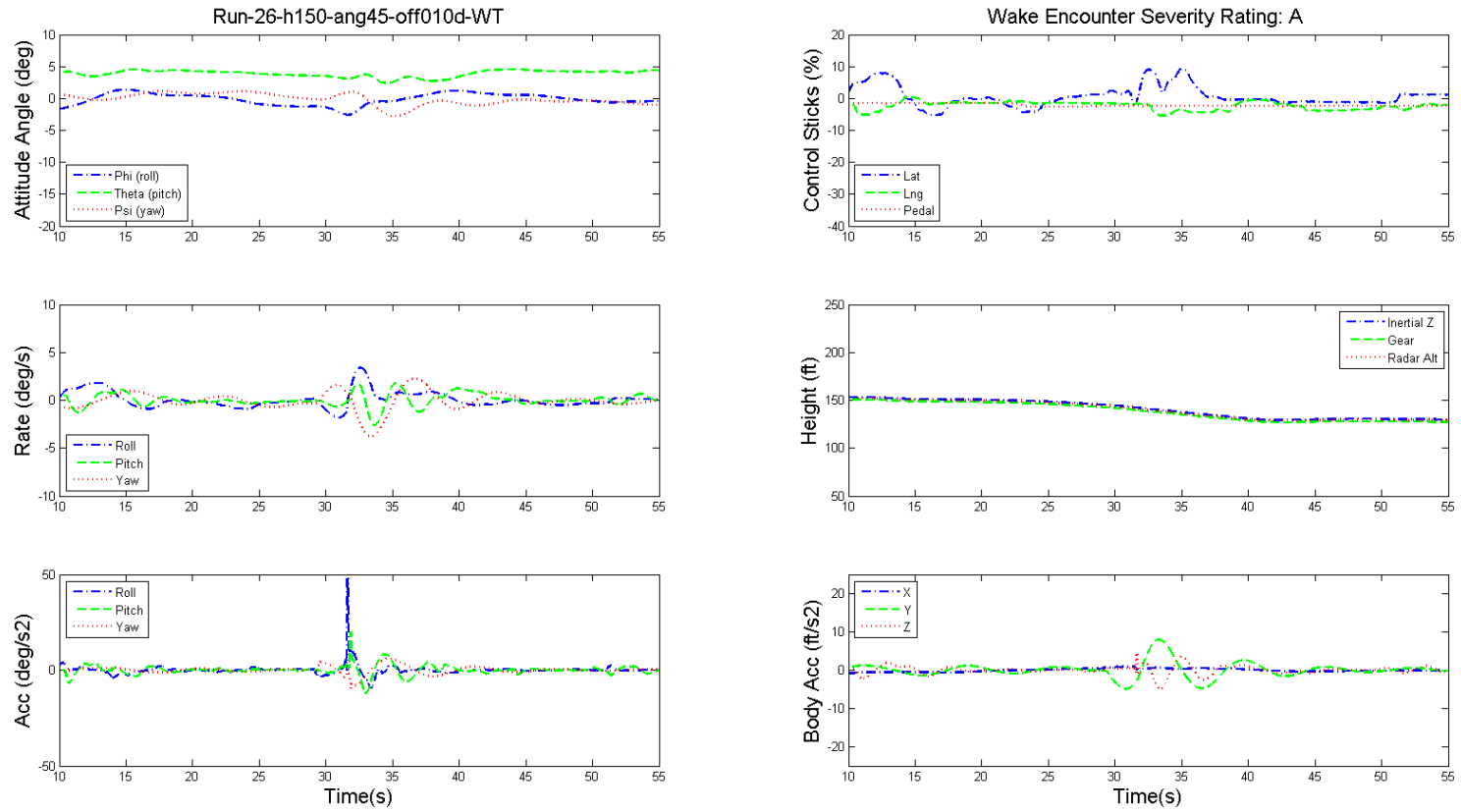


Figure 8.23: Time history of the dynamics of GA aircraft and pilot's controls during wake encounter, wind turbine hub height 150 ft, wind speed 10 m/s, angle 45.0, offset 1.0D.

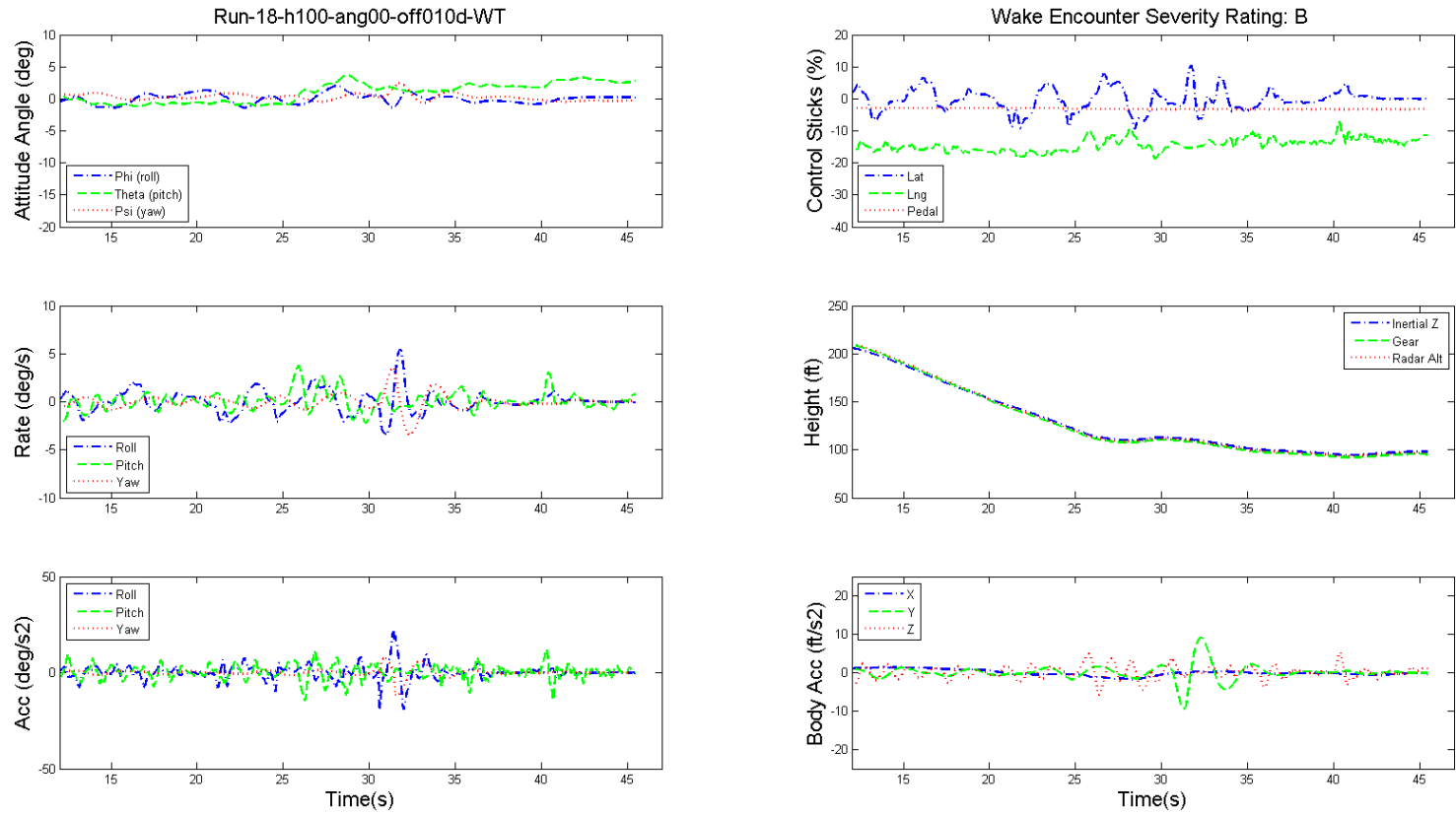


Figure 8.24: Time history of the dynamics of GA aircraft and pilot's controls during wake encounter, wind turbine hub height 100 ft, wind speed 10 m/s, angle 90.0, offset 1.0D.

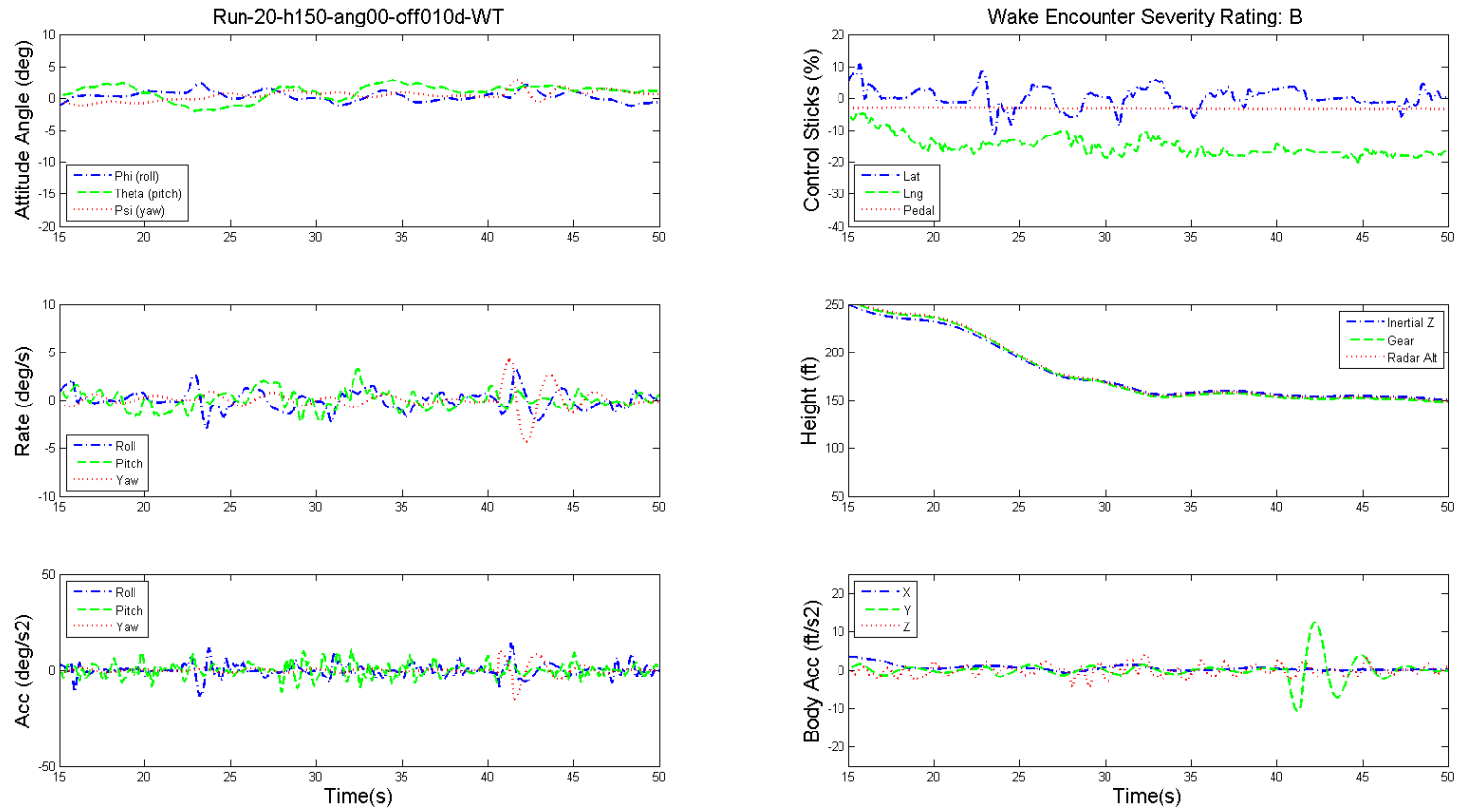


Figure 8.25: Time history of the dynamics of GA aircraft and pilot's controls during wake encounter, wind turbine hub height 150 ft, wind speed 10 m/s, angle 90.0, offset 1.0D.

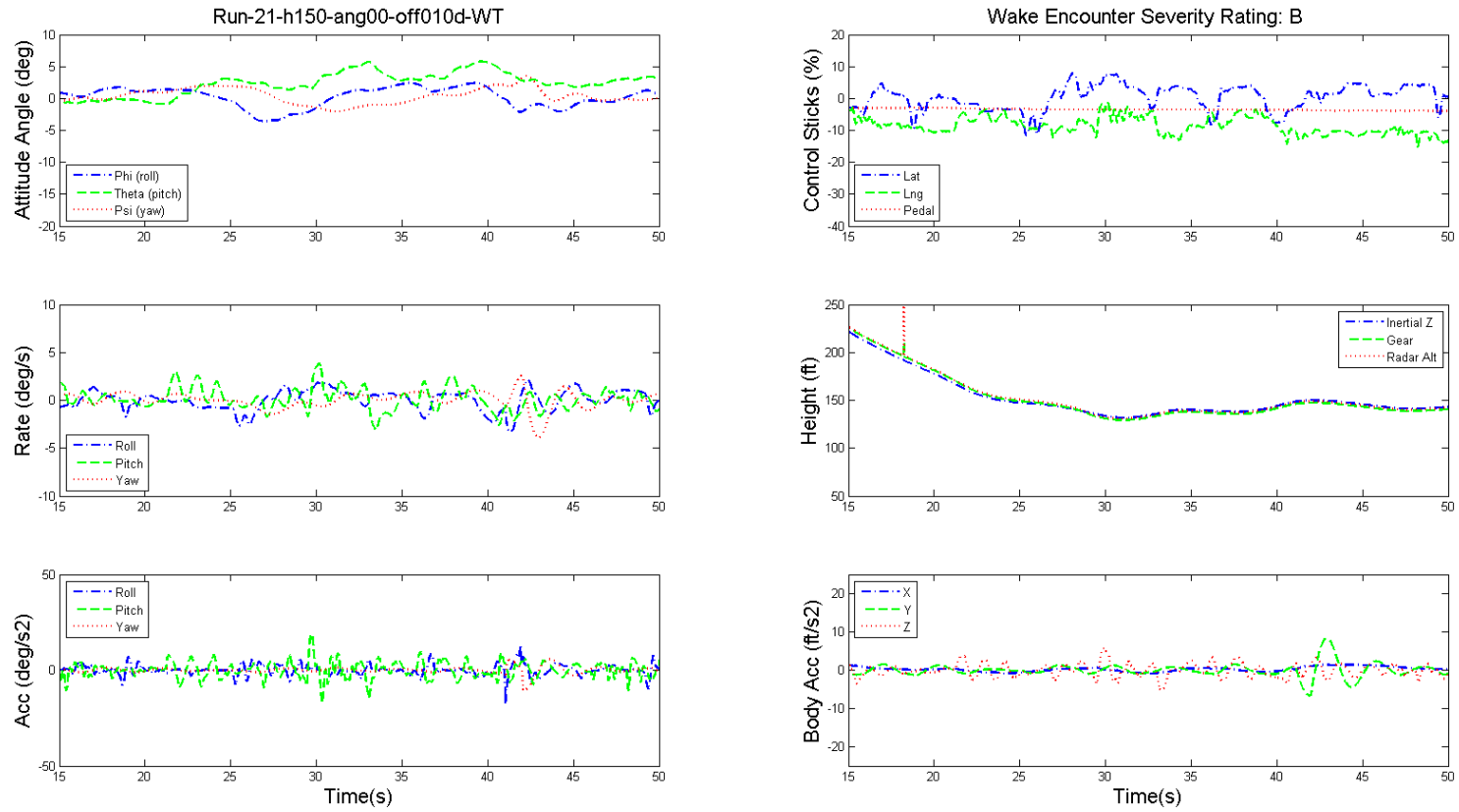


Figure 8.26: Time history of the dynamics of GA aircraft and pilot's controls during wake encounter, wind turbine hub height 150 ft, wind speed 10 m/s, angle 90.0, offset 1.0D.

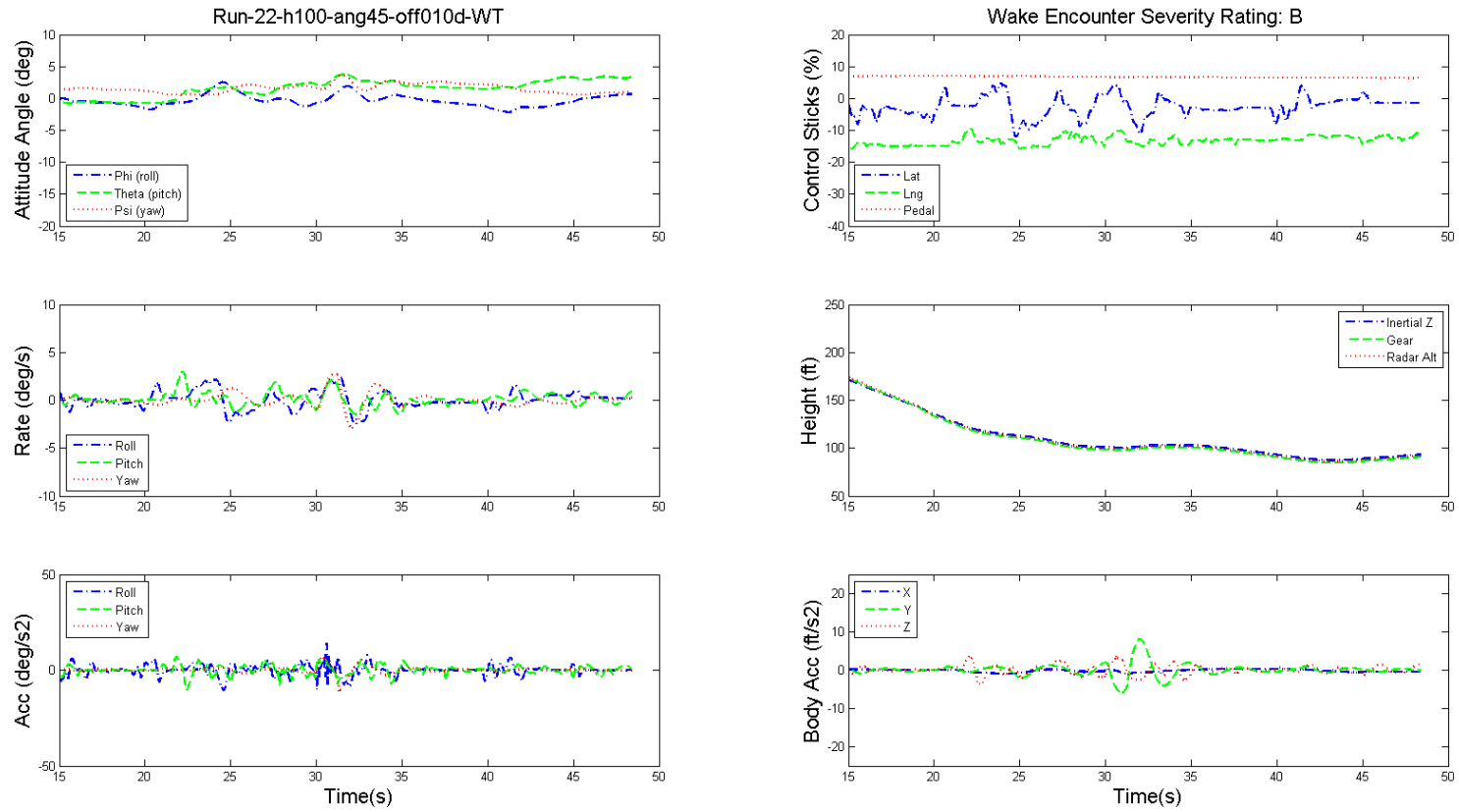


Figure 8.27: Time history of the dynamics of GA aircraft and pilot's controls during wake encounter, wind turbine hub height 100 ft, wind speed 10 m/s, angle 45.0, offset 1.0D.

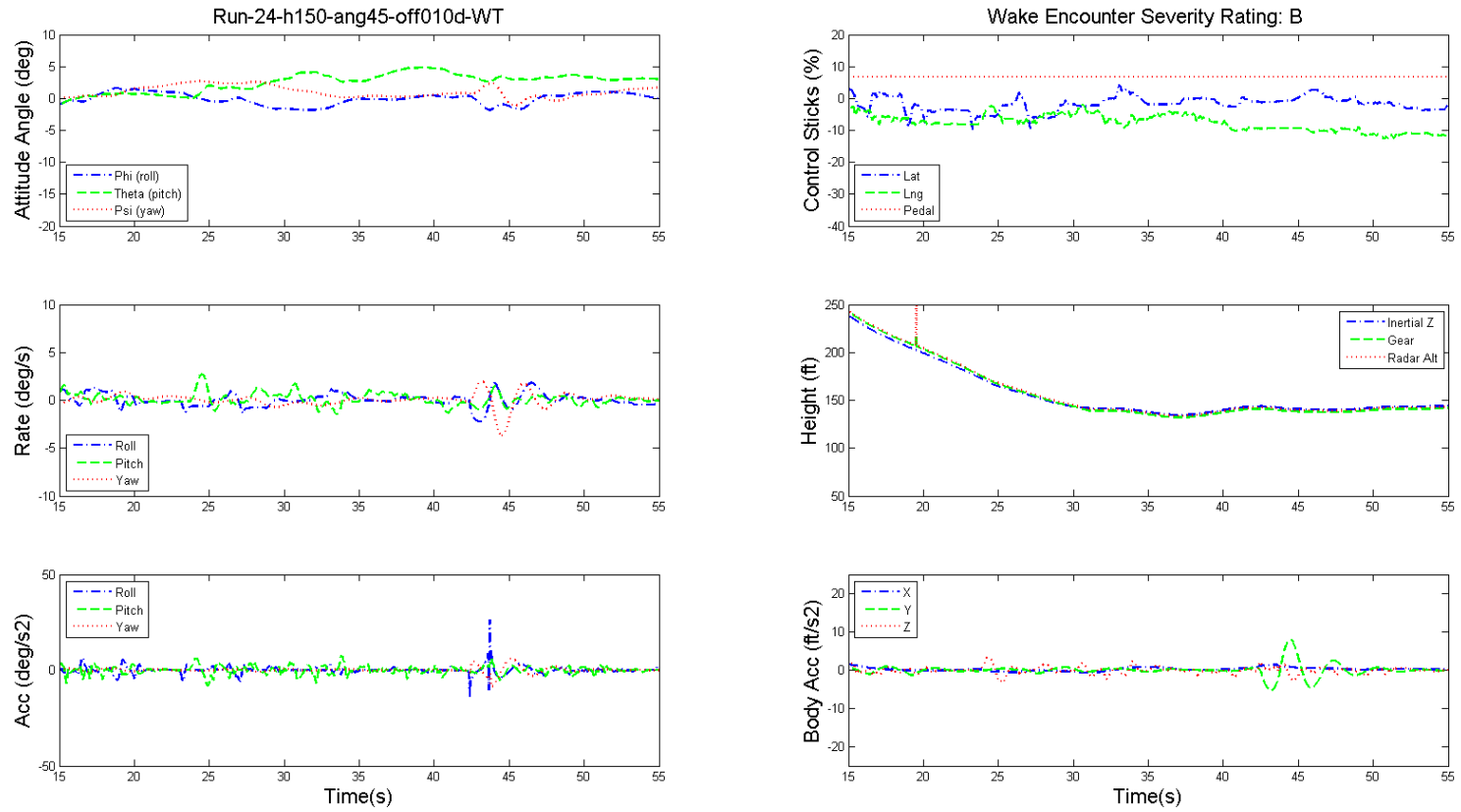


Figure 8.28: Time history of the dynamics of GA aircraft and pilot's controls during wake encounter, wind turbine hub height 150 ft, wind speed 10 m/s, angle 45.0, offset 1.0D.